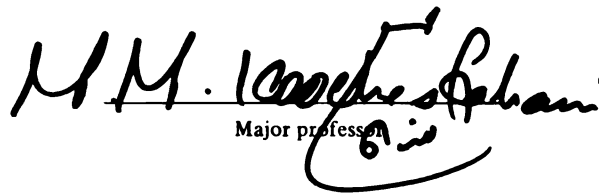This is to certify that the

thesis entitled
EFFECTS OF MOTION HISTORY ON
LEADING EDGE SEPARATION
FOR AN AIRFOIL PITCHING TO
LARGE ANGLES OF ATTACK

presented by

TODD ALLEN BROWN

has been accepted towards fulfillment
of the requirements for

M.S. degree in Mechanical Engineering

Major professor

Date 2-15-92

PLACE IN RETURN BOX to remove this checkout from your record.
TO AVOID FINES return on or before date due.

DATE DUE	DATE DUE	DATE DUE

MSU is An Affirmative Action/Equal Opportunity Institution

c:\circ\datedue.pm3-p.1

EFFECTS OF MOTION HISTORY ON LEADING EDGE SEPARATION
FOR AN AIRFOIL PITCHING TO LARGE ANGLES OF ATTACK

By

Todd Allen Brown

A THESIS

Submitted to

Michigan State University

in partial fulfillment of the requirements

for the degree of

MASTER OF SCIENCE

Department of Mechanical Engineering

1992

ABSTRACT

EFFECTS OF MOTION HISTORY ON LEADING EDGE SEPARATION FOR AN AIRFOIL PITCHING TO LARGE ANGLES OF ATTACK

By

Todd Allen Brown

The evolution of the flow field around a NACA 0012 airfoil pitching to large angles of attack is investigated at a chord Reynolds number of 12,000. The onset of leading edge separation and details of the flow development on the suction side of the airfoil are documented using flow visualization. Both constant and variable pitch rate motions are studied. For low values of constant pitch rate, boundary layer disturbances are observed on the suction side before the onset of leading edge separation. For higher pitch rates, however, leading edge separation occurs prior to the development of such disturbances. Based on constant pitch rate data, a model is developed to predict the onset of leading edge separation for the variable pitch rate motions studied here. The trends indicated by the model are shown to be representative of the data for both higher and lower pitch rates.

Dedicated to my parents,

Jim and Maureen Brown

ACKNOWLEDGEMENTS

TABLE OF CONTENTS

LIST OF TABLES

LIST OF FIGURES

LIST OF SYMBOLS

Symbol   Description

c airfoil chord

C_m moment coefficient

$C_{m_{max}}$ maximum value of moment coefficient for a motion

C_l lift coefficient

C_p pressure coefficient

dC_p/dx chordwise gradient of pressure coefficient

f circular frequency $2\pi\omega$

k reduced frequency $\omega c/2U_\infty$

Re Reynolds number cU_∞/ν

T Time, sec

U_∞ free stream velocity, cm/sec

x distance from the leading edge, cm

α angle of attack, deg

α_m angle of attack at which trajectories match, deg

α_{sep} angle of attack of separation, deg

$\alpha_{s.s.}$ static stall angle, deg

α_1 separation angle associated with $1/2\Omega^*$, deg

α_2 separation angle associated with Ω^*, deg

α_3 separation angle associated with $2\Omega^*$, deg

$\dot{\alpha}$ angular velocity of airfoil, $rad/sec.$

$\dot{\alpha}_{s.s.}$ instantaneous pitch rate at static stall angle, deg

ν kinematic viscosity

ω frequency of sinusoidal oscillation, rad/sec

Ω^* non-dimensional pitch rate $\dot{\alpha}c/2U_\infty$

Chapter I

INTRODUCTION

Airfoils operating in non-steady flow regimes often exhibit temporary but dramatic increases in lift, drag, and moment coefficients relative to those obtained in a steady flow environment. Such increases result from the complex phenomena associated with dynamic stall, and have the potential for both favorable and less than favorable consequences. The result may lead to the enhanced performance of super-maneuverable aircraft in highly dynamic maneuvers or conversely, the premature failure of helicopter rotors designed using static performance data. The detailed understanding and accurate prediction of the unsteady flow development during dynamic stall will ultimately lead to the reliable and efficient exploitation or avoidance of the enhanced aerodynamic performance. Both product life and performance will be improved. Additionally, the insight gained by depicting the controlling mechanisms in dynamic stall will prove very beneficial in our fundamental understanding of unsteady fluid dynamics.

The number of parameters influencing the stall process makes a comprehensive study a formidable task. Parameters known to influence the stall process include: airfoil geometry, motion history, motion type (pitch, plunge, and roll), Reynolds number, pitch axis location, and Mach number. Due to the variety of relevant combinations of controlling parameters, dynamic stall is rich in fluid dynamic phenomena. In its entirety, dynamic stall presents the researcher with an opportunity to study unsteady potential flow, unsteady boundary layer separation, complex viscous-inviscid interaction, shear layer instabilities, shock-boundary layer interactions, vortex formation, vortex interaction with a moving boundary, and complex vortex-vortex interactions. Although experiments have provided a great deal of information on dynamic stall, the underlying physical mechanisms remain insufficiently understood.

1.1 Background

Studies on airfoils undergoing oscillating motions and airfoils pitching to high angles of attack at a constant pitch rate are most abundant in research related to dynamic stall. Results from studies of these two motion types comprise the majority of knowledge on dynamic stall. Each will be discussed below.

1.1.1 Oscillating Motions

Although the evidence of dynamic stall was observed in the early 1930's, extensive experimentation on the dynamic stall process did not occur until the early 1960's and 1970's. This experimentation resulted from the need to understand the unsteady aerodynamic effects causing premature failure of helicopter rotor blades. Static airfoil data were not sufficient to predict the aerodynamic loading on the blades oscillating in a highly dynamic flow regime.

The general features of the phenomenon were documented initially. It was established that the predominant feature of dynamic stall was the development of a strong vortex-like structure near the leading edge, which convected along the surface of the airfoil and into the wake. As the vortex passed over the suction surface of the airfoil, the chordwise pressure distribution was altered producing aerodynamic coefficients which were fundamentally different from the static case (McCroskey 1976).

For these oscillating airfoils, the fundamental parameter influencing the nature and timing of the resulting flow events was found to be the reduced frequency k, defined as:

$$k = \frac{\omega c}{2U_\infty}, \tag{1.1}$$

where ω is defined $\omega = 2\pi f$.

Inviscid studies by Carta (1971) indicated that the delay in the stall event resulted largely from a reduction in the adverse pressure gradient imposed upon the boundary layer for the unsteady case. Note that this reduction was purely an inviscid phenomenon. That is, the unsteady inviscid solution yielded chordwise pressure gradients which were less adverse on the forward portion of the suction surface of the airfoil than the steady inviscid solution at the same angle of attack. The effect of the pitch up motion was to delay the build up of adverse pressure gradients with increasing angle of attack compared to the static case. McCroskey (1973) extended this analysis by Carta with additional inviscid studies. The dynamic delay of separation for oscillating airfoils was predicted with surprising accuracy considering only the inviscid unsteady effects.

Experimental investigations by McCroskey (1976) provided a great deal of insight into the timing and nature of the dominant events associated with dynamic stall of oscillating airfoils. A description of the development of events depicted in these studies is given below and represent, qualitatively, a wide range of unsteady conditions studied for the oscillating airfoil. Note that the Reynolds number of these studies is moderately high, $Re = 2.5 \times 10^6$.

In the initial phases of the motion, the boundary layer remains relatively thin and attached as the airfoil passes through the static stall angle, with no sign of flow reversal along the suction surface of the airfoil. As the angle of attack increases, reverse flow occurs near the trailing edge of the airfoil and a rapid thickening of the boundary layer in that region is observed. Development of eddy structures in this region give a wavy character to the local boundary layer. With increasing angle of attack, the wavy character progresses upstream along the surface of the airfoil.

The boundary layer then experiences a nearly simultaneous catastrophic break-down and separates over the forward portion of the airfoil. As the separation develops, the suction peak magnitude increases near the leading edge indicative of the

formation of a vortex in this region. The developing vortex convects toward the trailing edge of the airfoil at a rate of about 35%-40% of the free stream velocity.

The moment coefficient falls rapidly as the dynamic stall vortex traverses the airfoil midchord. The moment coefficient reaches the lowest value just before the maximum angle of attack. As the vortex convects just downstream of the trailing edge, the moment coefficient rapidly rises to values more characteristic of static stall. A second vortex develops near midchord as the pitch down motion proceeds, producing secondary peaks in C_m. The subsequent developments correspond to the re-attachment phases of the motion cycle progressing from the leading edge region to the trailing edge. It is interesting to note that although the flow re-attaches over the entire surface of the airfoil before the minimum angle of attack is reached, the aerodynamic forces only return to the pre-stall values after the motion has completed the cycle and begun its next upstroke.

For an excellent survey of the research on oscillating airfoils the reader is referred to the review paper by McCroskey (1981).

1.1.2 Constant Pitch Rate Motions

More recently, interest has developed in utilizing lift and drag augmentations for improved combat aircraft maneuverability. This has lead to the study of a second predominant class of airfoil motions; constant pitch rate motions.

For these types of motions, the non-dimensional pitch rate, Ω^*, is known to be a fundamental parameter influencing the flow development and is defined as:

$$\Omega^* = \frac{\dot{\alpha}c}{2U_\infty}. \tag{1.3}$$

The physical significance of Ω^* is that it represents the ratio of the motion time scale to the convective time scale.

Experiments by Walker et. al. (1985) demonstrated the importance of this parameter. The free stream velocity and angular velocity of the airfoil were varied by a factor of four providing a set of motions for which the Reynolds number was varied while the non-dimensional pitch rate remained the same. The resulting C_l vs. α curves for each case were very similar.

The relationships between Ω^* and the general features of the flow development are well known. As Ω^* is increased, the flow remains attached on the suction surface of the airfoil to higher angles of attack. The angle at which leading edge separation occurs has been shown to have a square root dependence on the non-dimensional pitch rate Ω^* by Graham (1986). Work by Visbal (1990) has indicated that higher pitch rates correspond to increased magnitudes of pressure gradients and a stronger suction peak in the high angle portions of the motion. These are induced by a stronger and more coherent dynamic stall vortex and result in higher values of maximum lift coefficient. Additionally, the location of formation of the dynamic stall vortex is closer to the leading edge with increasing Ω^*.

Once leading edge separation has occurred and the dynamic stall vortex begins to develop, it convects downstream at a relatively constant speed. Lorber et. al. (1987) have computed these speeds from pressure traces. Values vary from $0.13U_\infty$ at $\Omega^* = 0.001$ to $0.33U_\infty$ at $\Omega^* = 0.02$. Empirical relations have been suggested by Jumper et. al. (1989) to predict the stall angle from the separation angle based upon the notion of a common vortex convection speed for various pitch rates. However, as figure 1.1 indicates (Gendrich 1991), a large scatter in vortex convection values from different authors suggests that this topic offers much opportunity for further investigation.

The location of the pitch axis location is also known to influence the stall process. Documenting its effects on the stall process is of fundamental importance. Due to the non-common pitch axis locations in experiments of different authors, it is difficult to correlate their various results. Additionally, airfoils in practice will experience a variety of pitch axis locations depending upon airfoil geometry (swept wing) and aircraft

design. From this, the fundamental importance of understanding and documenting the effects of pitch axis location becomes clear.

Jumper et. al. (1989) conducted experiments to investigate the effects of pitch axis location on the flow development for airfoils pitching to large angles at constant rate. From these studies, it was observed that the changes in separation angle resulting from changing the pitch axis location correlated closely with the changes in effective angle of attack at the leading edge of the airfoil. For the non-dimensional pitch rates and pitch axis locations studied, $\Omega^* < 0.06$ and x/c = 0.25, 0.50, 0.75, 1.00 respectively, the change in separation angle produced by changing the pitch axis location, was accounted for by the effective angle of attack at the leading edge of the airfoil.

Computations by Visbal (1990) investigated the effect of pitch axis location in a higher pitch rate range; $\Omega^*/2$ = 0.045, 0.2. The primary effect of moving the pitch axis from c/4 to the trailing edge was to delay both the buildup of the circulation surrounding the airfoil and the separation process. It is interesting to note that the propagation characteristics of the reverse flow were not significantly affected over the forward half of the airfoil. It was shown that the propagation of the reverse flow over this portion of the airfoil was mainly influenced by the instantaneous chordwise pressure gradient. That is, for any fixed location on the forward portion of the suction surface of the airfoil, the arrival of the reverse flow front at this location corresponded to nearly the same value of chordwise pressure gradient and it was independent from the pitch axis location. Additionally, the nature and location of the vortex development was not significantly affected by changing the pitch axis location.

Understanding the nature of 3-D effects is essential to the application of dynamic stall to aircraft in practice. Robinson et. al. (1988) conducted experiments on 3-D effects of a finite wing span on the stall process using an airfoil with a "semi-aspect ratio" of 2. The flow development near the effective midspan of the airfoil was observed to remain largely the same as in the 2-D cases. Pressure measurements at a span location of 1.8c inboard from the wingtip were highly indicative of 2-d vortex

initiation and development. However as the span location moved closer to the wingtip, the convection of the dynamic stall vortex was more and more retarded. For a span-wise location of 0.4c in from the wingtip, the interaction with the 3-D wingtip vortex completely retarded the convection of the stall vortex. An additional point of interest from this study was the improvement in the spanwise lift distribution for the dynamic case when compared to the quasi-steady case of airfoils with finite span.

A particularly detailed and insightful description of the dynamic stall process is given by Visbal (1991). The description of a progression of flow events characteristic of the dynamic stall process for constant pitch rate motions based on his work follows.

For an airfoil at some small angle of attack below the static stall angle, the flow remains relatively attached and follows the general contour of the airfoil. As the pitch-up motion begins, the pressure on the suction surface decreases with increasing angle and the suction peak begins to move closer to the leading edge. From the suction peak forward the pressure gradient is favorable, and aft of the suction peak the pressure gradient is unfavorable. An increasing magnitude of suction peak with angle of attack is observed, and in general the pressure gradients over the entire suction surface of the airfoil become larger in magnitude with time. As the adverse pressure gradients along the suction surface become more severe with time, the low momentum fluid near the surface, which to a large extent existed at the outset of the motion, is unable to overcome the adversity and a reverse flow region forms which eventually extends over a majority of the airfoil upper surface. For airfoils with well rounded leading edges this region of flow reversal progresses from the trailing edge to the vicinity of the leading edge, except possibly for very fast motions (i.e. high pitch rates) in which an independent region of flow reversal forms near the leading edge just prior to the arrival of the reverse flow front from the trailing edge.

Independent of the propagation characteristics, this reverse flow region remains very thin and conforms to the surface of the airfoil. Even as the reverse flow region extends nearly to the leading edge, the C_p distributions resemble fully attached flow

and for this reason the flow is not yet said to have separated. Shortly after the reverse flow reaches the leading edge region of the airfoil, a protuberance in the boundary layer forms over a forward portion of the airfoil upper surface to accommodate the influx of fluid from the reverse flow. As this protuberance grows in thickness, a distinct recirculation region forms. The development of the protuberance and recirculation region corresponds to the initiation of the leading edge separation. This recirculation region develops into an energetic vortical structure labeled a dynamic stall vortex. The dynamic stall vortex continues to grow and convects downstream at a relatively constant rate. Increasing lift is evident until the dynamic stall vortex reaches about 70% of the airfoil chord (Chow et. al. 1986). At this point dynamic stall occurs. Lift falls dramatically along with a quick moment reversal.

1.2 Objective

Research on dynamic stall conducted to date has provided substantial information on the stall process for airfoils undergoing constant pitch up motions and oscillating motions. However, very little is known about the stall process for airfoil motions which deviate from these two basic motion types. This is unfortunate as in practice, it is the exception rather than the rule that such idealized conditions exist. Thus, understanding how the stall process is affected as the airfoil motion deviates from these idealized cases is essential.

It is the purpose of this work to investigate how the flow field evolution is altered when the motion trajectory deviates from the constant pitch rate case. Specifically, the onset of leading edge separation and the details of the flow development on the suction side of the airfoil are investigated for constant pitch rate motions. These results are then compared to cases where the motion trajectory deviates from the constant pitch rate case using variable pitch rate motion trajectories.

Chapter II

FACILITY AND INSTRUMENTATION

The data obtained in this study were acquired from two sets of experiments. The apparatus used and procedures followed are described below.

2.1 Experimental Apparatus

All the experiments were conducted in the Free Surface Water Channel of the Turbulent Shear Flows II Laboratory at Michigan State University. The water channel has a test section of 61 cm x 61 cm in cross section by 274 cm long, and is optically accessible from all sides including a downstream observation window. The maximum flow speed of the channel is 100 cm/sec. A schematic of the facility is given in figure 2.1.

A NACA 0012 airfoil of rectangular planform is used in the study. The airfoil has a 12.0 cm chord and a 48.6 cm span. The quarter chord location is used for the pitch axis. A support assembly houses the airfoil and all actuation hardware. This assembly is composed of two plexiglas false walls which are attached above water level by aluminum cross supports. The false walls are hollow and contain the airfoil mounting hardware and drive linkages. The central spanwise axis of the airfoil is located at the central streamwise location of the false walls which extend 2.5 chord lengths in the upstream and downstream direction from this axis. The walls are mounted flush with the ends of the airfoil to assist in the realization of 2-D study. A schematic of the support assembly is depicted in figure 2.2.

A programmable digital closed loop servo controller (Galil DMC-610) and a DC servo motor (Galil Motor 500/1000B) are used to implement the airfoil motion. This control system can be programmed to realize arbitrary motion trajectories with control

of motion acceleration and velocity as a function of time or distance. Note that for this work a motion trajectory is defined to be the angle versus time trace for a particular pitch up motion. The system allows the user to tune the motions with control of gain and damping parameters. The angular resolution of the motor position is 0.09 degrees. A schematic of the control system components is given in figure 2.3.

The flow is visualized using the hydrogen bubble technique. This technique is described in detail by Schraub et. al. (1965). Typically flood lighting is used to illuminate the hydrogen bubbles, however in this study a laser sheet at the midspan location is used for the illumination of the hydrogen bubbles. This has the additional advantage of qualitatively indicating the 2-D nature of the flow at this location. If the bubbles which are initially coplanar with the laser sheet encounter a spanwise component of velocity of sufficient magnitude and duration, they will leave the laser sheet and cease to be illuminated. Note that obtaining quantitative information of the 3-D nature of the flow is not implied or pursued in this work. The hydrogen bubble arrangement used in this experiment is depicted in figure 2.4.

The working electrode is a 0.05 mm (0.002 in.) diameter by 20cm long stainless steel (T351) wire suspended at each end by a wire holder constructed from 5 mm diameter steel rod and insulated with heat shrink tubing. The flow speeds used in the experiments, result in a wire Reynolds number of 5 which is well below the range (40) in which vortex shedding occurs, thus assuring a planar convection of the hydrogen bubbles from the wire. The wire is oriented normal to the airfoil's planform at zero degrees angle of attack and at the midspan location approximately 1 mm upstream from the leading edge. It is found that placing the wire close to the leading edge greatly assists in the placement of bubbles deeper into the boundary layer region. The current waveform is generated by a voltage signal from a Hewlett Packard HP-3314A function generator amplified by a Kepco BOP 100-2M power supply. The bubbles are generated using a 30 volts peak to peak square wave operating at 20 Hz with a -15 volt offset.

The beam from a 4-watt argon ion laser (Excel 3000) is passed through a combination of converging lens and cylindrical lens to provide a laser sheet of approximately 1-2mm in thickness to illuminate the hydrogen bubbles. The sheet is normal to the pitch axis and is oriented to project onto the upper (suction) surface of the airfoil as depicted in figure 2.5.

Flow visualization images are sensed by an electronically-shuttered CCD camera with an exposure time of 2 msec/field at a rate of 60 fields/sec. The images are stored on video tape and then digitized and stored on a hard disk through a digital image acquisition/processing system (Trapix 5500). The digitized images are enhanced with an appropriate look-up-table to emphasize the important features of the flow and output on a laser printer via a laser printer controller system (LaserPort GrayScale). This system has the desirable features of cropping, scaling, and placing multiple images on a page.

2.2 Motion Controller Tuning

Once the theoretical motion desired for a particular trajectory is programmed into the control system memory, it is necessary to tune the controller to minimize system error. The airfoil position versus time is sensed via the system encoder. Position sensing is subject to two software imposed constrains. The maximum allowable sample size is 1000 data points per motion, and the overall data collection time must correspond to 2^n sec where n is an integer from 1 to 8 inclusive. For these experiments the maximum sample size is used and the overall data collection time is set to the lowest power of 2 sec which is greater than the motion time. This corresponds to sampling periods of 2 msec - 128 msec and position increments of approximately 0.1 deg between samples for the cases studied. In the initial stages of the tuning process, the position output is plotted on the computer screen using Galil software for quick

inspection. In the final tuning stages the system output is plotted along with the desired position output on hardcopy to assist in the tuning process.

The steady state initial position error is minimized by adjusting an offset parameter which supplies a bias to the motor input signal. This bias counteracts the static aerodynamic and gravitational torques on the airfoil and drive system assuring a zero initial angle of attack.

The motion trajectories for the pitch-up motions conducted in these studies are composed of either 1 or 3 straight motion segments. A motion segment is defined as a portion of the motion trajectory in which the airfoil pitches between two angles of attack at a constant pitch rate. To minimize the transition time between consecutive motion segments it is desirable to accelerate to the new pitch rate as rapidly as possible. For this reason, the acceleration is typically set to a value well in excess of that attainable by the motor maximum torque. The system gain and damping are then set at the highest values consistent with both critical damping and straight motion segments. Note that for slower motions excessive damping and gain values produce motion segments which are not straight due to slight deviations from the nominal pitch rate of a given motion segment.

2.3 Obtaining Airfoil Position from Image Output

In order to determine the specific angle at which particular events occur in the development of the flow it is important to know the precise angle of the airfoil for each image. Prior to the start of an experiment the airfoil is set to zero degrees angle of attack. With the airfoil initially close to this position, dye is carefully injected into the upper and lower recirculation regions existing at the trailing edge of the airfoil. The airfoil position is then adjusted until the chordwise extent of both recirculation regions are equal. This procedure provides confidence that the airfoil is zeroed to within 0.5 degrees of the free stream direction. It is important to note that all runs

within a data set, have identical geometric zero angles of attack. Only when comparing runs from different data sets does this uncertainty become relevant.

Once the airfoil's zero angle of attack has been set, it is necessary to correlate the airfoil position with the image output. The initial step is to determine the precise starting time of the motion relative to the image sequence. This is accomplished by programming the controller to send a 50 ms pulse to a LED light positioned in the camera field of view. The 50 ms pulse is chosen to improve the temporal resolution of the initiation of the motion. By observing whether a flash is observed in a single frame or two consecutive frames, the starting time of the motion can be deduced to within ±10 ms.

Once the motion starting time is determined, the time in the motion for a particular image is calculated from the number of frames into the sequence and the time between frames. The time of an image is converted to angle of attack by referring to the α vs. t output for the airfoil which was acquired during the tuning and testing process under identical conditions. Note that a second 50ms pulse is sent to the LED light when the airfoil reaches 20° as a consistency check.

Chapter III

CONSTANT PITCH RATE MOTION EXPERIMENT

3.1 Background

As discussed in the Introduction, the non-dimensional pitch rate Ω^* is a fundamental parameter influencing the dynamic stall process for constant pitch-up motions. Flow visualization studies are conducted to reveal details of the nature and timing of the separation process for a broad range of Ω^* values traversing the range $0.01 \leq \Omega^* \leq 0.40$. Emphasis is placed on high spatial and temporal resolution. The airfoil is pitched about the quarter chord from zero to sixty degrees angle of attack with a constant pitch rate. Figure 3.1 depicts the actual α vs. t traces for six of the eight cases studied. Note that the time axis for each case is scaled such that the pitch-up motion depicted spans the majority of the plot. This corresponds to a decrease in the maximum time on the horizontal axis with an increase in the pitch rate. The free stream velocity for the experiment is 10 cm/sec corresponding to a chord Reynolds number of Re $= 1.2 \, x \, 10^4$.

The primary event in the stall process studied in this experiment is the onset of leading edge separation. This event is tied closely to the development of a protuberance in the forward portion of the marked/unmarked fluid interface on the suction surface of the airfoil, and represents the initiation of a chain of events generic to dynamic stall. The development of this protuberance provides the experimenter with a distinct visual marker in the flow development to indicate the onset of leading edge separation. For a detailed description of the initiation of the separation process, the reader is referred to the computational studies by Visbal (1991).

In the present work, the onset of leading edge separation will be denoted to occur when the protuberance from which the dynamic stall vortex evolves is first observed as

a distinct feature in the flow visualization. This definition becomes clear by observing the image in figure 3.5 corresponding to an angle of attack of 22.0°. The increased gap between the hydrogen bubbles and the airfoil surface over the leading edge 10% of the airfoil corresponds to leading edge separation for this trajectory. By viewing the subsequent images in this figure, it is possible to observe that the dynamic stall vortex does in fact develop from this region. The above definition provides a repeatable and consistent means of depicting the timing of the initiation of the dynamic stall vortex development corresponding to a particular motion trajectory and provides a basis to compare the timing of the flow development between different motion trajectories.

It is important to note that for the lowest two pitch rates studied, $\Omega^* = 0.02, 0.01$, it was not possible to consistently depict the onset of leading edge separation. For these cases no attempt was made to quantify or acknowledge a leading edge separation event. It is important to keep this in mind during the description of the flow development associated with these pitch rates. For a pitch rate of $\Omega^* = 0.03$ the development of the protuberance is distinguishable and becomes more so with increasing pitch rate.

As is evident in the flow visualization images, the hydrogen bubbles do not mark the entire boundary layer, and fluid is visualized down to a layer which is displaced from the airfoil. The extent of this region has been minimized by placing the hydrogen bubble wire approximately 1mm from the leading edge of the airfoil. Placing the hydrogen bubble wire further upstream moves the interface of the marked-unmarked fluid further from the surface of the airfoil. Placing the hydrogen bubble wire less than 1 mm from the leading edge makes it difficult to distinguish the initial development of the protuberance associated with the onset of leading edge separation. At higher pitch rates such placement allows the hydrogen bubbles to penetrate the boundary layer sufficiently to make the marked fluid indistinguishable from the illuminated surface of the airfoil in the region of interest.

The kinematics of the bubble transport involved in this experiment would make a very interesting study, however the conclusions from the work presented here are not dependent on such analysis. This would clearly not be the case if the aim of this work was to obtain detailed kinematic information of the flow field from the hydrogen bubble motion.

3.2 Results

3.2.1 Separation Process

The separation events on the suction surface of the airfoil are observed to be strongly affected by the value of Ω^*. The description of the separation events for four pitch rate values are given below, $\Omega^* = 0.02, 0.04, 0.10, 0.20$. Note that the flow developments observed over the range of pitch rates studied are represented by these four cases.

Figure 3.2 depicts the flow development corresponding to $\Omega^* = 0.02$. For this pitch rate a wavy character in the boundary layer at the trailing edge region becomes evident as the airfoil reaches 8.1°. The formation of small vortices appear at the trailing edge by 8.5° and form at progressively forward locations with increasing angle of attack. At an angle of 9.0° a small vortex is observed forming at the midspan location. Note that the spacing between these developing vortices is approximately c/6 and that they are being sequentially shed into the wake with no evidence of pairing. At this angle of attack the formation of the interface between the fluid marked by the hydrogen bubbles and the unmarked fluid strongly resembles the spatial development of a low Reynolds number free shear layer. The development of these vortices results from the presence of reverse flow over the aft portion of the airfoil suction surface as discussed in greater detail later in this chapter. Associated with this reverse flow is a region of clockwise vorticity which is removed from the surface of the airfoil. This

region of vorticity is highly unstable and, given sufficient distance from the airfoil surface, emulates a free shear layer subject to Kelvin-Helmholtz instabilities. For this reason the vortices such as those described in the preceding paragraph are typically referred to as shear layer vortices in dynamic stall literature. Such vortices will subsequently be referred to as shear layer vortices in this work.

By 9.6° the shear layer vortex at the midchord is retarded from convecting downstream. It is anticipated that this retardation is associated with a large local reverse flow velocity near the airfoil surface. Just upstream of this shear layer vortex the initial development of three more shear layer vortices is observed with a spacing of roughly c/9. At 10.4°, a recirculation region appears to have formed over the forward 50% of the airfoil.

At 11.4°, the marked fluid contained in the recirculation region over the forward c/2 at 10.4° has dispersed over the entire suction surface of the airfoil. With increasing angle of attack this region of vorticity thickens and by 16.1°, a large region of vortical fluid exists over the entire suction surface of the airfoil.

Figure 3.3 depicts the flow development associated with $\Omega^* = 0.04$. With this increase in pitch rate, the undulations in the boundary layer no longer progress from the trailing edge toward the leading edge as observed for $\Omega^* = 0.02$. Undulations are observed over the aft 75% of the airfoil nearly simultaneously at 11.9°. In this region, three shear layer vortices are observed developing with a spacing of c/6 as in the previous case with $\Omega^* = 0.02$. However for this pitch rate, the simultaneous disturbance amplification has the distinguishing appearance of temporally developing free shear layer as opposed to a spatially developing shear layer.

At 12.3°, a protuberance in the marked/unmarked fluid interface is observed over the forward 30% of the airfoil, and by 12.8° a distinct recirculation region is evident at this location. Note that this initial recirculation region is confined closer to the leading edge than for $\Omega^* = 0.02$. At 17.0°, the shear layer vortices have colligated into a single larger vortical structure depicted by the dark region at the trailing edge of the

airfoil. Further increases in α correspond to an extension and thickening of the leading edge recirculation region, and by 21.4.° a relatively diffuse dynamic stall vortex is observed which extends over the majority of the suction surface.

The flow development associated with $\Omega^* = 0.10$ is depicted in figure 3.4. At an angle of 17.5°, a distinct protuberance is visible over the forward 20% of the airfoil corresponding to the onset of leading edge separation. Note that aft of this region, disturbances in the marked/unmarked fluid interface are not present except for very near the trailing edge. This is opposite of what occurs for $\Omega^* = 0.02$, in which the disturbances originate at the trailing edge and progress toward the leading edge. Thus by varying the pitch rate by a factor of 5, disturbances can be observed originating at the trailing edge and progressing forward ($\Omega^* = 0.02$), occurring nearly simultaneously with the initiation of leading separation ($\Omega^* = 0.04$), or occurring after the onset of leading edge separation ($\Omega^* = 0.10$).

By 22.2°, in addition to the leading edge recirculation region which is developing, three distinct shear layer vortices are observed over the aft 50% of the airfoil. The spacing of these shear layer vortices is also approximately c/6. As the airfoil moves from 20.6° to 25.7° an interesting display of vortex interaction is visible. Starting at 20.6°, the shear layer vortex nearest the leading edge begins to pair with the neighboring shear layer vortex immediately downstream and by approximately 24.0°, pairing has occurred. At 34.4°, a large region of vorticity is observed over the midchord location of the airfoil which is representative of the dynamic stall vortex.

The flow development associated with $\Omega^* = 0.20$ is depicted in figure 3.5. For this pitch rate, the flow on the suction surface of the airfoil appears quiescent (as depicted by the hydrogen bubbles) up to 20.1°. Note that the marked/unmarked fluid interface over the forward 50% of the airfoil remains very close to the airfoil surface. At 22.0°, a distinct protuberance is visible over the leading edge c/8 of the airfoil. This leading edge disturbance continues to develop, while on the remainder of the

airfoil, the marked-unmarked fluid interface continues to appear undisturbed. At 27.4°, a distinct protuberance in the marked-unmarked fluid interface is observed developing just downstream of the leading edge recirculation region.

Let α_s be defined as the angle at which leading edge separation is detected. The increase of α_s with respect to Ω^* is evident in figures 3.2-3.5. For the cases studied, the separation angles are plotted against Ω^* in figure 3.6. Note that the lower two pitch rate values $\Omega^* = 0.01$, and 0.02 are not represented in the plot. For these pitch rates no distinguishable separation region is observed from flow visualization. For these cases, the separation process is dominated by the trailing edge separation which progresses to the leading edge. The separation angle is plotted as a function of the square root of Ω^* in figure 3.7. The nearly linear dependence of α_{sep} on $\sqrt{\Omega^*}$ is in agreement with the observations by Graham (1986). Note that no physical argument was given by Graham for this functional dependence nor is one given here.

The length of the initial recirculation region associated with leading edge separation is observed to decrease with increasing Ω^*. In figure 3.8, the initial recirculation region is depicted for six of the pitch rates studied. For each case, a distinct recirculation region is evident which spans from the leading edge to the chordwise location x/c_{sep}. Note that x/c_{sep} is indicated by a white arrow. Figure 3.9 shows the relationship between the length of this recirculation region and the pitch rate. Data points for $\Omega^* = 0.01$ and $\Omega^* = 0.02$ are omitted due to the difficulty in depicting a repeatable separation event and a well defined recirculation region. Note that for pitch rates below $\Omega^* = 0.05$ the length of the separation region drops relatively quickly with increasing pitch rate, and for pitch rates above $\Omega^* = 0.10$, the change is much less pronounced.

It is anticipated that the length of this recirculation region will have a fundamental influence on angle at which stall occurs. It is important to note that the extent of the initial recirculation region represents the bounds of the developing dynamic stall vortex and as indicated in the Introduction, this vortical region (dynamic stall vortex)

progresses downstream at a relatively constant rate. Given a constant vortex convection rate and that stall occurs once the stall vortex reaches a specific chordwise location on the airfoil, then a vortex which develops closer to the leading edge will have a longer time delay between dynamic stall vortex formation and stall. All else being equal, a vortex which forms closer to the leading edge must convect farther before stall occurs and thus stall would be expected to occur at a higher angle of attack.

The portions of the boundary layer aft of the initial leading edge separation region in general roll up into small shear layer vortices and convect towards the trailing edge of the airfoil. The manner in which this occurs is observed to be very pitch rate dependent. For the lowest pitch rates, $\Omega^* = 0.01$, 0.02, 0.03, and 0.04 the shear layer rolls up into small vortices (often pairing) and sequentially convect into the wake. For $\Omega^* = 0.05$ and 0.10, the shear layer vortices colligate into a single shear layer vortex before convecting into the wake. In the case of the highest pitch rates studied, $\Omega^* = 0.20$ and 0.40, the shear layer vortices also colligate into a single shear layer vortex, but this vortex does not convect into the wake. Just as the shear layer vortex reaches the trailing edge, it reverses directions and convects toward the leading edge. Soon after, the shear layer vortex has either amalgamated with the dynamic stall vortex or has been torn up by it. This process is depicted more clearly later in this chapter.

As the shear layer vorticity aft of the leading edge recirculation region rolls up and convects toward the trailing edge of the airfoil a variety of vortical developments and interactions are observed in this region, as depicted in figures 3.2-3.5. Depending on the motion, various numbers of shear layer vorticies are observed with pairing, and tripling.

It is interesting to note that the repeatability of the detailed shear layer development is observed to be pitch rate dependent. For pitch rates above $\Omega^* = 0.03$, the details of the timing, spacing, and location of the shear layer vortex formations appear very repeatable as depicted in figure 3.10. In this figure, leading edge separation and

shear layer roll up are depicted for a repeated motion with a constant pitch rate of Ω^* = 0.10. The left column corresponds to run #1 and the right column to run #2. Identical angles of attack are depicted for each run. Note the similarity in the development of both the leading edge recirculation region and the shear layer vortices, for each angle of attack.

For pitch rates below Ω^* = 0.03 some of the details of the developments are not as repeatable. An example of this is given in figure 3.11 for a repeated motion with a constant pitch rate of Ω^* = 0.02. For this case, the developments appear very similar for the two runs with the exception of an apparent lag for run #1 up to 9.0°. At 9.1°, three shear layer vortices are observed forming over the aft portion of the airfoil in run #2, while only two are observed forming in run #1. Note that the disturbances in the shear layer are observed further upstream for run #2 than run #1. By 9.6° two shear layer vortices have rapidly formed at the midchord location from the nearly quiescent region which existed at 9.5° for run #1. Conversely, for run #2 at 9.6°, three small shear layer vortices are forming forward of the shear layer vortex which existed near the midchord at 9.5°. At 10.4°, a shear layer vortex is observed at c/6 from the trailing edge in run #1 and c/4 in run #2. Additionally at this angle, a patch of vortical fluid appears to be detaching from the recirculation region near the leading edge in run #1 while this is not evident for run #2.

When considering the aerodynamic loads as a function of angle of attack, these differences in details for repeated runs are anticipated to be only a second order effect at most. However, these effects may be of concern to the experimenter monitoring the flow development with velocity or pressure measurements. For example, if pressure at a particular chordwise location is monitored as a function of time in the motion, then the variations between runs may may cause considerable scatter in the pressure traces for different runs, and averaging the pressure traces may mask the existence of much of the small scale phenomena in the flow.

3.2.2 Reverse Flow Propagation

Much of the vortical activity described above results from the presence of a thin reverse flow region along the suction surface of the airfoil as depicted in figure 3.12. Note that the thickness of the reverse flow region has been exaggerated for illustration. The presence of this reverse flow region has been observed experimentally by McCroskey et. al. (1976) for oscillating airfoils at low reduced frequencies, and computationally by Visbal (1991) for constant pitch up motions at high pitch rates. This reverse flow is believed to be responsible for setting up the Kelvin-Helmholtz instabilities from which the shear layer vortices evolve. Additionally, the reverse flow is believed to play an integral part in the initiation of the dynamic stall vortex (Visbal 1991). In light of the importance of the development of this reverse flow, experiments were conducted to investigate the qualitative nature of this reverse flow region over a large range of pitch rates.

The qualitative nature of the reverse flow region is obtained by monitoring the progression of the fluid contained in the recirculation region existing near the trailing edge of the airfoil at $\alpha = 0.0°$. Laser induced fluorescein (LIF) is used to mark this region by depositing a patch of fluorescein dye in the trailing edge recirculation region through a dye tube just prior to the onset of the motion. Since only the aft region fluid is marked, the forward progression of the dyed fluid represents a lower bound of the forward progression of the reverse flow front along the suction surface of the airfoil. Additionally, it serves as an indicator of the reverse flow velocity at certain combinations of chordwise location and angle of attack. The progression of the dyed fluid is depicted in figures 3.13-3.16. The pitch rates represented correspond to the cases depicted in the flow visualization studies above (figures 3.2-3.5).

For $\Omega^* = 0.02$, the dyed fluid propagates to the leading edge. For the remaining cases the dyed fluid only reaches the midspan region before erupting from the surface of the airfoil and becoming entrained in the shear layer vortices. An increase in the

pitch rate from $\Omega^* = 0.04$ to $\Omega^* = 0.20$ only slightly retards the maximum forward progression of the dye. The progression of the dyed fluid front indicated reverse flow speeds on the order of $0.3U_\infty$.

Evident in figures 3.13-3.16 are several eruptions (ejections) of the dyed fluid outward from the surface of the airfoil. Comparison with figures 3.2-3.4 (which depict the corresponding outer flow developments) shows that these eruptions occur in the presence of the shear layer vortices. The ejections are observed just upstream of an adjacent shear layer vortex. Since the shear layer vortices are rotating in a clockwise direction, a particular eruption occurs on the side of shear layer vortex in which the normal velocity component is away from the surface. This is consistent with the findings by Smith and Walker (1990) as depicted in figure 3.17. Eruptions were observed in the streamwise portion of the horseshoe vortices developed in a laminar boundary layer impinging on a circular cylinder. The presence of a vortex near a solid wall was described as inducing a moving region of adverse pressure gradient which given sufficient time in the vicinity of the wall always produced a boundary-layer eruption. Note that after the ejections have developed sufficiently, the corresponding dye becomes sufficiently mixed with it's neighboring shear layer vortex that the dye can be used to mark the vortex development.

For the cases of $\Omega^* = 0.10$ and 0.20, the entrainment of the shear layer vorticity into the dynamic stall vortex is evident at the high angle portions of figures 3.15 and 3.16. This process is depicted in figure 3.16 for $\Omega^* = 0.20$ for $\alpha \geq 39.1°$. The shear layer vortex (marked by the dyed fluid) convects just off the trailing edge of the airfoil (43.9°) at which time it reverses directions and moves back along the surface of the airfoil toward the leading edge (56.3°) and up into the vortex (59.9°).

Chapter IV

MATCHING ANGLE EXPERIMENT

4.1 Background

In the previous chapter, many properties of the flow development associated with constant pitch rate motions were described. Of these properties, possibly the most influential on the high angle portions of the flow development is the angle at which leading edge separation occurs. The experiments contained in this chapter are designed to investigate both what portions of the pitch up motion influence the angle at which this leading edge separation is observed and how this separation process is affected by variations in the motion trajectory from that of a purely constant pitch rate motion.

Investigations are limited which relate to the effects of motion history on the dynamic stall process for non-oscillating airfoils pitching to large angles of attack. Koochesfahani at. el. (1990) have studied the effects of the magnitude of initial acceleration on the onset of leading edge separation for otherwise constant pitch rate motions. Variable accelerations for the pitch rates $\Omega^* = 0.2$ and 0.4 were studied for an airfoil pitching from zero to sixty degrees angle of attack. Three acceleration values corresponded to constant acceleration during the first 18°, 4°, and 1° of the motion. The magnitude of the acceleration was found to not influence the angle at which the onset of leading edge separation was detected.

Lorber and Carta (1987) studied the effects of the initial angle of attack on the subsequent flow development. The initial angle of attack of the airfoil was found to have little influence on the maximum lift coefficient for a constant pitch rate trajectory if the initial angle of attack was such that the airfoil did not experience partial stall prior to the initiation of the motion.

The experiments described in the preceding two paragraphs contribute to under-standing the effects of motion history on the dynamic stall process. However, a great deal of experimentation is still required to completely understand these effects. The experiments presented in this chapter are designed to address this issue by investigat-ing the importance of the instantaneous pitch rate as the airfoil passes through the static stall angle ($\alpha_{s,s}$) of the airfoil (indicated to be of significance for oscillating air-foils by McCroskey (1981)), and the effect of either increasing or decreasing the pitch rate of the airfoil at an angle close to imminent leading edge separation angle. Addi-tionally, a model is developed to predict the onset of leading edge separation for the variable pitch rate trajectories based on the constant pitch rate data.

4.2 Experimental Conditions

The motion trajectories used in these experiments are constructed from a set of three motion trajectories A, B, and C, which are specified by a parent pitch rate, Ω^*, and a matching angle, α_m, at which all three trajectories converge. A set of these tra-jectories is depicted in figure 4.1. Trajectory C is a constant pitch rate motion with the parent pitch rate Ω^*, while both trajectories A and B are composed of three motion segments. Trajectory A is characterized by a pitch rate equal to $1/2\Omega^*$ for $0° < \alpha <$ $1/3\alpha_m$ and $2\Omega^*$ for $1/3\alpha_m < \alpha < \alpha_m$. Trajectory B is characterized by a pitch rate equal to $2\Omega^*$ for $0° < \alpha_m < 2/3\alpha$ and $1/2\Omega^*$ for $2/3\alpha_m < \alpha < \alpha_m$. Parent pitch rates of $\Omega^* = 0.05$ and 0.20 are used in the study which represent low and high pitch rate ranges respectively. Matching angles are varied to represent the range $0° \leq \alpha_m \leq 60°$. Actual trajectories are depicted in figure 4.2 for variable pitch rate motions. Cases A, B, and C are shown for parent pitch rates $\Omega^* = 0.05$ and 0.20 in the left and right columns respectively. The corresponding matching angle is 20° for each case. The airfoil is pitched about the quarter chord from zero to sixty degrees angle of attack with a free stream velocity of 10 cm/sec (Re = 1.2 x 10^4).

As in the constant pitch rate motion study, the angle at which leading edge separation is detected is used to compare the effect of different motion trajectories on the flow development. The onset of leading edge separation is depicted using the same criteria as described in chapter 3.

4.3 Effect of Pitch Rate at the Static Stall Angle ($\alpha_{s.s.}$) on Leading Edge Separation

Research on the phenomenon of dynamic stall of airfoils has indicated the high-angle part of the oscillating airfoil dynamic stall cycle depends strongly on the instantaneous pitch rate near the static stall angle. The same lift and moment behavior beyond the static stall angle can be attained by matching the pitch rate at static stall and beyond for two cases with different amplitudes (McCroskey (1981)). In light of this observation, we ask the following question: Is the instantaneous pitch rate at static stall angle a controlling parameter in the subsequent development of the flow field beyond the static stall angle in the case of non-oscillating airfoils?

To answer this question, the angle at which leading edge separation is detected is used to compare the flow development for trajectories with different instantaneous pitch rates through the static stall angle ($\dot{\alpha}_{s.s.}$). Note that the static stall angle ($\alpha_{s.s.}$) for this airfoil and Reynolds number is approximately 12°. Figure 4.3 indicates how α_m for the trajectory sets can be chosen to carry out the investigation. In 4.3(I), α_m is slightly below $\alpha_{s.s.}$. For this case, all three motion trajectories pass through $\alpha_{s.s.}$ at the same pitch rate, i.e. they have the same $\dot{\alpha}_{s.s.}$ values, while the portions of the trajectories below $\alpha_{s.s.}$ are largely varied. In 4.3(II), α_m is chosen such that trajectories A and B have identical $\dot{\alpha}_{s.s.}$ values while the $\dot{\alpha}_{s.s.}$ value for trajectory C is lower by a factor of two. In figure 4.3(III), the matching angle is chosen such that each trajectory has different $\dot{\alpha}_{s.s.}$ values. Note that the value of $\dot{\alpha}_{s.s.}$ for case A is a factor of four larger than for case B.

In figure 4.4 a comparison of the flow developments for cases (A) and (B) from the trajectory set with a parent pitch rate of $\Omega^* = 0.2$ are depicted. The matching angle is $15.0°$ which corresponds to different $\dot{\alpha}_{s.s.}$ values (i.e. figure 4.3(III)). Note that the flow development is very similar for each case. The notable exception is that disturbances are observed over the aft portion of the airfoil at a lower angle of attack for case B than for case A. In figure 4.5, the separation angles for all three trajectories of the set are plotted. The similar separation angles for each case indicate the instantaneous pitch rate through the static stall angle is not a controlling parameter in this pitch rate range. Note that the variations in separation angles are within the uncertainty of $\pm.6°$ for these trajectories. In figure 4.6, the separation angles are plotted for a matching angle of $21°$. Note that the trajectories A and B pass through the static stall angle with the same pitch rate, yet the separation angles for each are different.

As the parent pitch rate is reduced by a factor of four to $\Omega^* = 0.05$, the pitch rate through the static stall angle is shown to influence the separation angle. The separation angles for a matching angle of $15°$ are plotted in figure 4.7. In this case, each trajectory corresponds to a different separation angle. The separation angles for a matching angle of $10°$ are given in figure 4.8. For this case, the separation angles are also different for each case, however to a lesser degree. These results indicate that for this lower pitch rate range, the pitch rate through the static stall angle influences the subsequent development of the flow field. However it is not a controlling parameter. Note that this is in contrast to the findings by McCroskey (1981) for the case of oscillating airfoils in which the portions of the trajectory below the static stall angle of the airfoil were shown not to influence the higher angle portions of the flow development.

4.4 Effect of Decreasing the Pitch Rate in the Vicinity of the Separation Angle

For motion trajectory sets with sufficiently large α_m values, separation occurs well before the matching angle is reached. Causality indicates that for such

trajectories, the portion of the motion trajectory above α_m does not influence the leading edge separation process. Consequently, for high matching angles, trajectories A and B may be thought of as "quasi" two motion segment trajectories as far as the onset of leading separation is concerned. In this section and in section 4.5, motion trajectories of this nature will be discussed. Case B trajectories will be considered in this section, while case A trajectories will be considered in section 4.5.

For both case A and B trajectories, with high α_m values, it is not as convenient to specify the trajectory by the matching angle. A more instructive parameter is the pitch rate transition angle (α_t). This is the angle at which the motion trajectory switches from the first constant pitch rate motion segment to the second constant pitch rate motion segment (i.e. see figure 4.1). For case A trajectories, α_t corresponds to the angle at which the pitch rate is increased by a factor of four, while for case B trajectories, α_t corresponds to the angle at which the pitch rate is decreased by a factor of four. Although the α_m will not be used to directly specify the motion trajectories in this or the subsequent section, it can be used to determine α_t for trajectories A and B. The value for α_t is related to α_m algebraically: $\alpha_t = 1/3\alpha_m$ for case A, and $\alpha_t = 2/3\alpha_m$ for case B.

In addition to α_t, there are two parameters which are instructive in describing the results of the high matching angle trajectories (i.e. "quasi" two motion segment trajectories) discussed in this and the following section. These are the constant pitch rate separation angles associated with the highest and lowest constant pitch rate motion segment in the trajectory. The angle associated with the highest pitch rate motion segment is α_3. This is the angle at which leading edge separation would occur for a constant pitch rate motion with a pitch rate equal to that of the highest pitch rate motion segment in the trajectory. Similarly, α_1 corresponds to the separation angle associated with the lower constant pitch rate motion segment in the trajectory.

The values of α_1 and α_3 represent a possible range of leading edge separation angles for the trajectories considered here. One might expect the separation angle to be at or between the separation angles corresponding to the highest and lowest pitch rates in the trajectory, α_3 and α_1 respectively.

Consider the case B trajectories with a parent pitch rate of $\Omega^* = 0.20$ and high matching angles. The separation angle (α_3) corresponding to the higher pitch rate ($\Omega^* = 0.40$) in these trajectories is 27.5°. Similarly, for the lower pitch rate ($\Omega^* = 0.10$) in these trajectories, $\alpha_1 = 17.5°$. The lower portion of several case B trajectories are plotted in figure 4.9. The associated transition angles range from α_t slightly less than α_1 to α_t slightly larger than α_3. Additionally, the actual angle at which leading edge separation is detected (α_{sep}) is depicted on each respective trajectory.

From this figure it is evident that α_{sep} is relatively independent of α_t for $\alpha_t <$ α_1. However for each of these cases, separation occurs slightly higher than α_1. Even though the airfoil was being pitched at four times the rate over the majority of the angle range before separation, the separation angle was only slightly increased when compared to the constant pitch rate motion of the lower pitch rate. This indicates that for these trajectories, the onset of leading edge separation is largely controlled by the instantaneous boundary conditions.

As α_t is increased above α_1, the separation angle increases as might be expected. Causality indicates that separation would not occur before α_t for $\alpha_t \leq \alpha_3$. For $\alpha_t > \alpha_1$, the time of separation remains nearly constant, while the angle of separation increases with increasing α_t. Note the decreasing time interval between the pitch rate transition time and the onset of leading edge separation as the transition angle is increased from α_1 to α_3. For $\alpha_t > \alpha_3$, separation occurs at nearly the same angle of attack as depicted by multiple data points near α_3.

Next, consider a similar set of case B trajectories, however in a lower pitch rate range. The lower portions of case B trajectories with parent pitch rate $\Omega^* = 0.05$ are

plotted in figure 4.10. As in figure 4.9, the separation angles are plotted on the lower portions of the actual trajectories with α_t ranging from slightly less than α_1 to α_t slightly larger than α_3. The separation angle (α_3) corresponding to the higher pitch rate ($\Omega^* = 0.10$) in these trajectories is $17.5°$, and similarly for the lower pitch rate ($\Omega^* = 0.025$), $\alpha_1 = 10.7°$. Evident in this figure are similar trends to those found in figure 4.9, however the features of the data are not as distinct. That is, a constant separation angle for $\alpha_t < \alpha_1$ and a constant separation time for $\alpha_t > \alpha_1$ are not as distinct as for the higher pitch rate range.

4.5 Effect of Increasing the Pitch Rate in the Vicinity of the Separation Angle

In this section, case A trajectories with high matching angles are discussed, and the motivation and nomenclature from the previous section apply. These motion trajectories correspond to the following scenario. Consider an airfoil undergoing a constant pitch rate motion for which the leading edge separation angle (α_{sep} for this example) is known. Suppose that just before separation is about to occur, the pitch rate of the airfoil is rapidly increased to a new higher constant pitch rate. Is it possible to delay the onset of leading edge separation through such tactics, or is separation at α_{sep} unavoidable? The results which follow address this question.

The lower angle portions of several case A trajectories with parent pitch rate of $\Omega^* = 0.20$ and the corresponding separation angles are plotted in figure 4.11. The pitch rate transition angles (α_t) range from $12.3°$ ($5°$ lower than $\alpha_1 = 17.5°$) to $19.3°$ ($2°$ higher than α_1).

For the lower α_t values, the separation angle is not influenced by the presence of the low pitch rate portion of the trajectory. Separation occurs near the angle corresponding to the higher pitch rate, α_3. This occurs for transition angles which are at least two degrees below the separation angle associated with the lower pitch rate, α_1.

The flow field evolution for one such case is depicted in figure 4.12 for which α_t = 16°. This trajectory corresponds to the fifth (farthest to the right) data point near 27.5° in figure 4.11. The flow development for this trajectory is very similar to that of the $\Omega^* = 0.40$ constant pitch rate motion. Note that the size of the initial leading edge recirculation region for the variable motion trajectory is identical to that of the constant pitch rate case, and that α_{sep} = 26.5°. This result indicates that for this pitch rate range (and type of motion trajectory), α_{sep} is independent of the motion trajectory even up to moderate angles of attack (i.e. 16° which is 4° greater than $\alpha_{s.s.}$).

Two exceptions to the similarity between the constant pitch rate case and the case A trajectory with α_t = 16° are observed. For the case A trajectory, the presence of small disturbances over the midspan region of the airfoil occur nearly simultaneously with the onset of leading edge separation. Conversely, these are not observed until after the onset of leading edge separation for the constant pitch rate case. Additionally in the case A motion trajectory, a thickening in the region of unmarked fluid (near the surface of the airfoil) over the forward 30% of the airfoil is observed at α = 24.0° and 25.4°. From these frames, it is evident that separation is about to occur with a mechanism associated with the lower pitch rate ($\Omega^* = 0.10$). However the remaining frames reveal that the subsequent separation process is consistent with the higher pitch rate (the initial separation region is confined much closer to the leading edge). This initial longer protuberance is not present for the constant pitch rate trajectory.

As α_t is increased from 16° to 18.3°, α_{sep} is reduced from 26.5° to 17.5°. Note that α_t = 18.3 corresponds to the trajectory with the highest matching angle on figure 4.11. Such a large change α_{sep} with only a 2.3° change in α_t indicates that α_{sep} is very sensitive to the pitch rate through this portion of the case A trajectories in this pitch rate range. This is in strong contrast to the portions of the motion below 16° which had virtually no influence on α_{sep}.

In figure 4.13, the flow field evolution for a slightly higher pitch rate transition angle is depicted (α_t = 19.3°). This trajectory is not plotted on figure 4.11, however it should be noted that in this case, α_t is nearly 2° greater than α_1. This trajectory demonstrates the effect increasing the pitch rate after separation has occurred on the subsequent development of the leading edge separation region.

Comparison of figure 4.13 with figure 3.4 in which the flow field evolution is depicted for the constant pitch rate motion , $\Omega^* = 0.10$ (the initial pitch rate of the case A trajectory) shows that the initial stages of the separation process are nearly identical in each case for $\alpha < 19.0°$. However after the pitch rate is increased in case A, the similarity between the two flow developments quickly disappears. For the case A trajectory the development of the leading edge recirculation region and the disturbances over the remainder of the airfoil surface are impeded under the influence of the higher pitch rate.

At 22.0°, a comparatively small protuberance near the leading edge and relatively weak disturbances are evident on the surface of the airfoil for the case A trajectory. Conversely, at nearly the same angle of attack, 22.2°, a well defined recirculation region is apparent near the leading edge and three shear layer vortices are evident on the surface of the airfoil pitching at constant pitch rate. Note that these disparities have occurred within 3° of airfoil motion. This is an example of how the portions of the motion trajectory above α_{sep} strongly influence the subsequent flow development.

Comparison of figure 4.13 with 4.12 gives an indication of response of the flow field to a change in pitch rate which occurs above α_{sep} and how the flow begins to emulate the development associated with the constant pitch rate motion corresponding to the new higher pitch rate. As indicated above, the development of the separation region in figure 4.12 is nearly identical to the constant pitch rate motion with $\Omega^* = 0.40$ and will be used to represent the constant pitch rate motion flow development associated with this pitch rate.

Figures 4.12 and 4.13 depict a large difference in the angles of leading edge separation, 26.5° and 17.8° respectively. However comparing figure 4.12 (α = 30.2°), with figure 4.13 (α = 26.8°) shows that the development of the leading edge separation region is nearly identical for each at these respective angles of attack. This is a 3.4° discrepancy compared to nearly 9° for the onset of leading edge separation. Comparing each flow development in the vicinity of 40° shows that by this angle of attack, the development of the recirculation near the leading edge for each case is nearly identical. This indicates that for the case A trajectory with ($\alpha_t > \alpha_{sep}$) the initial lag in flow development as compared to the higher constant pitch rate case, decreases with increasing angle of attack. This is in contrast to what might have been expected: the flow development maintaining a constant lag behind the constant pitch rate case.

Figure 4.14 is similar to figure 4.11 with the exception that the parent pitch rate has been reduced by a factor of four to $\Omega^* = 0.05$ and the pitch rate transition angles are slightly lower to encompass $\alpha_1 = 10.7°$. This corresponds to α_t values ranging from 7.7° to 15.7° inclusive. Note that for the trajectories with higher α_t values in the plot, two separation angles are indicated for each trajectory and will be discussed later in this section.

For the lowest transition angle, 7.7°, separation is detected at 16.9°, slightly below $\alpha_3 = 17.5°$. As α_t is increased to 9.7°, α_{sep} is reduced to 15.0°. The evolution of the flow field for this trajectory is depicted in figure 4.15. This corresponds to the third trajectory from the left in figure 4.14. An interesting feature in this flow evolution is the development of the four shear layer vortices over the trailing 50% of the airfoil chord. All these vortices amalgamate into a single larger vortex with a large degree of stretching occurring in the aft vortices. For this trajectory, the development of the initial recirculation region and the dynamic stall vortex is very similar to the constant pitch rate case for $\Omega^* = 0.10$.

As the transition angle is increased to 13.7°, a secondary separation event takes place as depicted in both figures 4.16 and 4.17. Up to an angle of 13.2° inclusive in

figure 4.16, the images depict the flow development associated with a constant pitch up motion. At an angle of 13.2°, the recirculation region over the forward portion of the airfoil is thin and elongated, spanning the forward 60% of the airfoil chord. Note that between this and the subsequent frame, at 13.7°, the pitch rate is increased by a factor of four to $\Omega^* = 0.10$. Analysis of the video tape for this motion trajectory, indicates that after α_t, a new shorter recirculation region forms at the leading edge which only spans the forward 30% of the airfoil chord. This is evident at 18.0°. It is from this new shorter recirculation region that the dynamic stall vortex evolves. The aft portion of the fluid contained in the initial larger recirculation region was convected down-stream into the wake without interaction with the newly forming recirculation region. The subsequent development of the dynamic stall vortex is very similar to that associated with the constant pitch rate motion for $\Omega^* = 0.10$.

For this motion trajectory a difficulty arises in defining the angle at which the onset of leading edge separation occurs. Maintaining the guidelines for depicting the onset of leading edge separation used through out this work, it is clear that separation occurs near 10.7°, and that up until the pitch rate transition angle, the leading edge recirculation region develops from this initial separation region. However after the pitch rate transition angle, a new smaller leading edge recirculation region forms closer to the leading edge, and it is from this second recirculation region that the dynamic stall vortex ultimately evolves. Which separation event should be relevant to the subsequent flow development? A researcher interested in flow control techniques to delay the onset of leading edge separation may be more interested in the initial separation event, while a researcher interested in predicting stall may be more interested in the secondary separation. Thus, it important to indicate both events. It is for this reason that the trajectories with the higher α_t values on figure 4.14 have two separation angles indicated.

This "double" separation phenomenon reveals a very important characteristic of the dynamic stall process. This indicates that even though the flow on the suction side

of the airfoil has developed a recirculation region spanning over 60% of the airfoil chord, the subsequent flow development can still be influenced by the local (in time) unsteady boundary conditions, and the resulting flow evolution is very similar to the development if the airfoil had been pitched at a constant rate for the entire motion. The degree to which this holds for the aerodynamic coefficients would make a very insightful study. An additional point to note is that recirculation region which develops into the dynamic stall vortex, does not necessarily monotonically increase with increasing angle of attack as observed in the constant pitch rate trajectories.

For the pitch rate transition angles between 9.7° and 13.7°, there is a gradual transition from a clearly depicted leading edge separation event for $\alpha_t = 9.7°$ and the double separation phenomena apparent for $\alpha_t = 13.7°$. For these cases it is difficult to clearly depict onset of the secondary separation event as indicated in figure 4.17 for which $\alpha_t = 11.7°$. Note that for this trajectory, the leading edge recirculation region spans a smaller portion of the airfoil chord at 16.2° than at 13.3°.

4.6 Theoretical Model

The results described above indicate that for a higher pitch rate range the onset of leading edge separation is relatively insensitive to the motion history. That is, if the airfoil is on a particular motion segment of the trajectory, leading edge separation in general occurs near the leading edge separation angle associated with the constant pitch rate of that motion segment, independent of the pitch rate values of the previous motion segments in the trajectory. For the lower pitch rate range, a similar trend exists, however the influence of the motion history is observed to have a more noticeable effect on the separation angle, i.e. the separation angle is influenced to a larger extent by the constant pitch rate values of the lower angle motion segments of the trajectory. In an effort to consolidate the results described thus far and to indicate the extent to which the separation angle is insensitive to the motion history, a theoretical

model is developed to predict leading edge separation for the variable motion trajectories studied in this work. It is emphasized that the motivation for developing the following model is to investigate the degree to which the separation process is insensitive to the motion history.

The principle assumption in the formulation of the present model is that the angle of leading edge separation is independent of the motion history. That is, whether or not separation will occur at a particular point in the motion trajectory is assumed to depend only on the instantaneous boundary conditions at the airfoil surface. We take the instantaneous boundary conditions to be specified by the instantaneous pitch rate and angle of attack. Note that for an arbitrary motion trajectory, it might not be possible to neglect the instantaneous angular acceleration of the airfoil. However, the motion trajectories in this study have been designed to minimize the acceleration time between constant pitch rate motion segments. Consequently, leading edge separation in general does not occur during the acceleration/deceleration portions of the trajectory and it is reasonable to neglect the effect of the instantaneous acceleration.

The constant pitch rate separation angles (α_{sep}) associated with a particular trajectory set form the basis of the model. These indicate potential angle/pitch rate combinations for which leading edge separation is predicted to occur. If the instantaneous angle of attack is below the constant pitch rate separation angle associated with the instantaneous pitch rate, then leading edge separation would not occur. Separation occurs during the first motion segment in the trajectory which has a portion at or above α_{sep} associated with that motion segment's pitch rate. Separation occurs at the separation angle associated with that motion segment.

As an example, consider case B in figure 4.5. The first motion segment (corresponding to the highest pitch rate in this trajectory) is entirely below α_3, the separation angle associated with this first motion segment. Thus, separation is not expected to occur on this motion segment. Similarly, the highest portion of the second motion segment is also below its corresponding separation angle, α_1, and separation is

not expected to occur on this portion of the trajectory. However, a portion of the third segment in the trajectory does exceed α_2, it's corresponding separation angle, and consequently, separation is predicted to occur at $\alpha_2 = 22.2°$ on this motion segment. Conversely, in figure 4.6 case B, separation does not occur during the third motion segment as in the previous case. In this case, the higher portion of the second motion segment is above it's corresponding separation angle α_1, and separation is predicted to occur on this motion segment at $17.5°$.

The preceding examples illustrate how changes in α_t for a transition from a lower pitch rate to a higher pitch rate can influence the angle at which separation is predicted to occur. For α_t slightly less than α_1 separation would occur at α_2, while for α_t slightly larger than α_1 separation would occur at α_1.

Next, consider the transition from a higher pitch rate to a lower pitch rate in which α_t is greater than the separation angle associated with the lower pitch rate. Under this constraint, there are two possibilities. If α_t is greater than the transition angle associated with the higher pitch rate, then α_{sep} would equal the separation angle associated with the higher pitch rate, independent of α_t (causality tells us this). While if α_t is less than or equal to the separation angle associated with the higher pitch rate, separation would be expected to occur the instant that the trajectory begins the lower pitch rate motion segment, i.e. at α_t.

Extending the ideas presented above, it is possible to predict the separation angle for cases A, B, and C, given any matching angle. For a particular parent pitch rate in a trajectory set, there correspond three constant pitch rates: $1/2\Omega^*$, Ω^*, and $2\Omega^*$. Note that the constants $1/2$ and 2 result from the way in which the motion trajectories were designed. Different values could have been designed into the trajectories. The restriction was that their product be unity to maintain a common matching angle for trajectories A and B. Associated with $1/2\Omega^*$, Ω^*, and $2\Omega^*$ are three constant pitch rate separation angles: α_1, α_2, and α_3 respectively. Given α_1, α_2, and α_3, the separation angles for cases A and B are predicted as a function of α_m below. The model for

the case A trajectories is first developed followed by a development of the model for the case B trajectories. Note that for the case C trajectories, α_{sep} is simply α_2.

For the case A trajectories with $\alpha_m < \alpha_2$, the first two motion segments are both completely below their respective constant pitch rate separation values, and separation occurs at α_2 associated with the third motion segment: $\alpha_{sep} = \alpha_2$ for $\alpha_m \leq \alpha_2$. However, as α_m is increased beyond α_2, separation is delayed to a higher angle. As long as α_m is below α_3 the separation will not occur until the end of the second motion segment and thus $\alpha_{sep} = \alpha_m$ for $\alpha_2 < \alpha \leq \alpha_3$. For further increases in α_m, the separation will occur at α_3 as long as the transition angle between the first two motion segments remains below α_1. Due to the pitch rate ratios used in the trajectories (1/2 and 2) this transition angle is related to the matching angle by $\alpha_t = 1/3\alpha_m$. Thus $\alpha_t = \alpha_1$ when $\alpha_m = 3\alpha_1$, giving: $\alpha_{sep} = \alpha_3$ for $\alpha_3 < \alpha < 3\alpha_1$. Note that the constant 3 occurs from the pitch rate combinations used to construct the motion trajectory sets. If the matching angle is increased beyond $3\alpha_1$, separation will not occur at α_3 but the separation angle will be significantly reduced to a lower angle, α_1. Thus we have: $\alpha_{sep} = \alpha_1$ for $\alpha_m \geq 3\alpha_1$. These results are tabulated in table 4.1 below, and a graphical representation is given in figure 4.18.

Case A

α_m	α_{sep}
$0° \leq \alpha \leq \alpha_2$	α_2
$\alpha_2 < \alpha \leq \alpha_3$	α_m
$\alpha_3 < \alpha < 3\alpha_1$	α_3
$3\alpha_1 \leq \alpha < 60°$	α_1

Table 4.1 Separation model in equation form, case A.

For the case B trajectories with $\alpha_m \leq \alpha_1$, the first two motion segments are both completely below their respective constant pitch rate separation values, and separation occurs at α_2, associated with the third motion segment: $\alpha_{sep} = \alpha_2$ for $\alpha_m < \alpha_1$. However, as α_m is increased beyond α_1, separation occurs during the second motion segment resulting from a portion of this segment being above α_1. With increasing α_m, separation will continue to occur at α_1 until the α_m is increased sufficiently such that the second motion segment is entirely above α_1. The pitch rate ratios used in the trajectories (1/2 and 2) relate the transition angle to the matching angle by $\alpha_t = 2/3\alpha_m$. Thus $\alpha_t = \alpha_1$ when $\alpha_m = 1.5\alpha_1$, giving: $\alpha_{sep} = \alpha_1$ for $\alpha_1 \leq \alpha < 1.5\alpha_1$. Any further increase in α_m will increase α_{sep} with separation occurring at the beginning of the second motion segment. Since $\alpha_t = 2/3\alpha_m$, for the transition between the first two motion segments, $\alpha_{sep} = 2/3\alpha_m$ for $1.5\alpha_1 \leq \alpha < 1.5\alpha_3$. An increase in α_m beyond $1.5\alpha_3$ will cause α_t to be above α_3 and separation will occur at α_3 for $\alpha_m \geq 1.5\alpha_3$. These results are tabulated in table 4.2 below, and a graphical representation is given in figure 4.18.

Case B.

α_m	α_{sep}
$0° < \alpha < \alpha_1$	α_2
$\alpha_1 \leq \alpha < 1.5\alpha_1$	α_1
$1.5\alpha_1 \leq \alpha < 1.5\alpha_3$	$2/3\alpha_m$
$1.5\alpha_3 \leq \alpha < 60°$	α_3

Table 4.2 Separation model in equation form, case B.

The actual angles at which leading edge separation is detected are plotted vs matching angle in figures 4.19 through 4.22. Figures 4.19 and 4.20 correspond to case A trajectories with parent pitch rates of $\Omega^* = 0.05$ and $\Omega^* = 0.2$ respectively, while figures 4.21 and 4.22 correspond to case B trajectories with parent pitch rates of $\Omega^* = 0.05$ and $\Omega^* = 0.2$ respectively. Additionally, the separation values predicted by the model are indicated in these figures. The thin double lines in each figure represent the separation angles predicted by the model for a given matching angle. The spacing between these lines represent the uncertainty associated with depicting the onset of leading edge separation for a given pitch rate. This uncertainty primarily results from the framing rate of the CCD camera which gives an uncertainty in the airfoil motion starting time of ±10ms.

In figure 4.19 separation angles for case A trajectories with a parent pitch rate of $\Omega^* = 0.05$ are considered. For $0° < \alpha_m < 13.7°$ the model indicates that the separation angle should be 13.7° and independent of α_m. The experiments reveal a slight increase in the separation angle from 0.5° at $\alpha_m = 7°$ to 1.3° at $\alpha_m = 13°$. This suggests two things. One is that these low angle portions of the trajectory do have an influence on the separation process for this range of pitch rates. Secondly, the higher angle portion of the trajectory below the matching angle may have a greater influence on the separation angle than the lower angle portion for a given matching angle. The increasing delay in separation angle with increasing matching angle indicates that the higher angle portion of a motion trajectory is more sensitive to the instantaneous pitch rate than the lower angle portions in this pitch rate range.

For $13.7° < \alpha_m < 17.5°$ the model indicates that separation should occur instantaneously as the pitch rate is reduced from $\Omega^* = 0.10$ to 0.025 in these variable motion trajectories. The data show this trend. However, in general separation is delayed to a higher angle than predicted by in this α_m range. This may be due to the finite time needed for the separation to become visible in the experiments.

As the matching angle is increased further, the trajectories contain only two motion segments prior to the separation angle. By increasing the matching angle, the angle at which the transition from $\Omega^* = 0.025$ to $\Omega^* = 0.10$ is also increased. Thus for remaining trajectories in this figure, as far as separation is concerned, the effect of the pitch rate transition angle as the airfoil pitch rate is rapidly increased by a factor of four is being depicted. The model suggests that separation will be delayed to $\alpha_3 = 17.5$ for $\alpha_t < \alpha_1$.

For $17° < \alpha_m < 23°$, the separation angle remains relatively constant at $17°$. Note that the transition angle for $\alpha_m = 23°$ is $7.7°$. As the matching angle and thus transition angle is increased further, the existence of the lower pitch rate portion of the motion begins to take effect and a steady decrease in α_{sep} is observed for increasing α_m.

As α_m is increased beyond $3\alpha_1 = 32.1°$, the model suggests a rapid drop in α_{sep} to $10.7°$ and by causality should be independent of further increases in transition angle. However, the data shows the "double" separation described earlier. Note that the increasing trend of the higher angle data in this α_m range is most likely to be occurring from detecting the secondary event later in the separation process with increasing α_m. For higher α_m values, the secondary separation event is difficult to detect in the presence of flow field irregularities.

For the case A trajectories associated with the higher pitch rate range, $\Omega^* = 0.20$, it is evident from figure 4.20 that the model predicts the separation angles very satisfactorily for the majority of the cases. However, for $19° \leq \alpha_m \leq 24°$ separation occurs at a higher angle than associated with the model as in the lower pitch rate range. Over the remainder of the α_m values, the model is generally more accurate than for the lower pitch rate range.

In figure 4.21, the model also predicts the trends in the data for the case B trajectories with a parent pitch rate of $\Omega^* = 0.05$. For matching angles below $10.7°$ the

model suggests that the separation should occur at 13.7°, independent of matching angle. The data shows that the separation process occurs at a smaller angle than predicted. This indicates that that the higher angle portions in the trajectory below the matching angle have more influence on the flow development than the lower angle portions.

As the matching is increased beyond 10.7° the motions become two segment trajectories as far as separation is concerned. The experiment becomes a study of the effect of pitch rate transition angle as the airfoil is rapidly decelerated from $\Omega^* = 0.10$ to $\Omega^* = 0.025$. For a matching angles between 10.7° and 16.1° α_t is below α_1. The model suggests that the separation will occur at 10.7°. However the this does not occur in the data, and separation is $\dot{}$ delayed to a higher angle than 10.7°. The lowest separation angle observed is 11.9° which is a drop of 60% of the difference between α_1 and α_2. This delay in separation to a higher angle of attack is likely to be the result of the higher pitch rate motion segment at the low angle portion of the trajectory.

Comparing figure 4.22 (in which the separation angles are plotted for case B trajectories with a parent pitch rate of $\Omega^* = 0.20$) with figure 4.21 shows that the model is more satisfactory in the higher pitch rate range than for the lower pitch rate range. As for the trajectories with higher pitch rates, the model predicts the separation angles very satisfactorily for the majority of the α_m values. Note that for the portions of the model which α_{sep} was predicted to be equal to α_1, the error was only 17% of the difference between α_2 and α_1 for the higher pitch rate range, compared to 40% for the lower pitch rate range.

Based on the discussion above, it is evident that the model was very successful in capturing the behavior of the experimental data as well as being quantitatively close to the data especially for the higher pitch rate range. Collectively the results strongly support the assumption that the separation process is relatively insensitive to the motion history for these types of motion trajectories.

In order to obtain further insight from studies of this type of motion trajectories, it is suggested that future work be conducted to obtain a more quantitative description of the flow field evolution numerically, or with LDV (especially in the region near the leading edge of the airfoil). This would both supplement the trends indicated by the present work and provide a means to obtain a more detailed quantitative analysis of the motion history effects on separation and the high angle portion of the flow development.

CONCLUSIONS

1) The angle at which leading edge separation is detected increases with increasing pitch rate for the constant pitch rate motions studied. The separation angle shows a linear dependence on the square root of the pitch rate which is in agreement with the observations by Graham et. al. (1986).

2) The length of the initial recirculation region associated with leading edge separation decreases with increasing pitch rate for constant pitch rate motions.

3) In the case of constant pitch rate motions, the timing of the disturbances over the aft portion of the airfoil relative to leading edge separation is strongly pitch rate dependent. For the lower constant pitch rate values ($\Omega^* = 0.01$, 0.02 in this case), disturbances in the shear layer originate near the trailing edge of the airfoil and progress to the leading edge. For these pitch rates, the formation of a leading edge recirculation region is not evident from the flow visualization. With an increase in the pitch rate, $\Omega^* = 0.04$, 0.05, the shear layer disturbances are observed developing simultaneously with the onset of leading edge separation. Additionally, these disturbances develop simultaneously over a large portion of the airfoil. For higher constant pitch rate values $\Omega^* = 0.10$, 0.20, 0.40 the onset of leading edge separation is observed prior to the development of disturbances in the shear layer over the remainder of the airfoil.

4) The development and movement of the shear layer vortices are also strongly pitch rate dependent. For lower constant pitch rate values, $0.01 \leq \Omega^* \leq 0.04$ in this case, the shear layer rolls up into small vortices (often pairing) which sequentially convect into the wake. Moderate pitch rate values of $\Omega^* = 0.05$, 0.10 correspond to the shear layer

rolling up into small vortices which in general amalgamate into a single larger shear layer vortex. The resulting shear layer vortex convects into the wake. The shear layer vortices associated with the highest pitch rates $\Omega^* = 0.20, 0.40$ also amalgamated into a single shear layer vortex, however instead of convecting into the wake, this shear layer vortex gets entrained or torn up by the dynamic stall vortex during the high angle portion of the motion.

5) The spacing between multiple shear layer vortices which develop on the suction surface of the airfoil are nearly always spaced c/6 apart during their formation. This is independent of pitch rate.

6) For the variable motion trajectories studied in the higher pitch rate range, the instantaneous pitch rate through the static stall angle is not a controlling parameter in the subsequent flow development. While for the lower pitch rate range, the instantaneous pitch rate through the static stall angle influences the angle at which leading edge separation is detected (however it is not a controlling parameter).

7) For the variable motion trajectories in the lower pitch rate range, the portions of the motion trajectory below the static stall angle influence the angle at which leading edge separation is detected. For the higher pitch rate range, portions of the motion trajectory above the static stall angle are shown not to influence the onset of leading edge separation.

8) Leading edge separation angles associated with the variable motion trajectories in the higher pitch rate range, are less sensitive to the low angle portions of the motion trajectory than in the lower pitch rate range.

9) As indicated by the model presented in this work, the assumption that the leading edge separation is insensitive to motion history is sufficient to capture the behavior of the separation angles associated with the variable motion trajectories presented.

REFERENCES

ACHARYA, M. & METWALLY, M. 1990 Evolution of the Unsteady Pressure Field and Vorticity Production at the Surface of a Pitching Airfoil. AIAA-90-1472

CARR, L. W. 1988 Progress in Analysis and Prediction of Dynamic Stall. *AIAA J.*, Vol. 25, No. 1, pp. 6-17.

CARTA, F.O. 1971 Effect of Unsteady Pressure Gradient Reduction on Dynamic Stall Delay. *J. Aircraft*, Vol. 8, No.10, pp. 839-841.

CHOW, C. Y. & CHIU, C. S. 1986 Unsteady Loading on an Airfoil Due to Vortices Released Intermittently from its Surface AIAA-85-0130.

DMC-600 Series, User Manual: Motion Controller Galil Motion Control, Inc.: 1054 Elwell Court, Palo Alto, CA 94303 Telephone:(415)964-6494, Telex:171-409.

FRANCIS, M. S. & KEESEE, J. E. 1985 Airfoil Dynamic Stall Performance With Large-Amplitude Motions. *AIAA J.*, Vol. 23, No. 11, pp. 1653-1659.

GENDRICH, C. P. 1991 Private communication.

GRAHAM, G. M. & STRICKLAND, J. H. 1986 An Experimental Investigation of an Airfoil Pitching at Moderate to High Rates to Large Angles of Attack. AIAA-86-0008.

JUMPER, E. J., DIMMICK, R. L. & ALLAIRE, A. J. S. 1987 The Effect of Pitch Location on Dynamic Stall. *ASME Forum on Unsteady Flow Separation*, FED-Vol. 52, Ed. K. N. Ghia

JUMPER, E. J. & STEPHEN, E.J. 1988 Toward Unsteady Lift Augmentation: An Assessment of the Roll of Competing Phenomena in Dynamic Stall. *Proceedings of Workshop II on Unsteady Separation*, Frank J. Seiler Research Labatory, FJSRL-TR-88-0004.

JUMPER, E. J., SHRECK, S. J. & DIMMICK, R. L. 1986 Lift-Curve Characteristics for an Airfoil Pitching at Constant Rate. AIAA-86-0117.

KOOCHESFAHANI, M. M., SMILJANOVSKI, V. & BROWN, T. A. 1990 Effect of Initial Acceleration on the Development of the Flow Field for an Airfoil Pitching at Constant Rate. *NASA/AFOSR/ARO Workshop on Physics of Forced Unsteady Separation.*

LORBER, P. F. & CARTA, F. O. 1987 Airfoil Dynamic Stall at Constant Pitch Rate and High Reynolds Number. AIAA-87-1329

McCROSKEY, W.J. 1973 Inviscid Flowfield of an Unsteady Airfoil. *AIAA J.*, Vol. 11, No. 8, pp. 1130-1137.

McCROSKEY, W. J. 1981 The Phenomenon of Dynamic Stall. NASA TM-81264, March 1981.

McCROSKEY, W. J., CARR, L. W. & McALISTER, K. W. 1976 Dynamic Stall Experiments on Oscillating Airfoils. *AIAA J.*, Vol. 14, No. 1, pp. 57-63.

ROBINSON, M., WALKER, J. & WHISSLER, J. 1988 Unsteady Surface Pressure Measurements on a Pitching Rectangular Wing. *Proceedings of Workshop II on Unsteady Separation*, Frank J. Seiler Research Labatory, FJSRL-TR-88-0004.

SCHRAUB, F. A., KLINE, S. J., JENRY, J., RUNSTADLER, JR., P. W. & LITTEL, A. 1965 Use of Hydrogen Bubbles for Quantitative Determination of Time-Dependent Velocity Fields in Low-Speed Water Flows. *J. Basic Engineering*, Vol. 87, pp. 429-444.

SMITH, C. R. & WALKER, J. D. A. 1990 Some Aspects of Unsteady Separation. *NASA/AFOSR/ARO Workshop on Physics of Forced Unsteady Separation.*

VISBAL, M.R. 1990 On Some Aspects of Airfoil Dynamic Stall. *Presented at the ASME Synopsium on Non-Steady Fluid Dynamics, June 4-7, 1990, Toronto, Canada.*

VISBAL, M. R. 1991 On the Formation and Control of the Dynamic Stall Vortex on a Pitching Airfoil. AIAA-91-0006.

WALKER, J., HELIN, H. & CHOU, D. 1985 Unsteady Surface Pressure Measurements on a Pitching Airfoil. AIAA-85-0532.

WALKER, J. M., HELIN, H. E. & STRICKLAND, J. H. 1986 An Experimental Investigation of an Airfoil Undergoing Large-Scale Pitching Motions. *AIAA J.*, Vol. 23, No. 8, pp. 1141-1142

		Re x 10^4	c/h	airfoil
▽	Lorber and Carta (1988)	200-400	.18	SSC-A09
○	Koochesfahani, Brown, and Smiljanovski (1990)	.8	.14	NACA 0012
□	Visbal (1990)	1.0	0	NACA 0015
△	Walker, Helin, and Chou (1985)	4.8-19	.25	NACA 0015
●	Walker, Helin, and Strickland (1985)	4.5	.25	NACA 0015
■	Acharya and Metwally (1990)	2.8-12	.5	NACA 0012
+	Francis and Keesee (1985)	7.7	.25	NACA 0012
⊕	Francis and Keesee (1985)	17	.33	NACA 64A012(13)
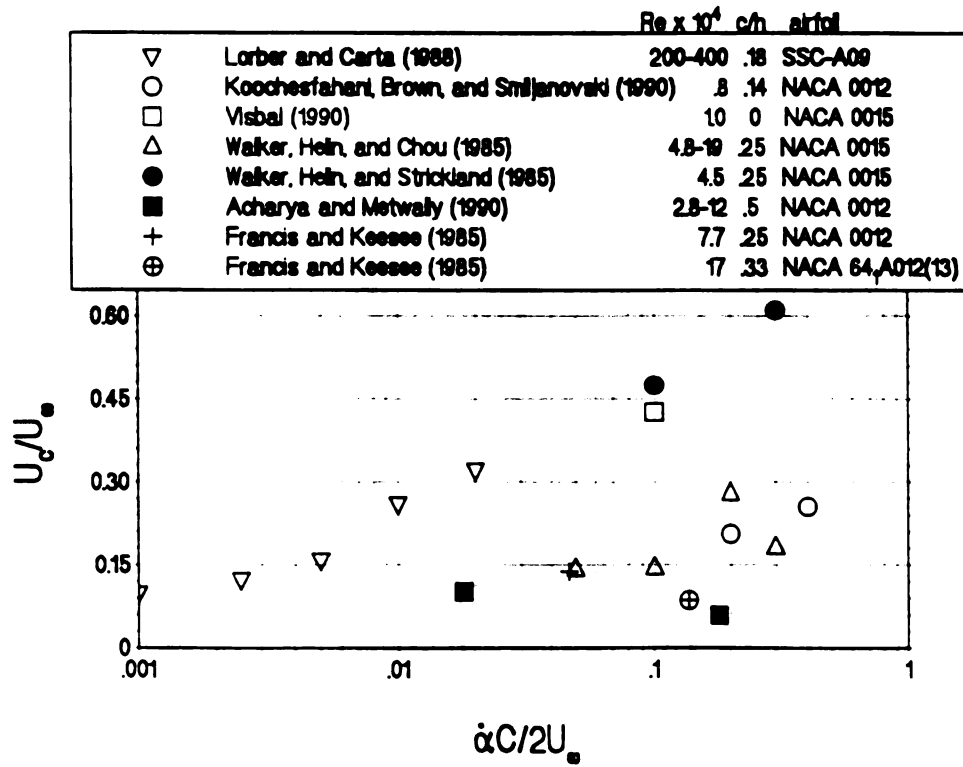
Figure 1.1   Vortex convection speeds from various authors.

DOWNSTREAM WINDOW

RETURN PLENUM

FLEXIBLE COUPLING

INSTRUMENT RAILS
STAINLESS STEEL, 1" DIA.

SAR PLEXIGALSS TEST SECTION

PIPE FLANGE/SADDLE

STEEL FRAME (TYPICAL)

14" DIA. PVC PIPE

SCREEN PACK ACCESS COVER

LEVELING PAD (TYPICAL)

AXIAL PUMP ASSEMBLY

MANWAY COVER/AIR DOME

CONTROLLER
VARIABLE FREQUENCY
BEVEL DRIVE
20 HP AC MOTOR

4'-2"

8'-0"

30'-0"

8'-0"

3'-2"

4'-6"

2'-0"
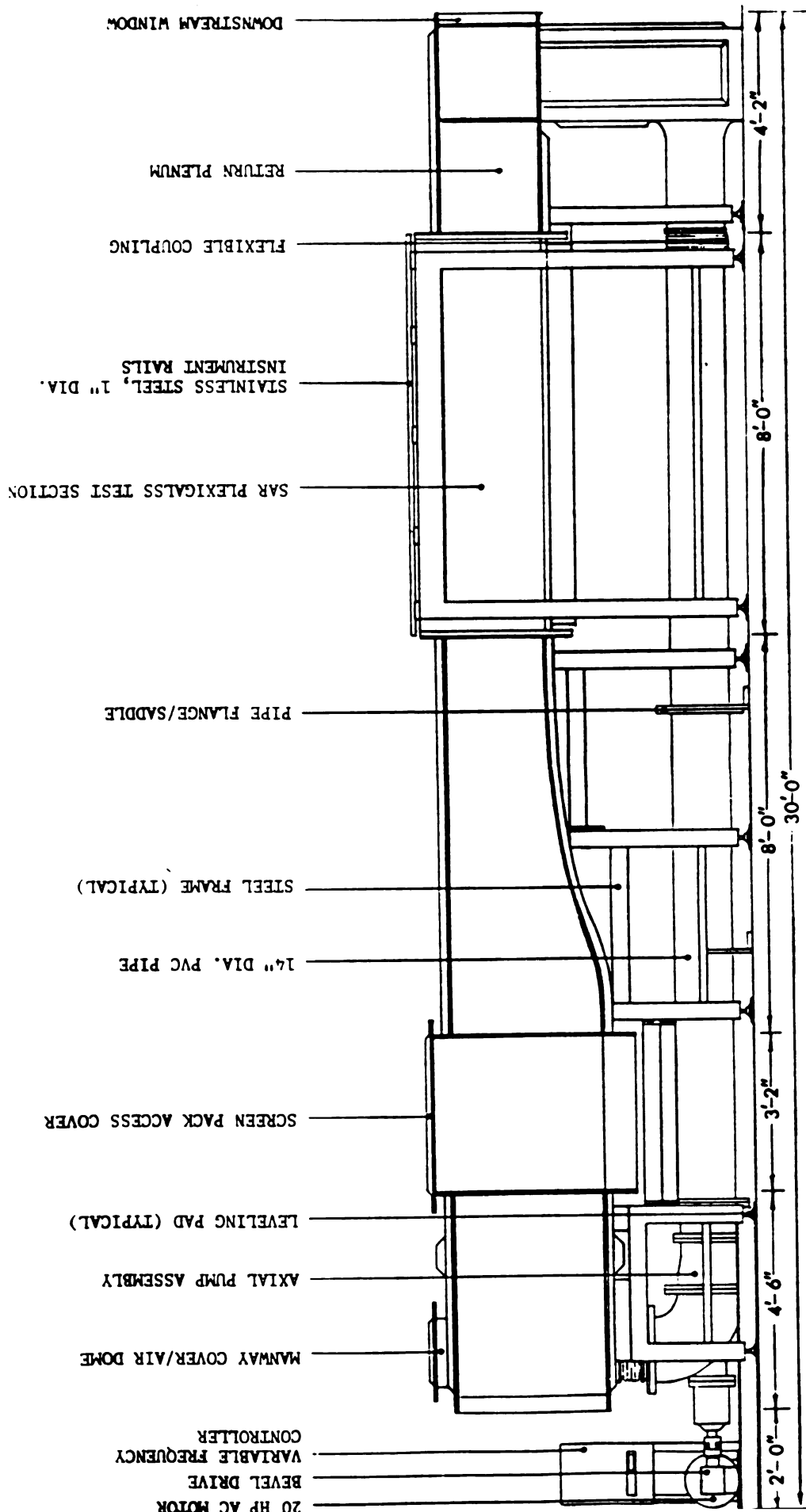
Figure 2.1. Schematic of water channel facility.

Cross Supports
(typical)

False
Wall

Motor

Drive
Linkage

Drive
Disk

Airfoil

U_∞
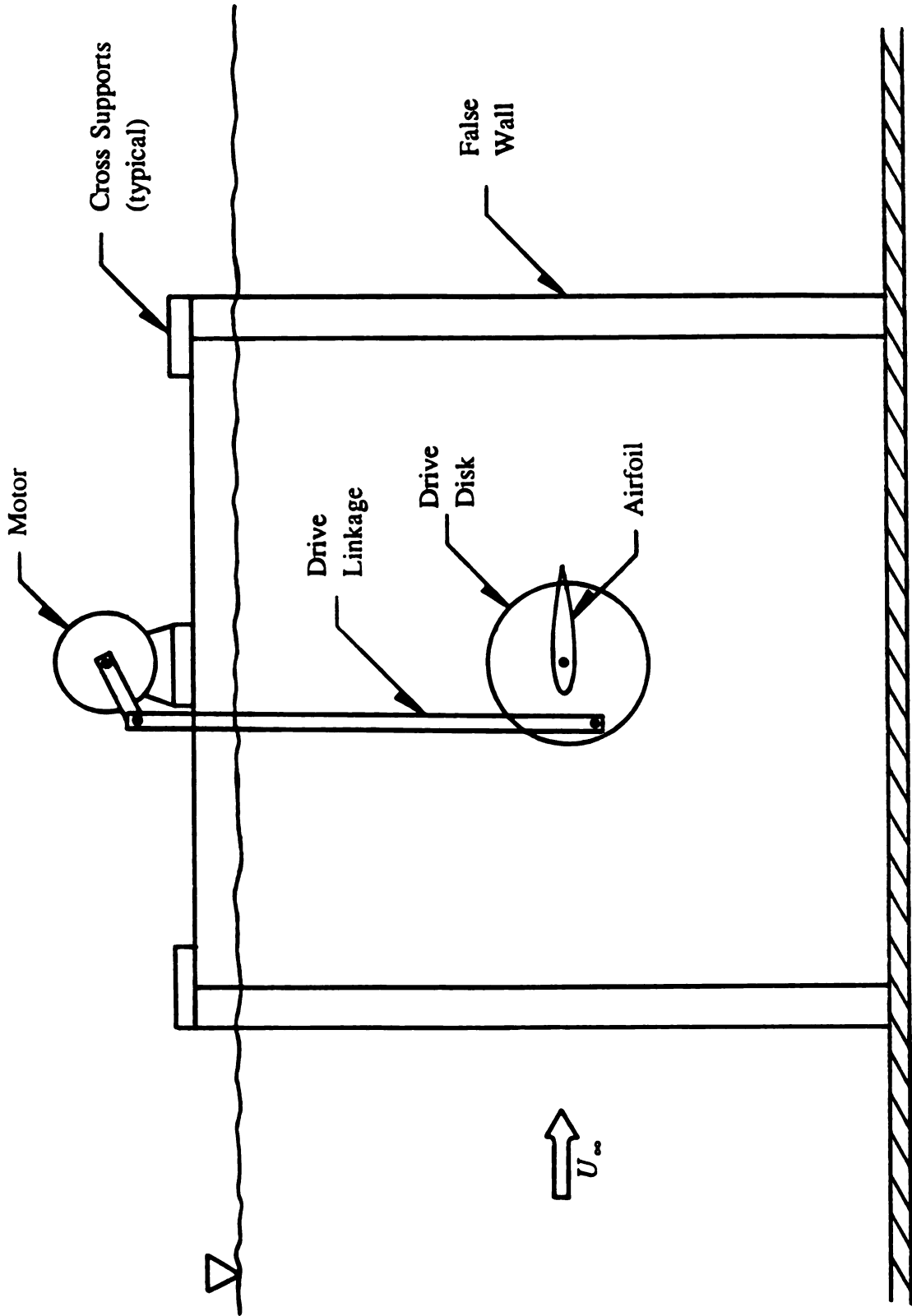
Figure 2.2   Airfoil and support assembly.
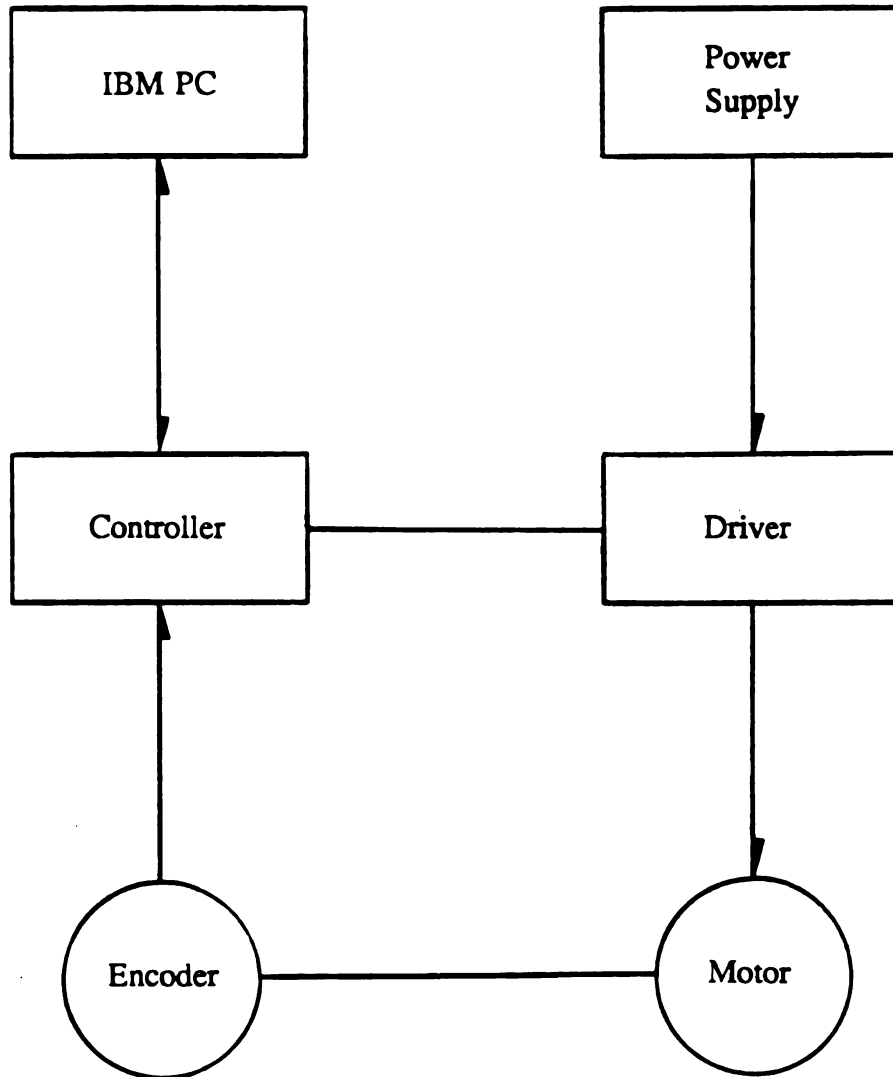
Figure 2.3 Elements of control system.
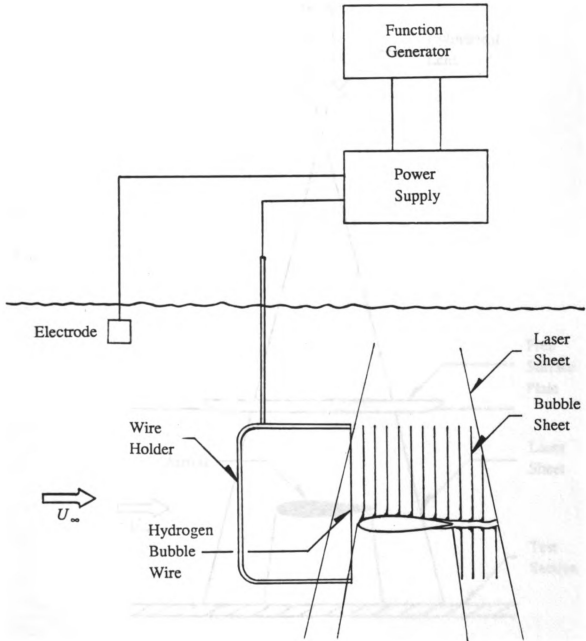
Figure 2.4   Hydrogen bubble arrangement.
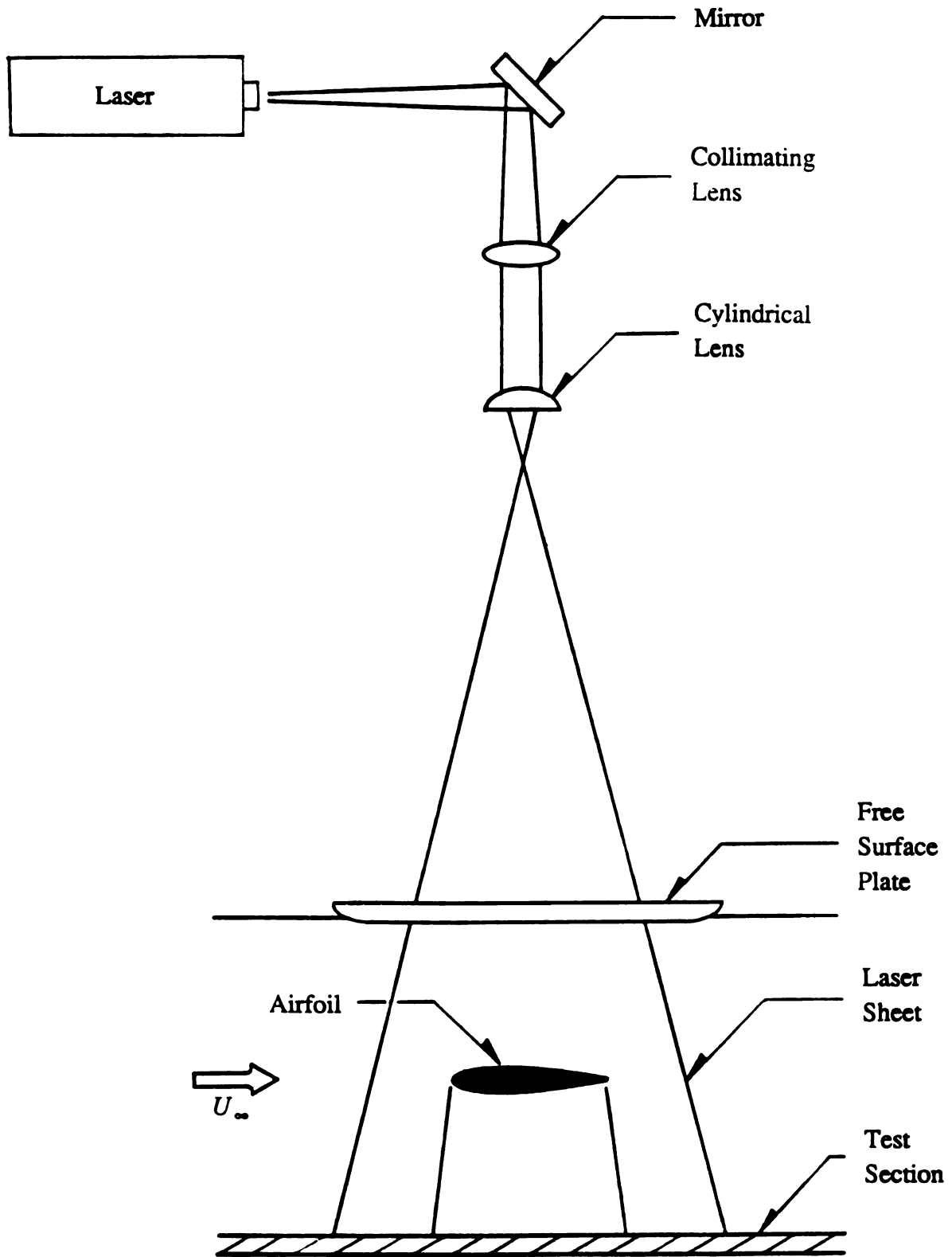
Figure 2.5 Laser sheet arrangement.
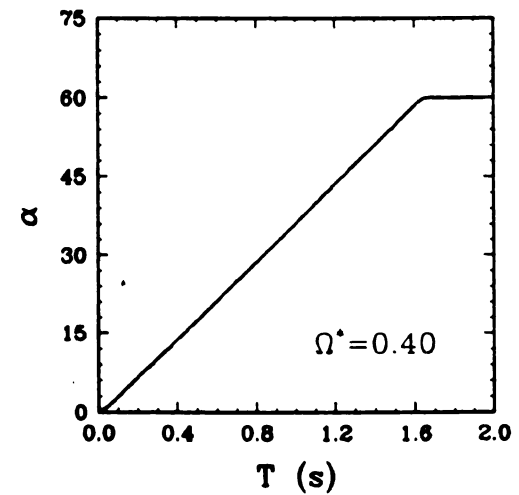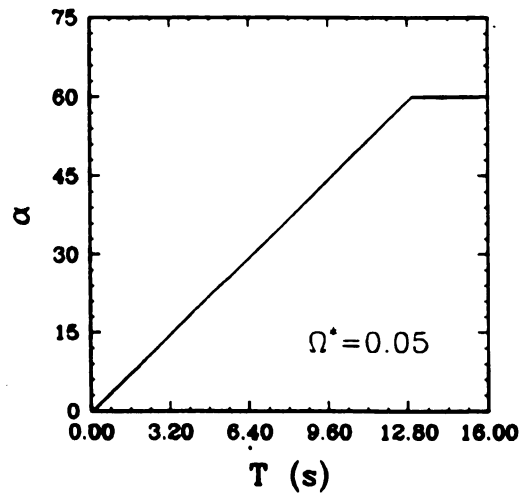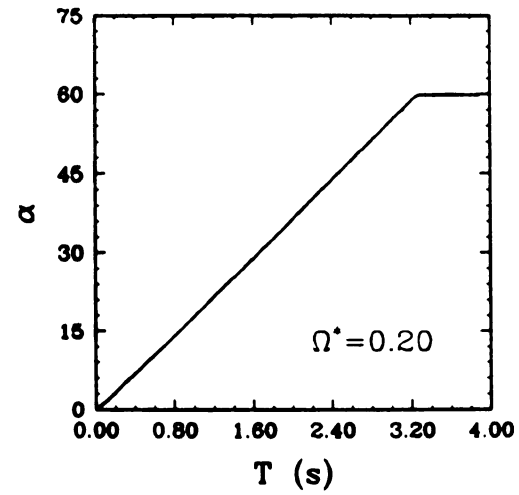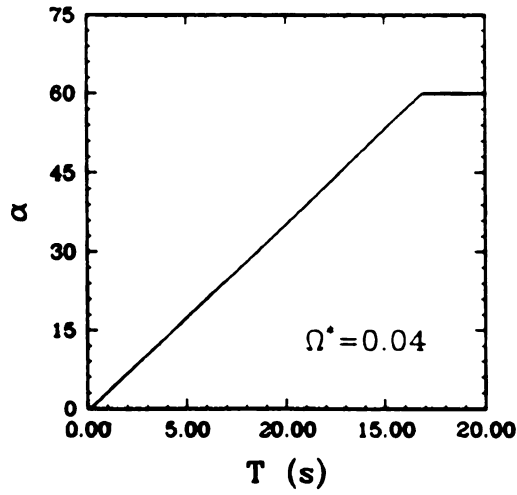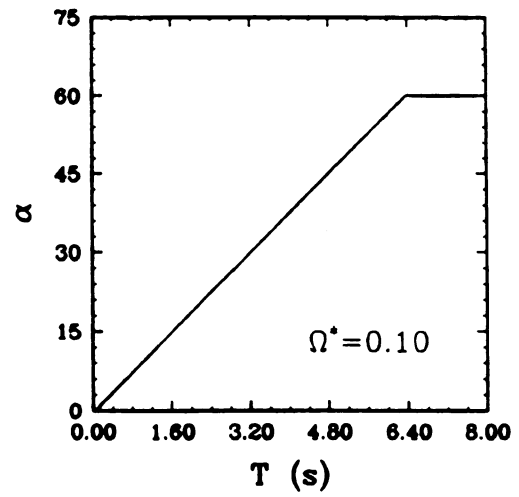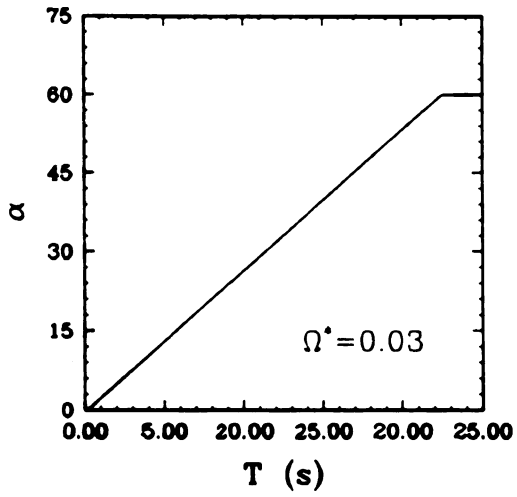
Figure 3.1. Actual airfoil trajectories for constant pitch rate motions.

$\alpha = 00.0°$ $\alpha = 08.3°$

$\alpha = 07.7°$ $\alpha = 08.5°$

$\alpha = 08.1°$ $\alpha = 08.8°$

$\alpha = 08.2°$ $\alpha = 09.0°$

Figure 3.2 Evolution of flow field on suction surface.

Constant Pitch Rate Motion, $\Omega^* = 0.02$.

$\alpha = 09.1°$
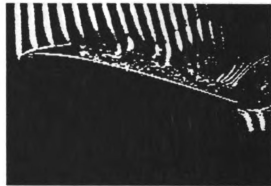
$\alpha = 11.4°$

$\alpha = 09.5°$

$\alpha = 12.4°$

$\alpha = 09.6°$

$\alpha = 14.7°$

$\alpha = 10.4°$

$\alpha = 16.1°$

Figure 3.2 Continued.

Constant Pitch Rate Motion, $\Omega^* = 0.02$.

$\alpha = 00.0°$

$\alpha = 11.9°$

$\alpha = 06.4°$

$\alpha = 12.2°$

$\alpha = 10.9°$

$\alpha = 12.3°$

$\alpha = 11.5°$

$\alpha = 12.6°$
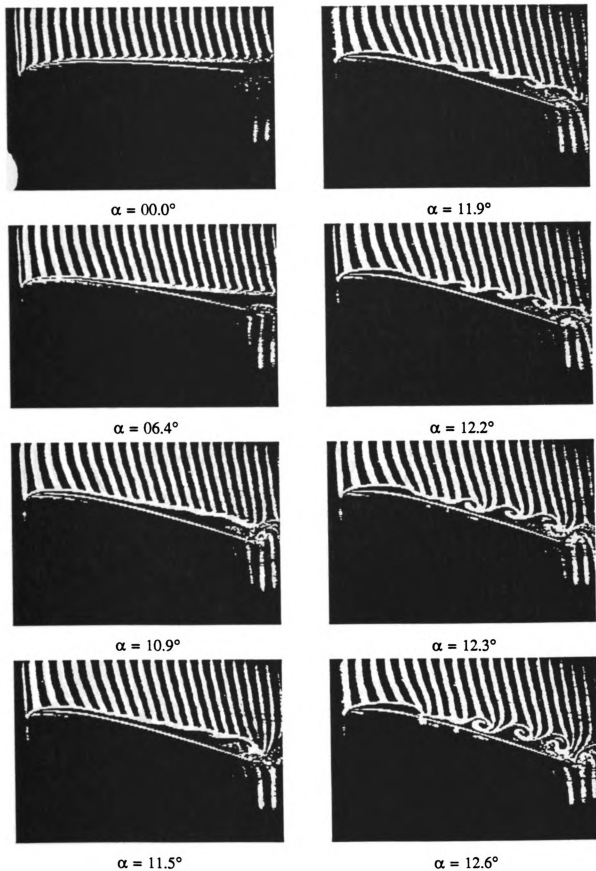
Figure 3.3 Evolution of flow field on suction surface.

Constant Pitch Rate Motion, $\Omega^* = 0.04$.

$\alpha = 12.8°$

$\alpha = 17.0°$

$\alpha = 13.3°$
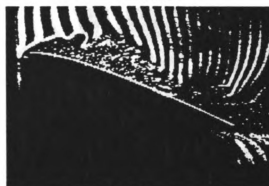
$\alpha = 18.4°$

$\alpha = 14.2°$

$\alpha = 21.4°$

$\alpha = 15.0°$
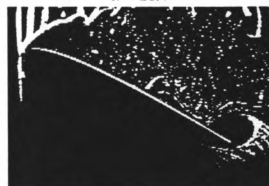
$\alpha = 24.5°$

Figure 3.3 Continued.

Constant Pitch Rate Motion, $\Omega^* = 0.04$.

$\alpha = 00.0°$ $\alpha = 18.4°$

$\alpha = 12.2°$ $\alpha = 19.6°$

$\alpha = 16.7°$ $\alpha = 20.6°$

$\alpha = 17.5°$ $\alpha = 22.2°$
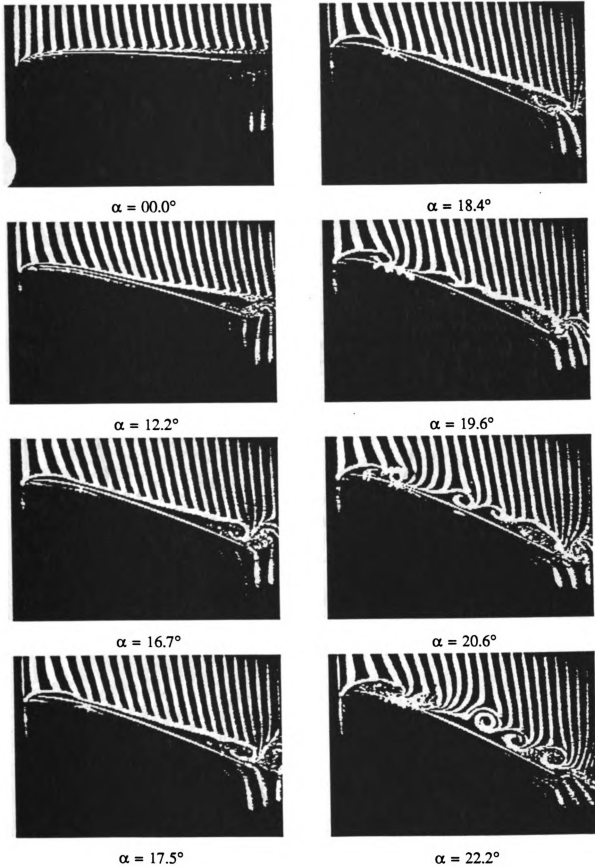
Figure 3.4 Evolution of flow field on suction surface.

Constant Pitch Rate Motion, $\Omega^* = 0.10$.
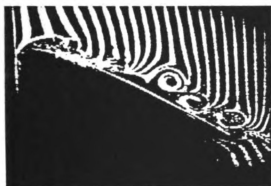
$\alpha = 22.8°$

$\alpha = 25.7°$

$\alpha = 23.4°$

$\alpha = 28.1°$

$\alpha = 24.0°$
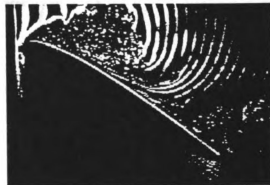
$\alpha = 31.2°$

$\alpha = 24.7°$
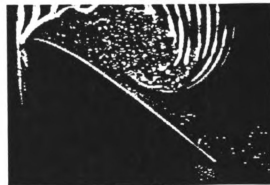
$\alpha = 34.4°$

Figure 3.4 Continued.

Constant Pitch Rate Motion, $\Omega^* = 0.10$.

$\alpha = 00.0°$ $\alpha = 23.3°$
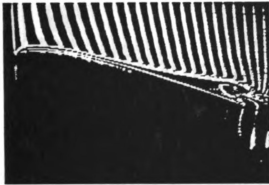
$\alpha = 13.9°$ $\alpha = 23.9°$
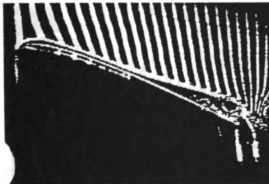
$\alpha = 20.1°$ $\alpha = 24.6°$

$\alpha = 22.0°$ $\alpha = 25.0°$

Figure 3.5 Evolution of flow field on suction surface.

Constant Pitch Rate Motion, $\Omega^* = 0.20$.
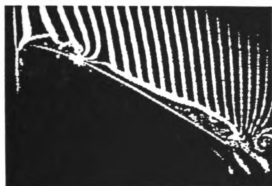
$\alpha = 26.2°$
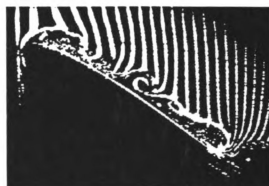
$\alpha = 31.2°$

$\alpha = 27.4°$

$\alpha = 33.7°$
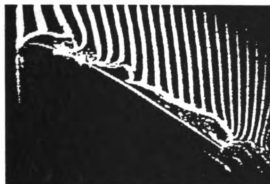
$\alpha = 28.6°$
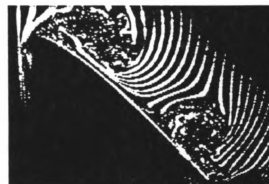
$\alpha = 40.6°$
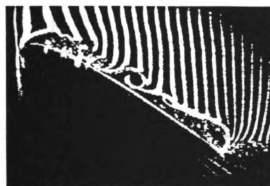
$\alpha = 30.0°$
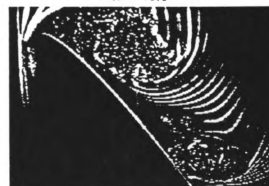
$\alpha = 46.7°$

Figure 3.5 Continued.

Constant Pitch Rate Motion, $\Omega^* = 0.20$.
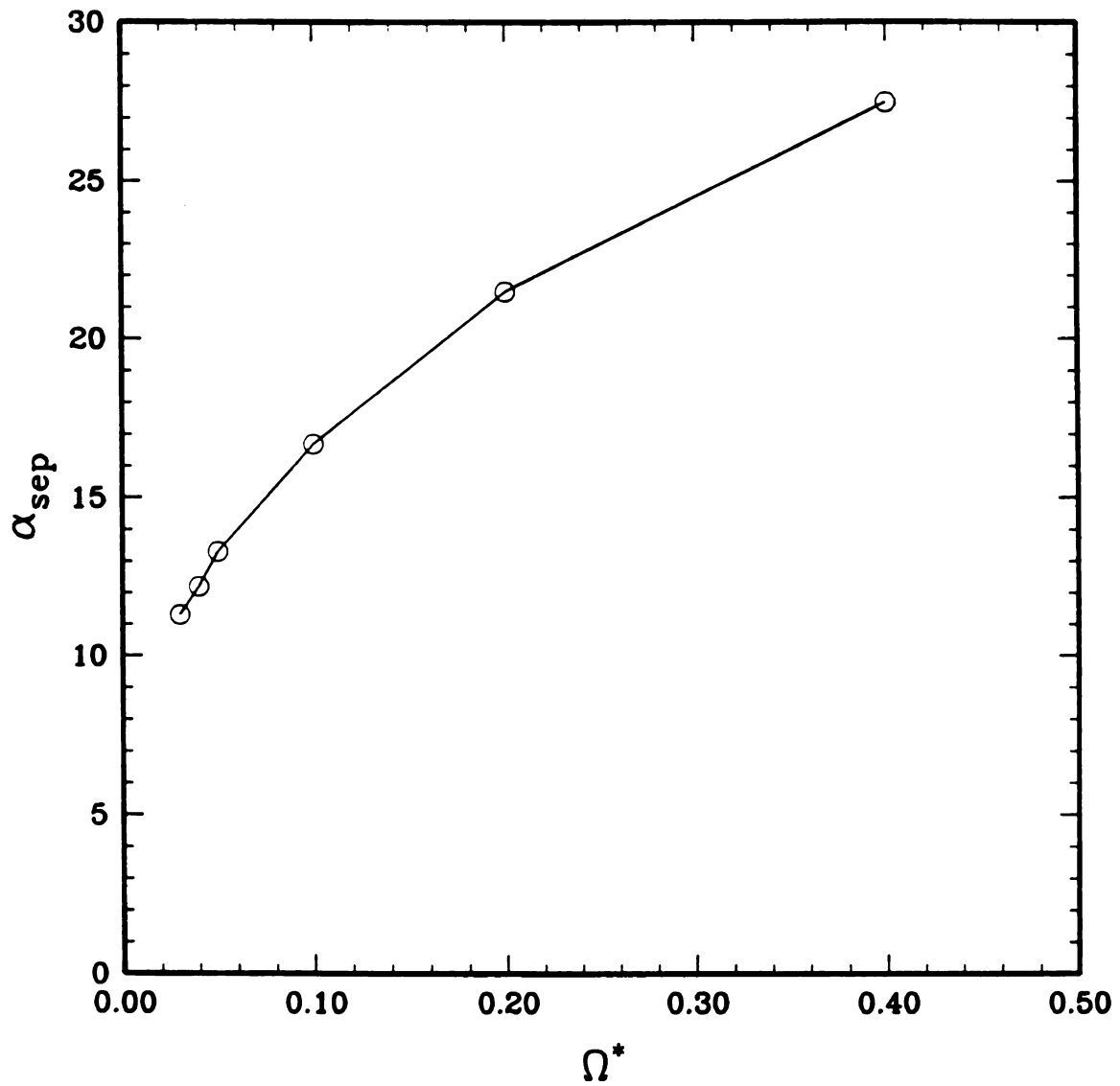
Figure 3.6. Angle at which leading edge separation is detected, α_{sep}, vs pitch rate, Ω^*.
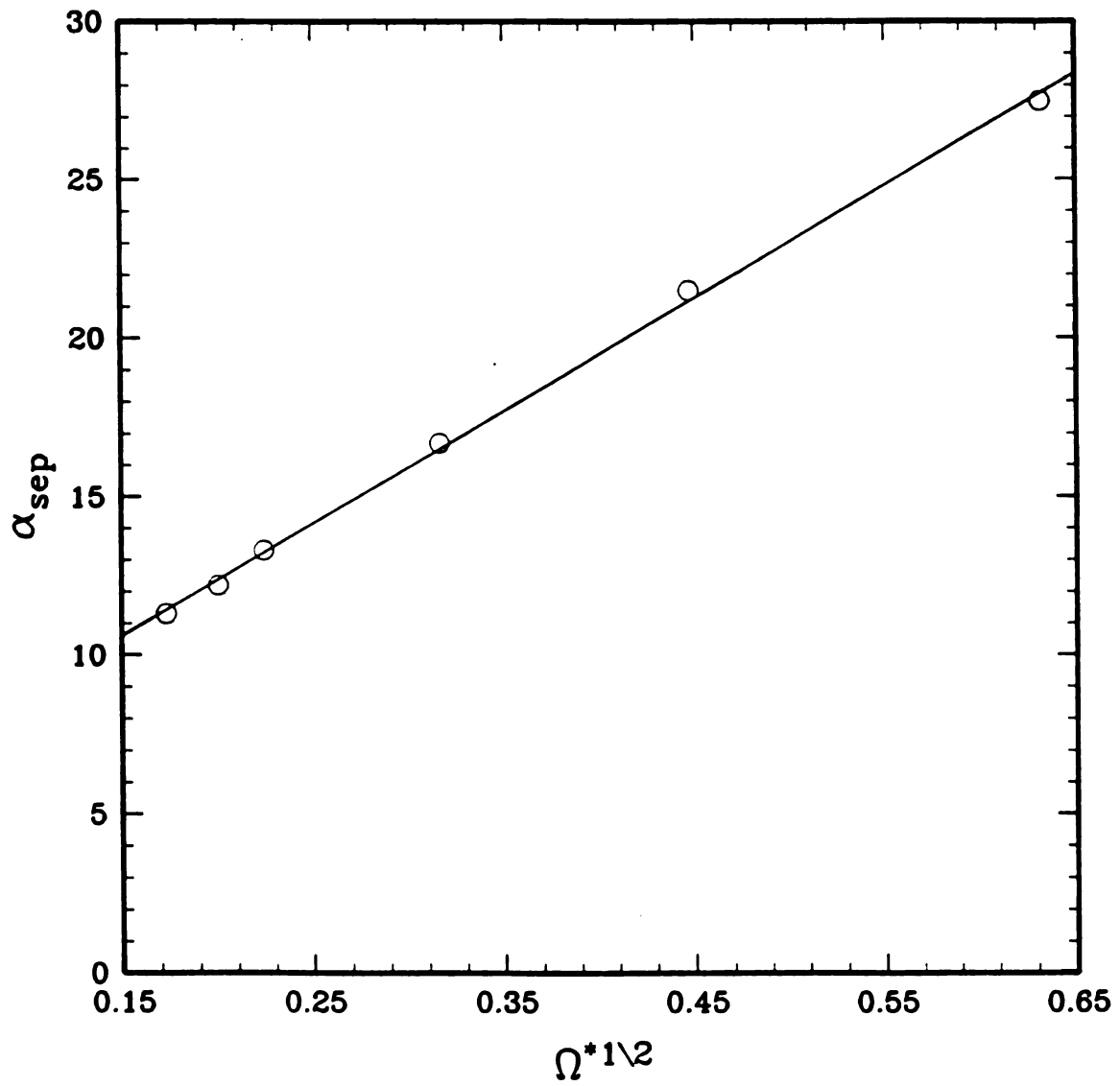
Figure 3.7. Angle at which leading edge separation is detected, α_{sep}, vs square root of pitch rate, $\Omega^{*1/2}$.
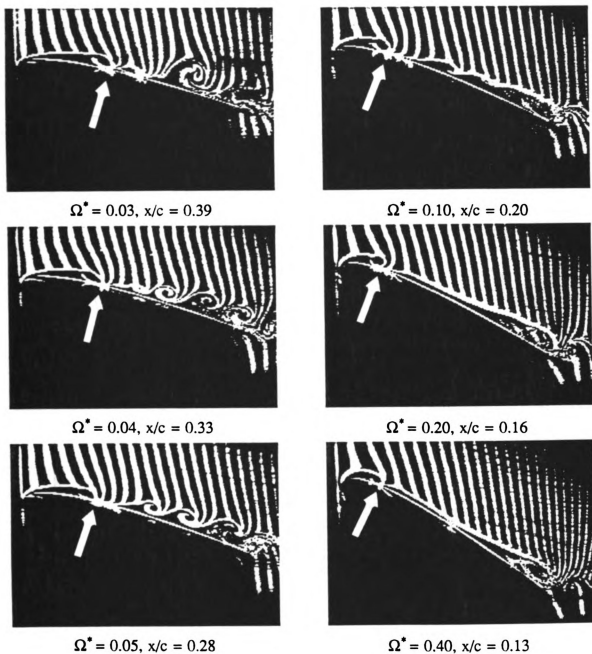
Figure 3.8 Initial leading edge recirculation region on suction surface.
Constant Pitch Rate Motions, $0.03 \leq \Omega^* \leq 0.40$.
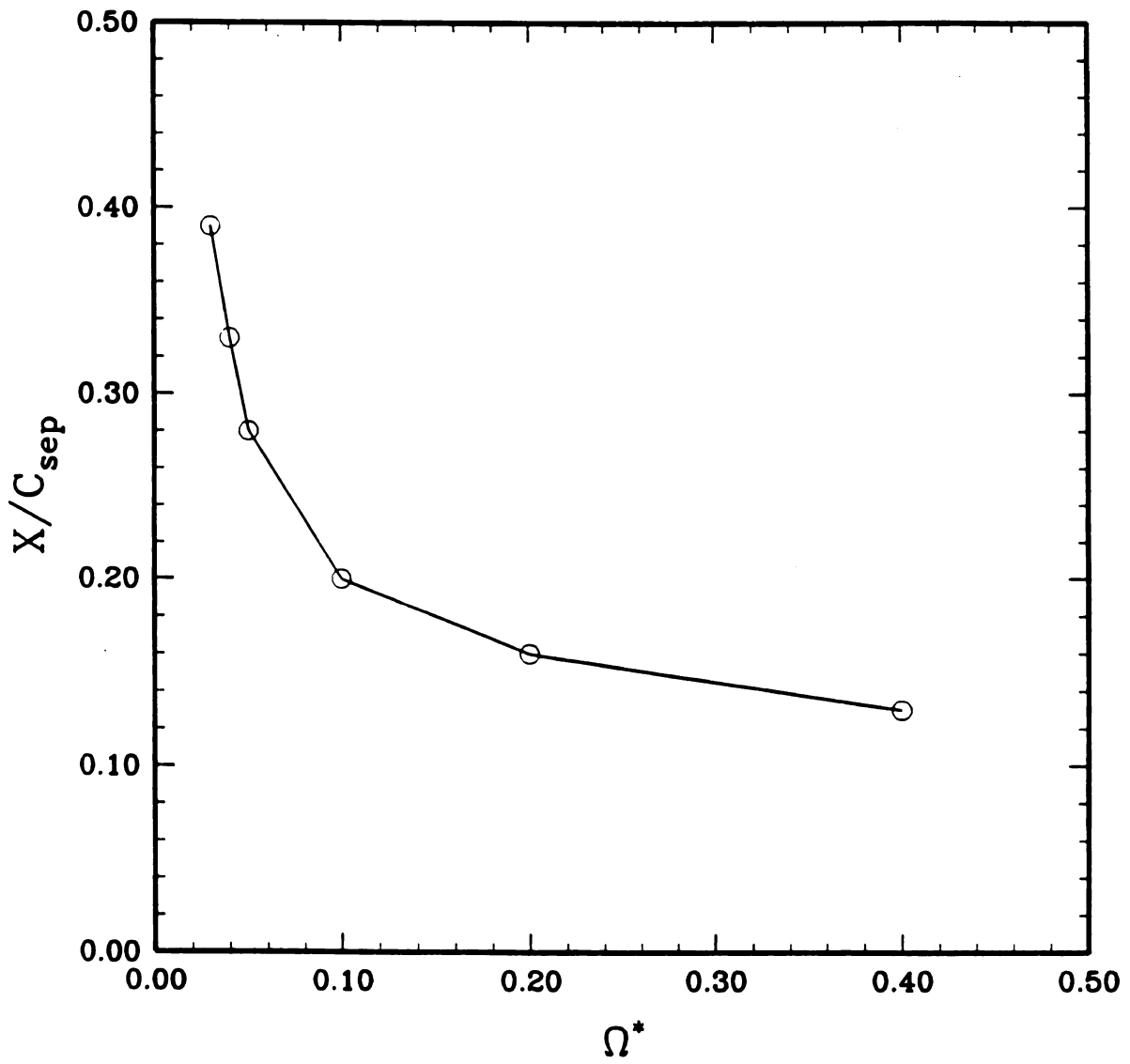
Figure 3.9. Initial chordwise extent of leading edge recirculation region vs pitch rate.
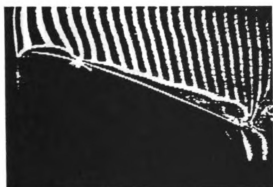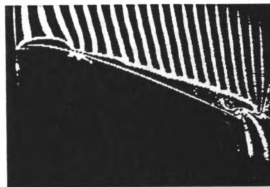
$\alpha = 18.4°$ $\alpha = 18.4°$

$\alpha = 19.6°$ $\alpha = 19.6°$

$\alpha = 20.6°$ $\alpha = 20.6°$

$\alpha = 22.2°$ $\alpha = 22.2°$
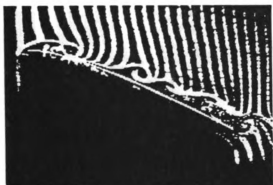
Run #1   Run #2

Figure 3.10   Repeated runs (Constant Pitch Rate Motion, $\Omega^* = 0.10$).

$\alpha = 08.3°$ $\alpha = 08.3°$

$\alpha = 08.5°$ $\alpha = 08.5°$

$\alpha = 08.8°$ $\alpha = 08.8°$

$\alpha = 09.0°$ $\alpha = 09.0°$
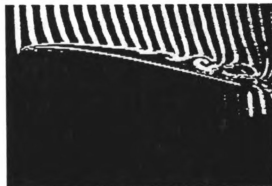
Run #1   Run #2

Figure 3.11. Repeated runs (Constant Pitch Rate Motion, $\Omega^* = 0.02$).

$\alpha = 09.1°$

$\alpha = 09.1°$

$\alpha = 09.5°$

$\alpha = 09.5°$

$\alpha = 09.6°$

$\alpha = 09.6°$

$\alpha = 10.4°$

Run #1

$\alpha = 10.4°$

Run #2

Figure 3.11. Continued.
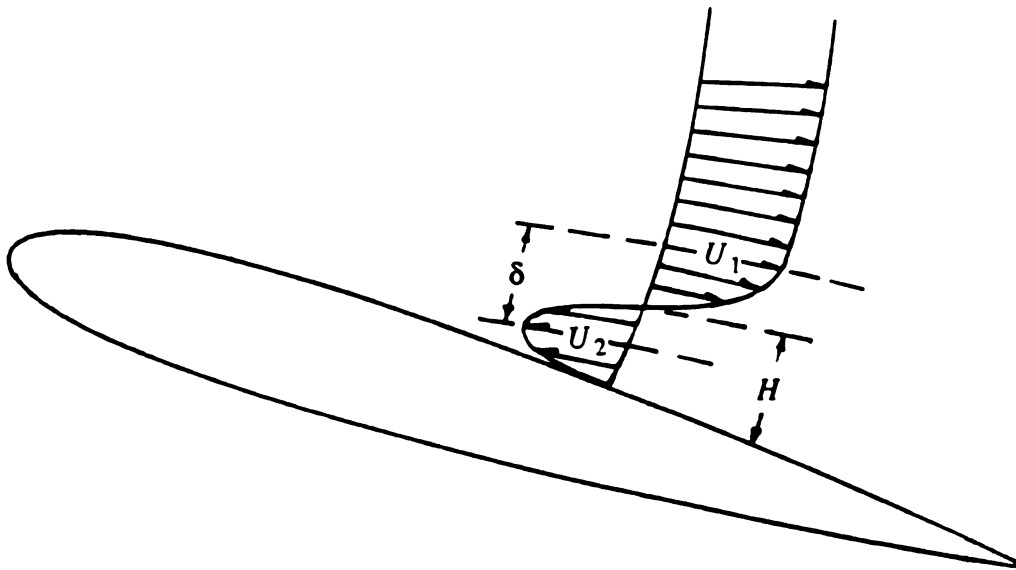
Figure 3.12. Schematic of reverse flow velocity profile.

$\alpha = 00.0^{\circ}$, t = 0.00s

$\alpha = 09.6^{\circ}$, t = 5.70s

$\alpha = 11.4^{\circ}$, t = 6.70s

$\alpha = 07.8^{\circ}$, t = 4.70s

$\alpha = 10.0^{\circ}$, t = 5.90s

$\alpha = 11.8^{\circ}$, t = 6.90s

$\alpha = 09.0^{\circ}$, t = 5.30s

$\alpha = 10.4^{\circ}$, t = 6.10s

$\alpha = 12.2^{\circ}$, t = 7.10s

$\alpha = 09.3^{\circ}$, t = 5.50s

$\alpha = 10.7^{\circ}$, t = 6.30s

$\alpha = 12.9^{\circ}$, t = 7.50s

$\alpha = 09.4^{\circ}$, t = 5.60s

$\alpha = 11.1^{\circ}$, t = 6.50s

$\alpha = 14.3^{\circ}$, t = 8.30s
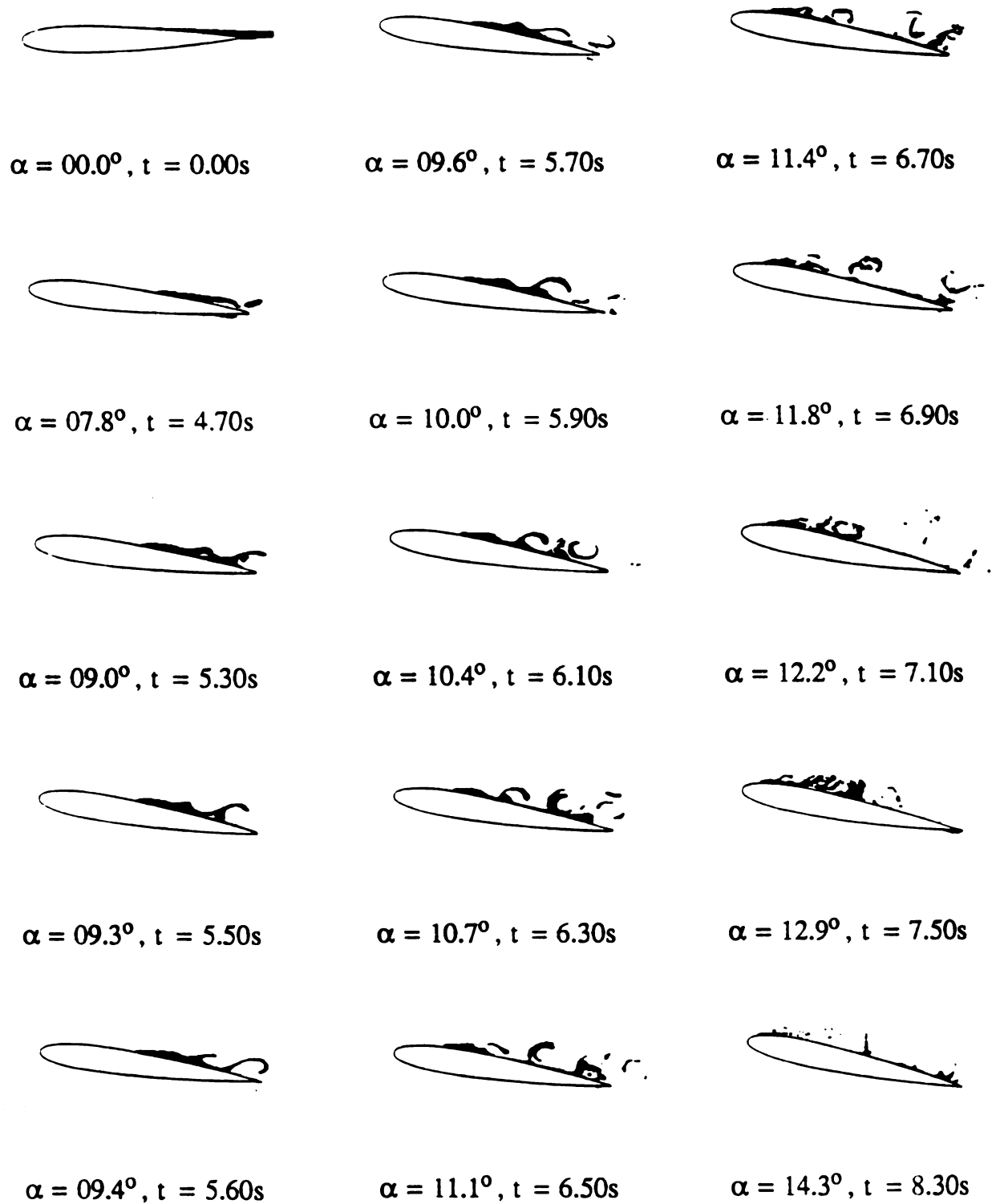
Figure 3.13. Evolution of flow field marked by dye deposited on suction surface, $\Omega^* = 0.02$.

$\alpha = 00.0^\circ$, t = 0.00s

$\alpha = 11.9^\circ$, t = 3.47s

$\alpha = 14.2^\circ$, t = 4.13s

$\alpha = 09.1^\circ$, t = 2.67s

$\alpha = 12.3^\circ$, t = 3.60s

$\alpha = 14.8^\circ$, t = 4.27s

$\alpha = 10.0^\circ$, t = 2.93s

$\alpha = 12.8^\circ$, t = 3.73s

$\alpha = 15.5^\circ$, t = 4.47s

$\alpha = 10.9^\circ$, t = 3.20s

$\alpha = 13.3^\circ$, t = 3.87s

$\alpha = 16.3^\circ$, t = 4.67s

$\alpha = 11.5^\circ$, t = 3.33s

$\alpha = 13.8^\circ$, t = 4.00s

$\alpha = 17.0^\circ$, t = 4.87s
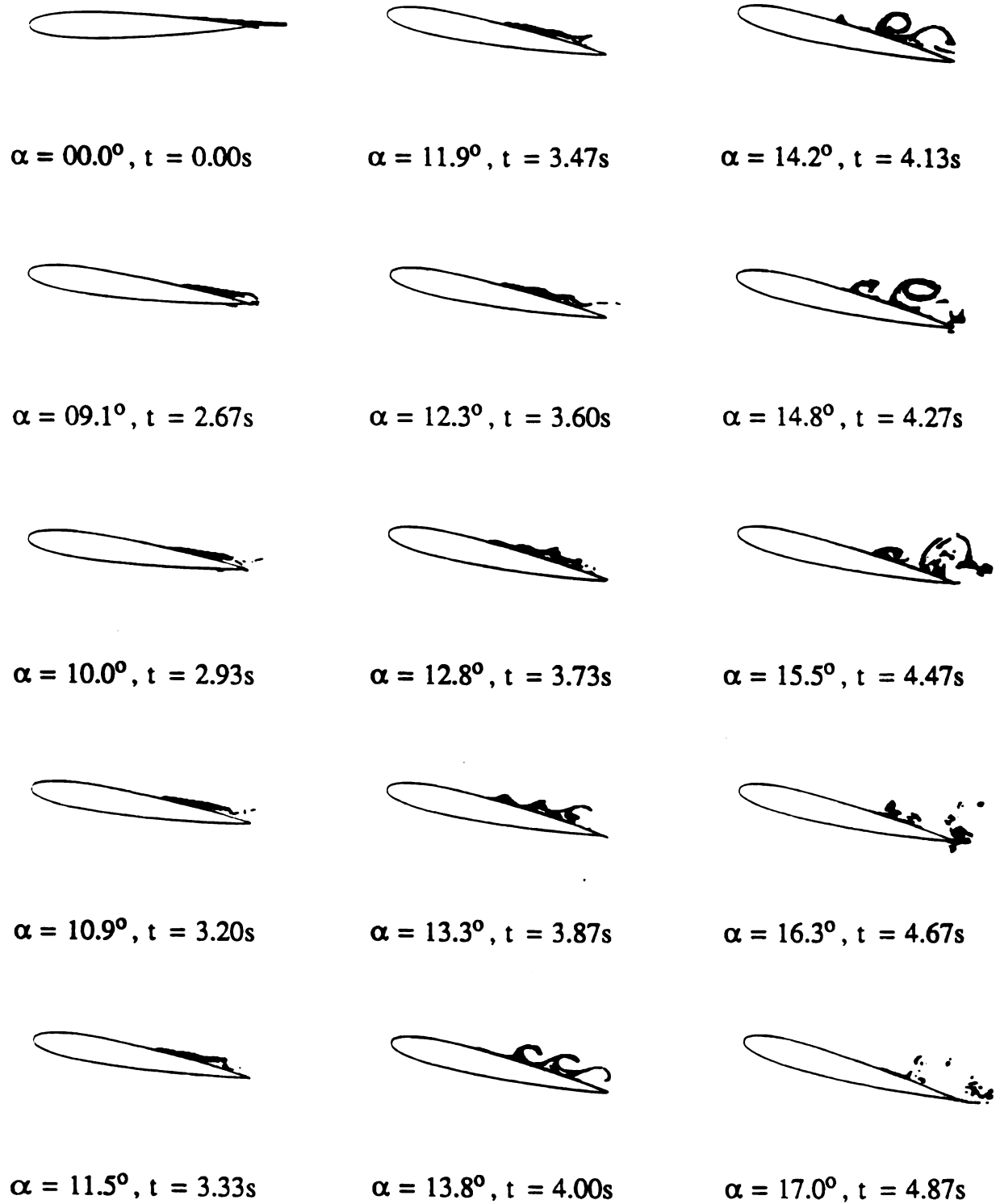
Figure 3.14. Evolution of flow field marked by dye deposited on suction surface, $\Omega^* = 0.04$.

$\alpha = 00.0^{\circ}$, t = 0.00s $\alpha = 23.6^{\circ}$, t = 2.53s $\alpha = 29.3^{\circ}$, t = 3.13s

$\alpha = 12.2^{\circ}$, t = 1.33s $\alpha = 24.9^{\circ}$, t = 2.67s $\alpha = 30.5^{\circ}$, t = 3.27s

$\alpha = 18.7^{\circ}$, t = 2.00s $\alpha = 26.1^{\circ}$, t = 2.80s $\alpha = 33.7^{\circ}$, t = 3.60s

$\alpha = 21.8^{\circ}$, t = 2.33s $\alpha = 28.0^{\circ}$, t = 3.00s $\alpha = 40.0^{\circ}$, t = 4.27s

$\alpha = 23.0^{\circ}$, t = 2.47s $\alpha = 28.6^{\circ}$, t = 3.07s $\alpha = 45.1^{\circ}$, t = 4.80s
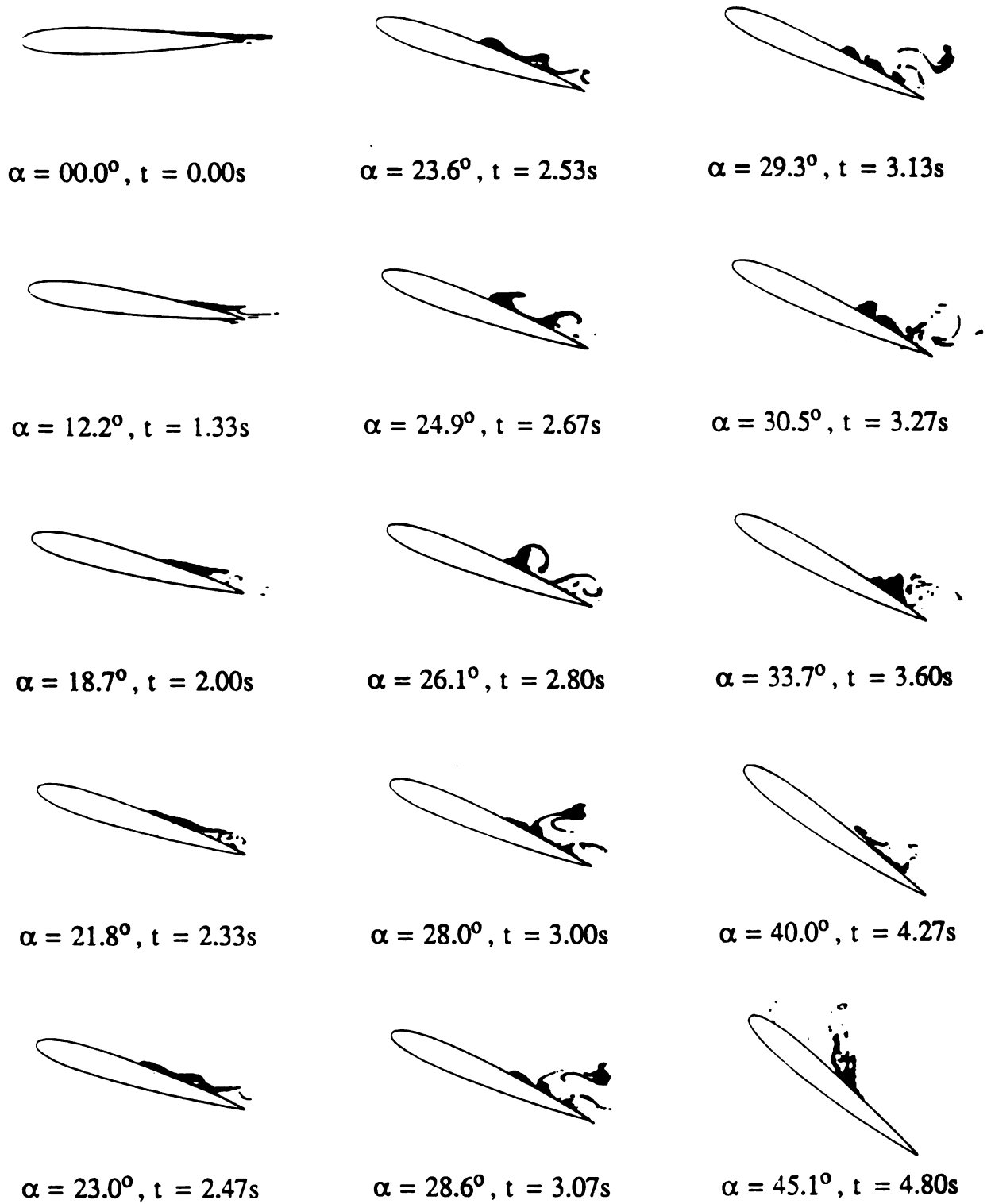
Figure 3.15. Evolution of flow field marked by dye deposited on suction surface,
$\Omega^{*} = 0.10$.

$\alpha = 00.0^\circ$, t = 0.00s

$\alpha = 31.4^\circ$, t = 1.74s

$\alpha = 39.1^\circ$, t = 2.14s

$\alpha = 11.5^\circ$, t = 0.68s

$\alpha = 32.1^\circ$, t = 1.78s

$\alpha = 43.9^\circ$, t = 2.41s

$\alpha = 17.9^\circ$, t = 1.01s

$\alpha = 32.7^\circ$, t = 1.81s

$\alpha = 50.0^\circ$, t = 2.74s

$\alpha = 24.1^\circ$, t = 1.34s

$\alpha = 35.1^\circ$, t = 1.94s

$\alpha = 56.3^\circ$, t = 3.08s

$\alpha = 29.6^\circ$, t = 1.64s

$\alpha = 37.1^\circ$, t = 2.04s

$\alpha = 59.9^\circ$, t = 3.58s
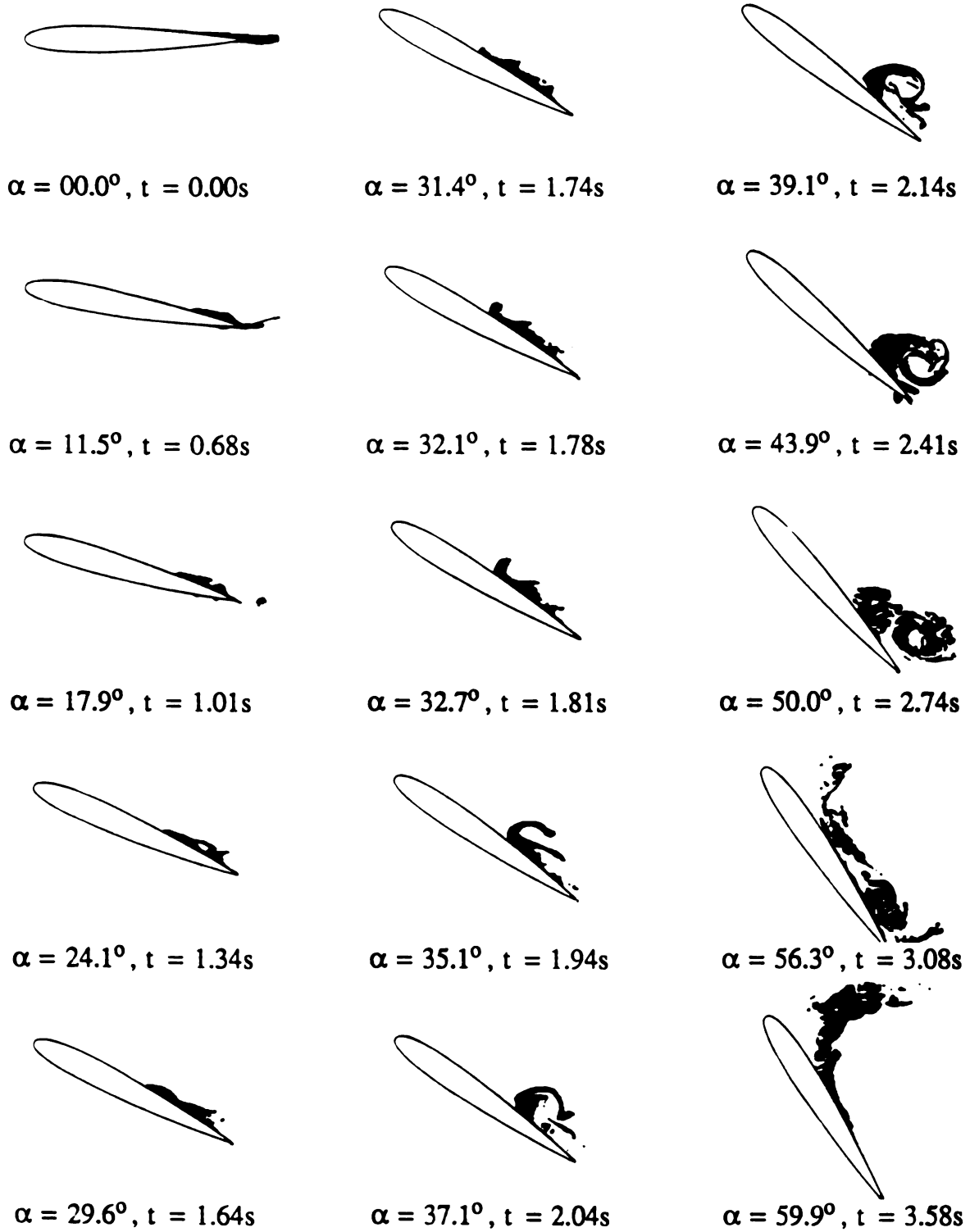
Figure 3.16. Evolution of flow field marked by dye deposited on suction surface, $\Omega^* = 0.20$.

View A-A
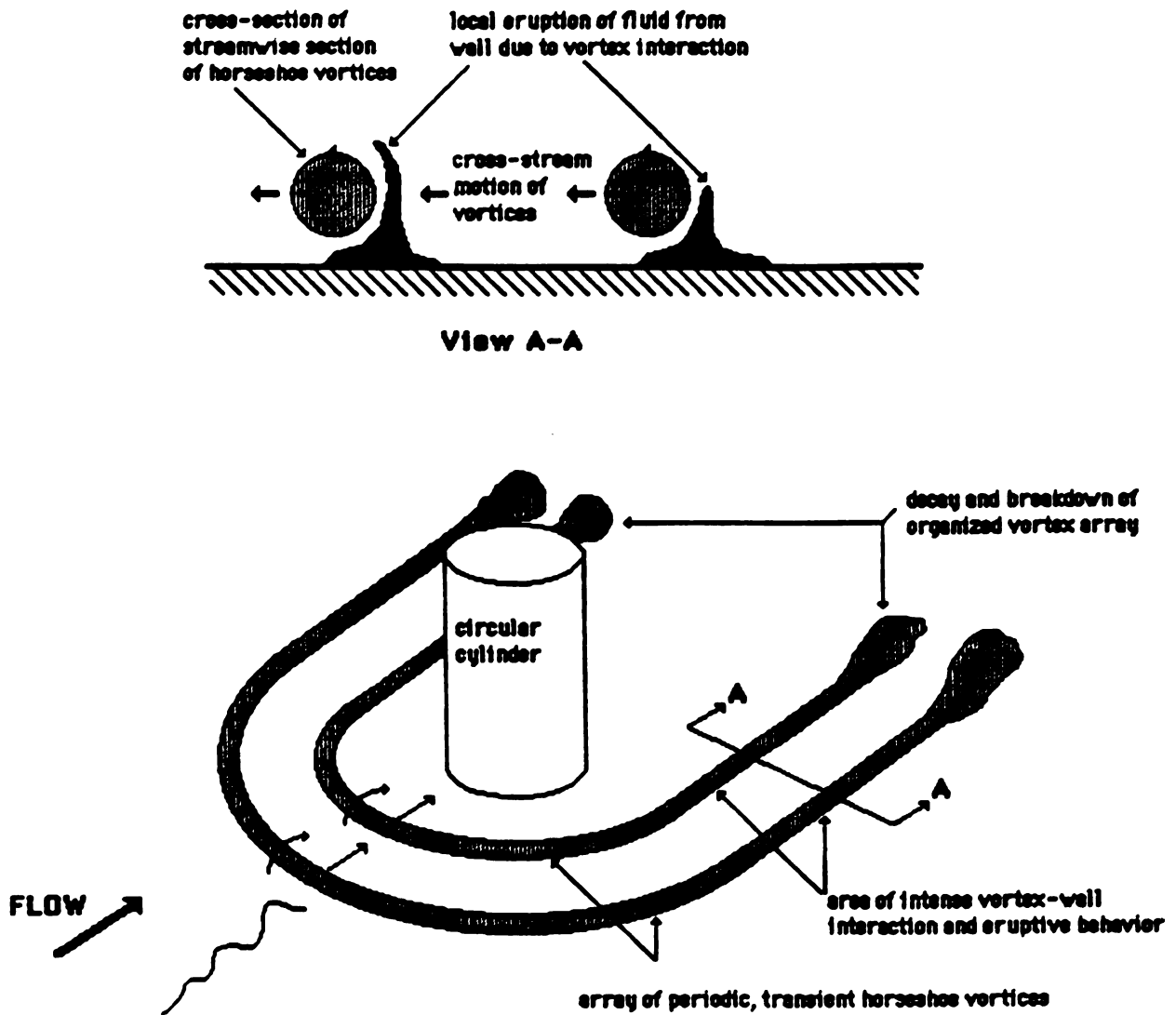
Figure 3.17. Local eruption of fluid from wall due to vortex interaction. The vortex array is developed by a laminar boundary layer impinging on a circular cylinder attached normal to the surface.
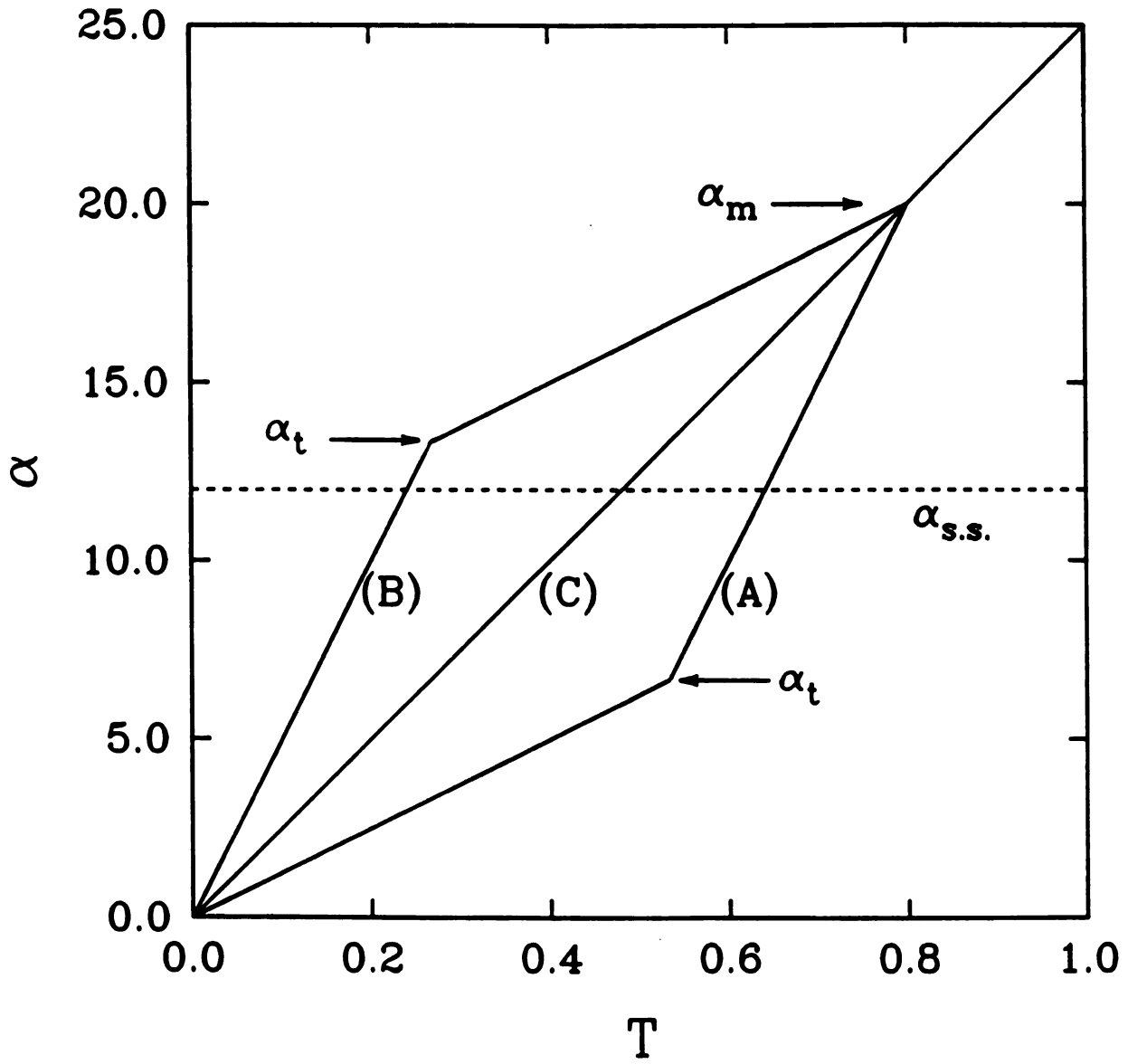
Figure 4.1. Variable motion trajectories.
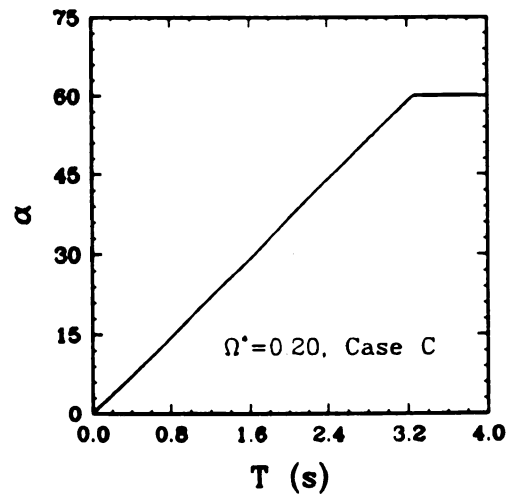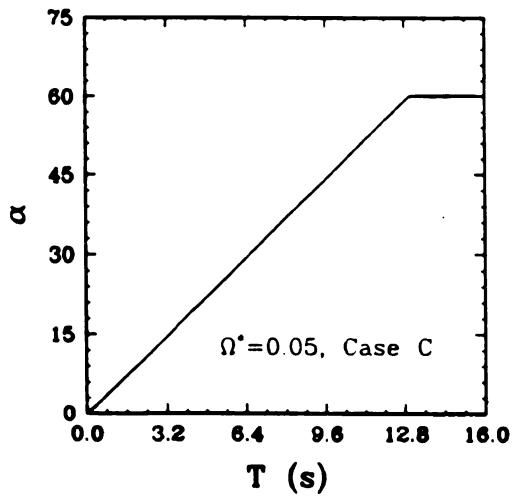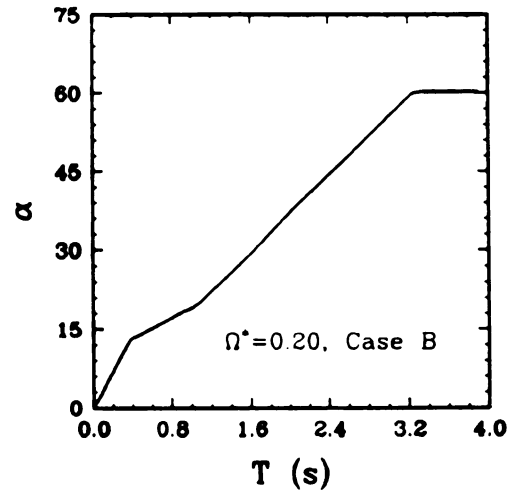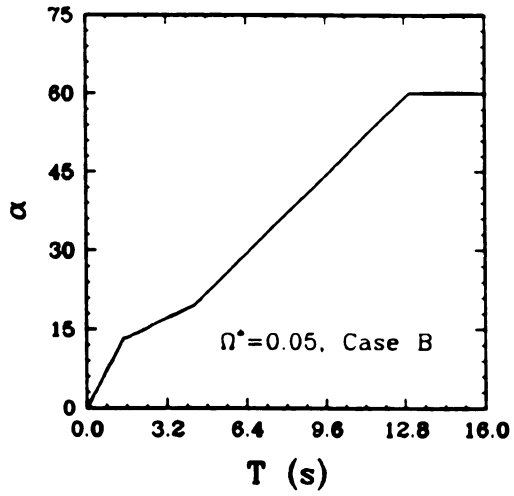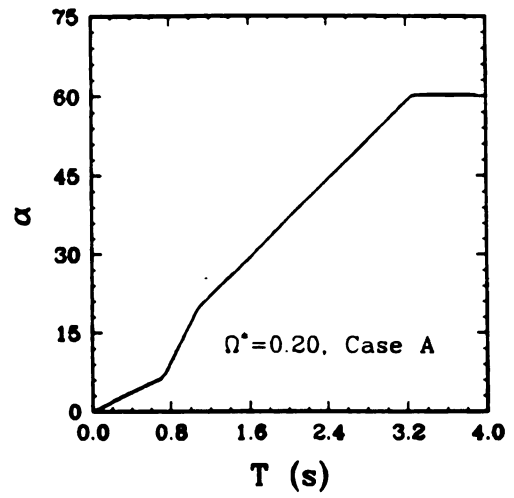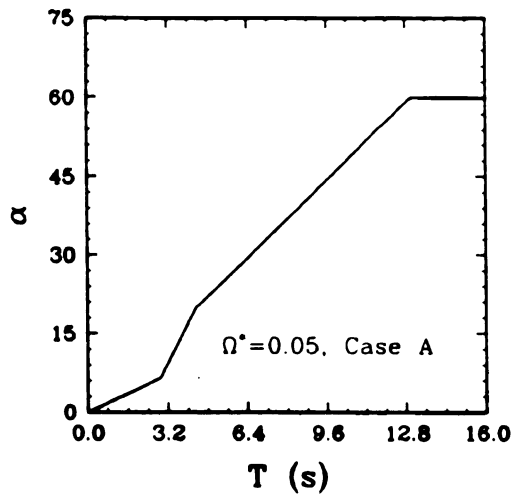
Figure 4.2. Actual trajectories for variable pitch rate motions, $\alpha_m = 20°$.
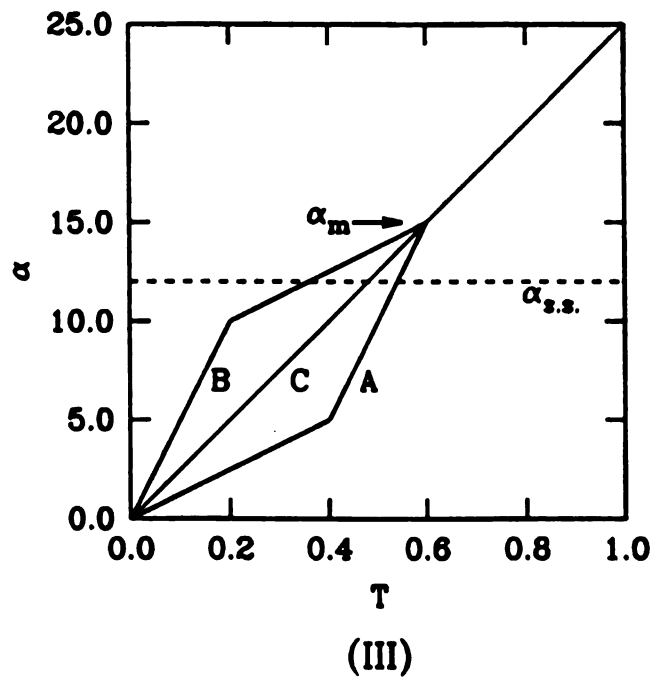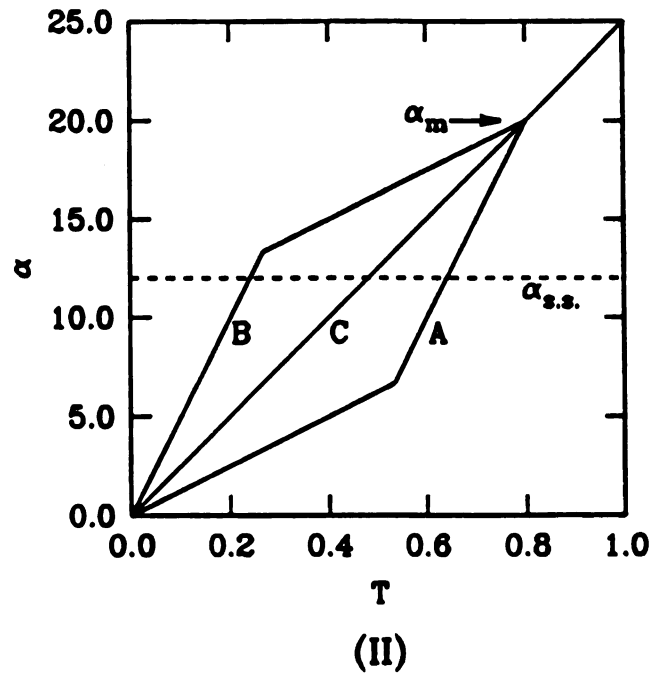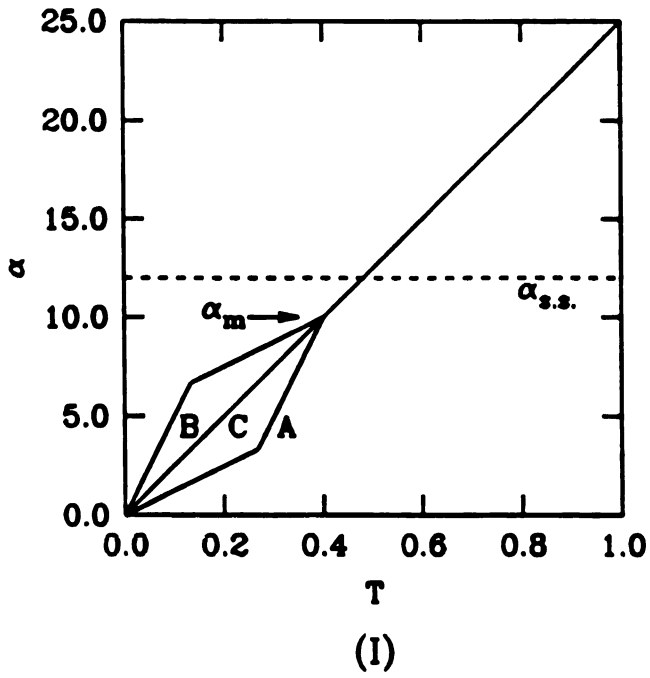
Figure 4.3. Variable motion trajectories with different matching angles.
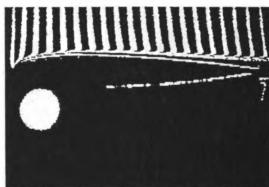
$\alpha = 00.0°$ $\alpha = 00.0°$

$\alpha = 16.9°$ $\alpha = 16.8°$

$\alpha = 21.9°$ $\alpha = 21.9°$

$\alpha = 23.8°$ $\alpha = 23.8°$
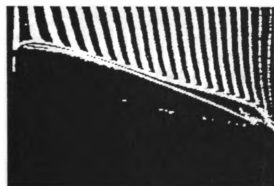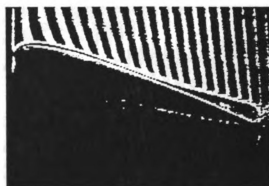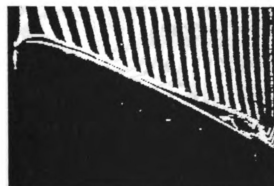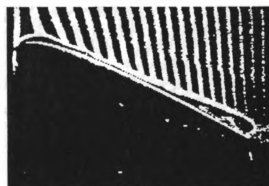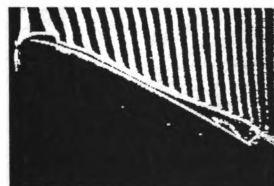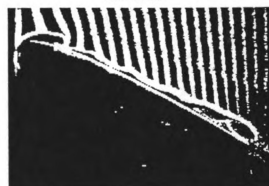
Case A   Case B

Figure 4.4. Evolution of flow field for $\alpha_m = 15°$, $\Omega^* = 0.20$, cases A and B.

α = 26.3°   α = 26.3°

α = 31.2°   α = 31.1°

α = 37.4°   α = 37.6°

α = 44.2°   α = 44.2°
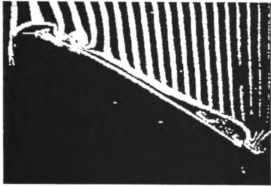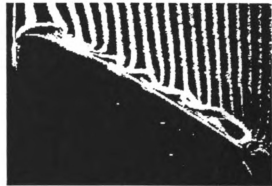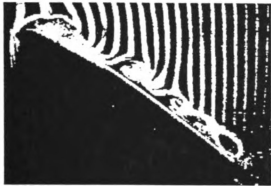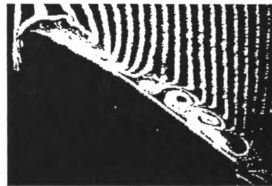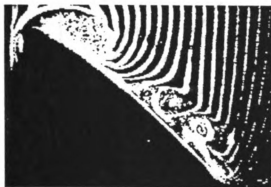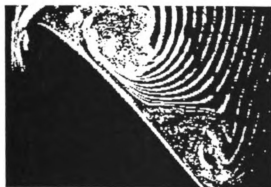
Case A   Case B

Figure 4.4 Continued.
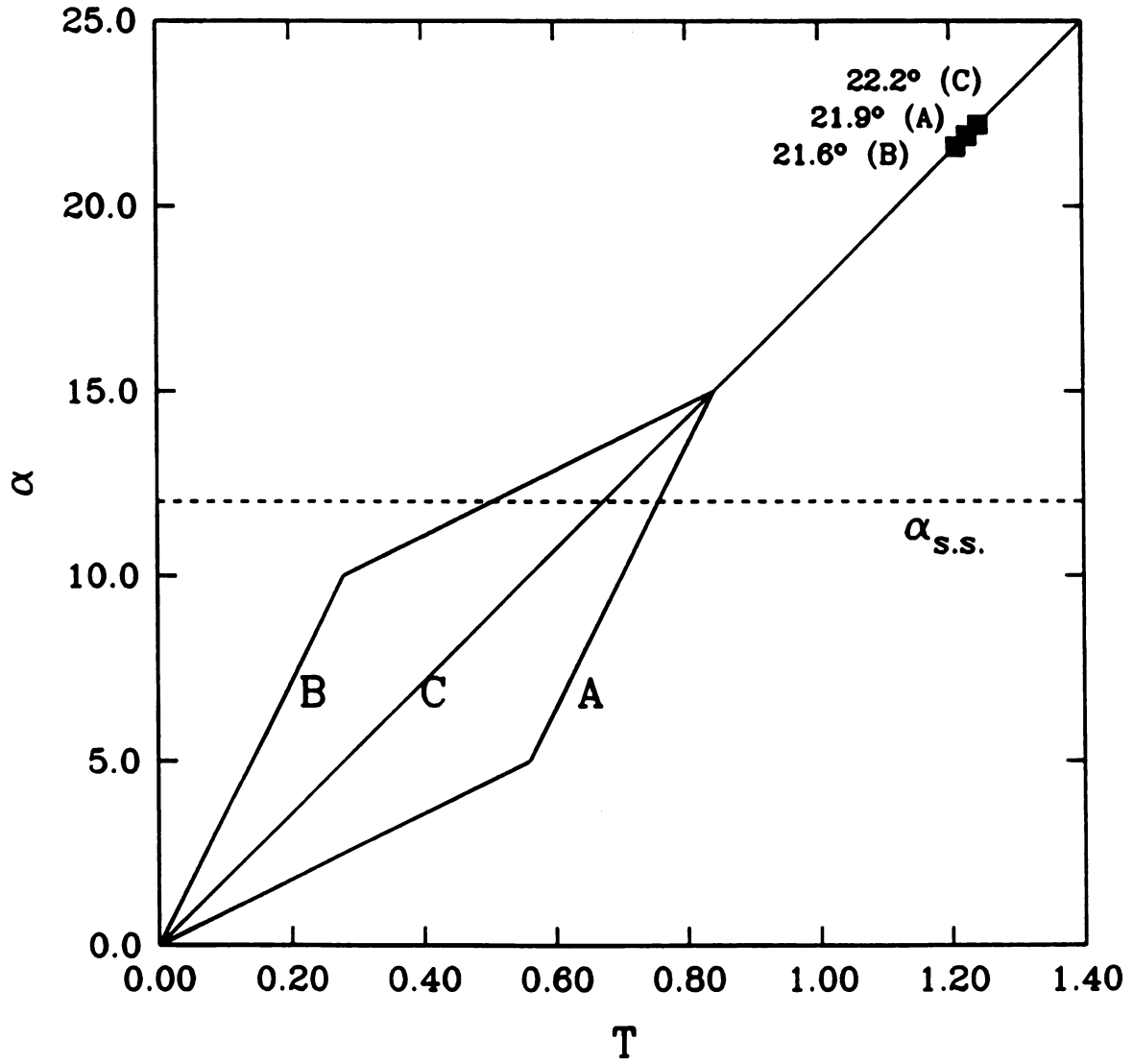
Figure 4.5. Separation angles for $\alpha_m = 15°$, $\Omega^* = 0.20$.
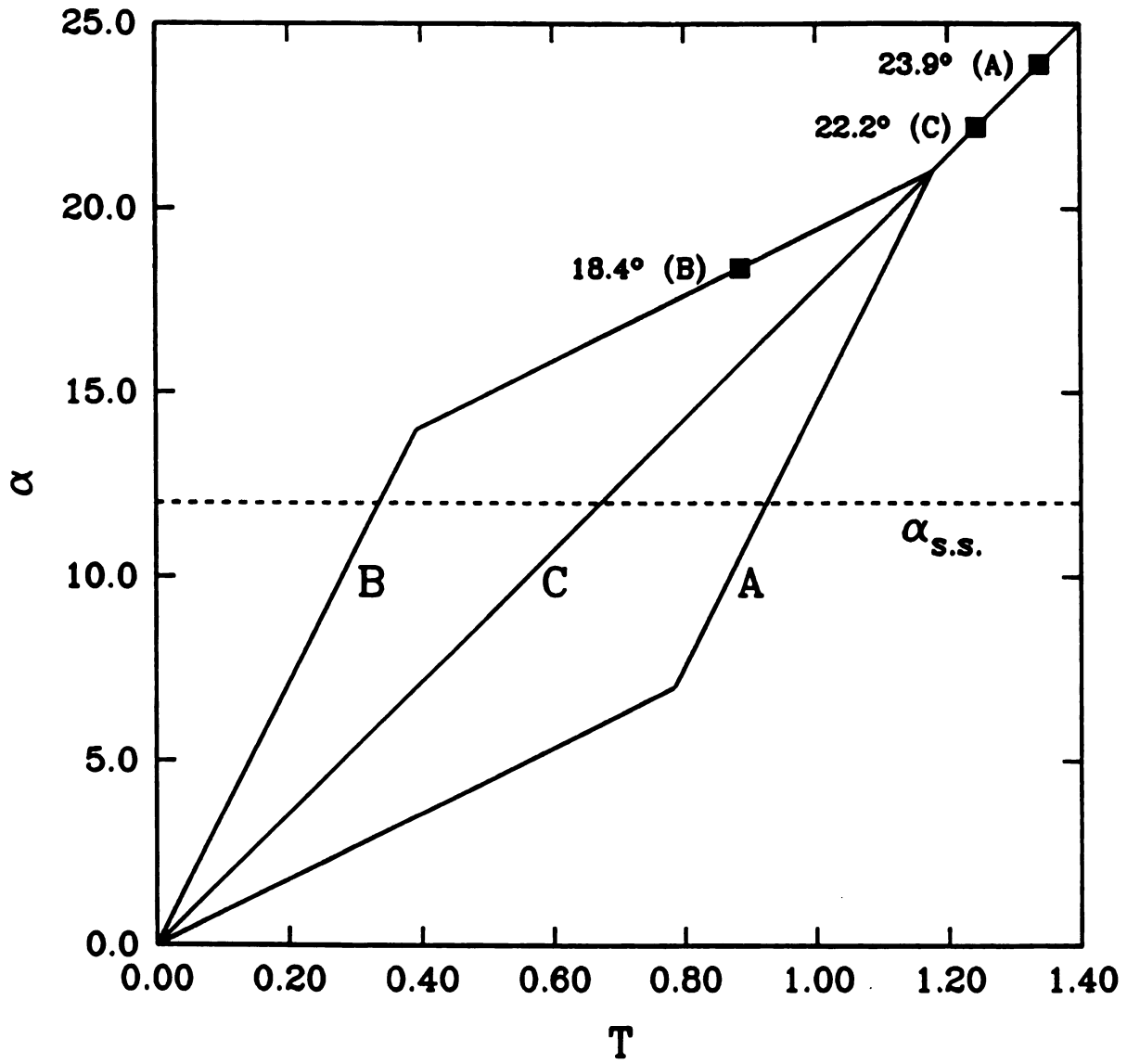
Figure 4.6. Separation angles for $\alpha_m = 21°$, $\Omega^* = 0.20$.
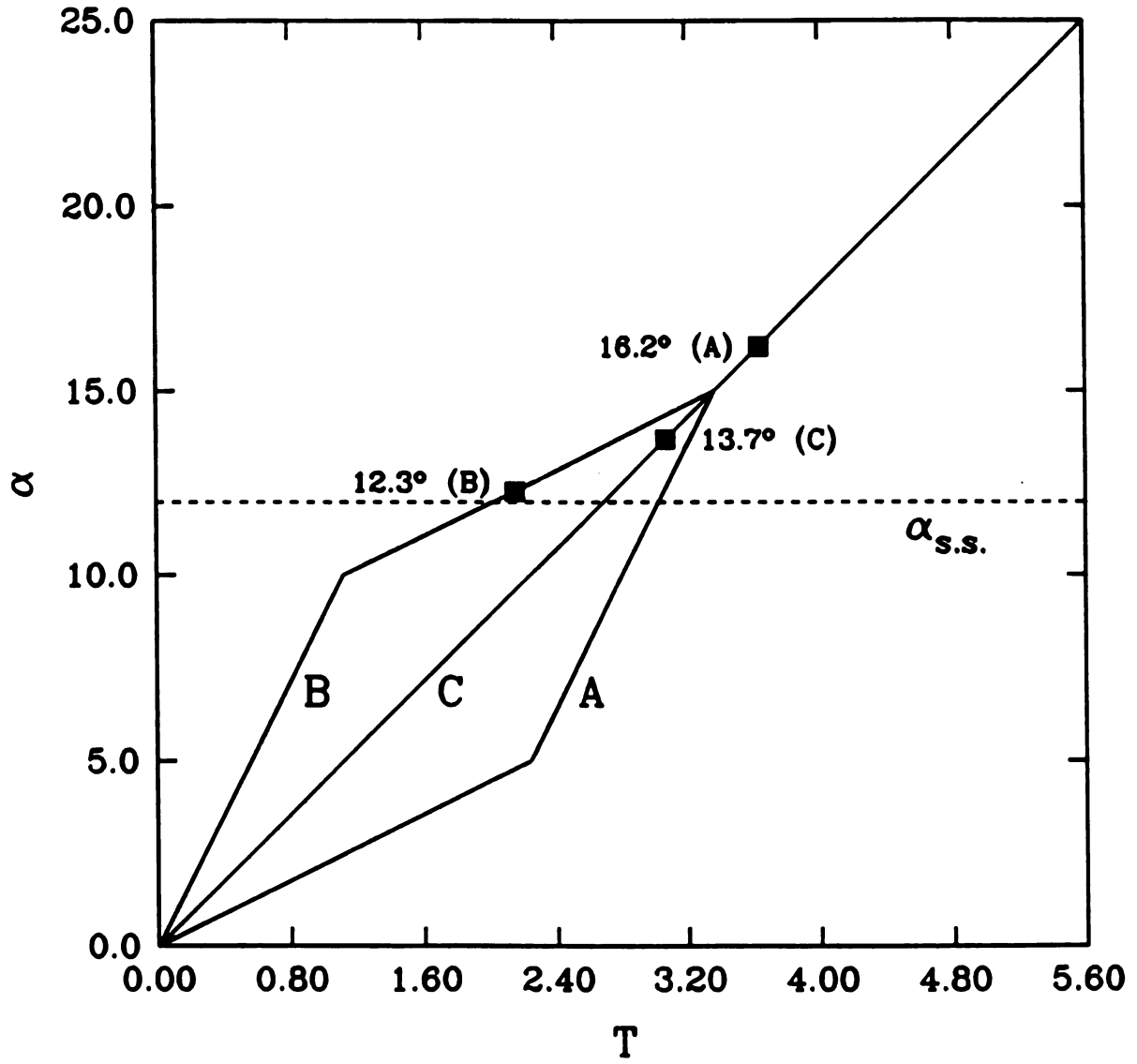
Figure 4.7. Separation angles for $\alpha_m = 15°$, $\Omega^* = 0.05$.
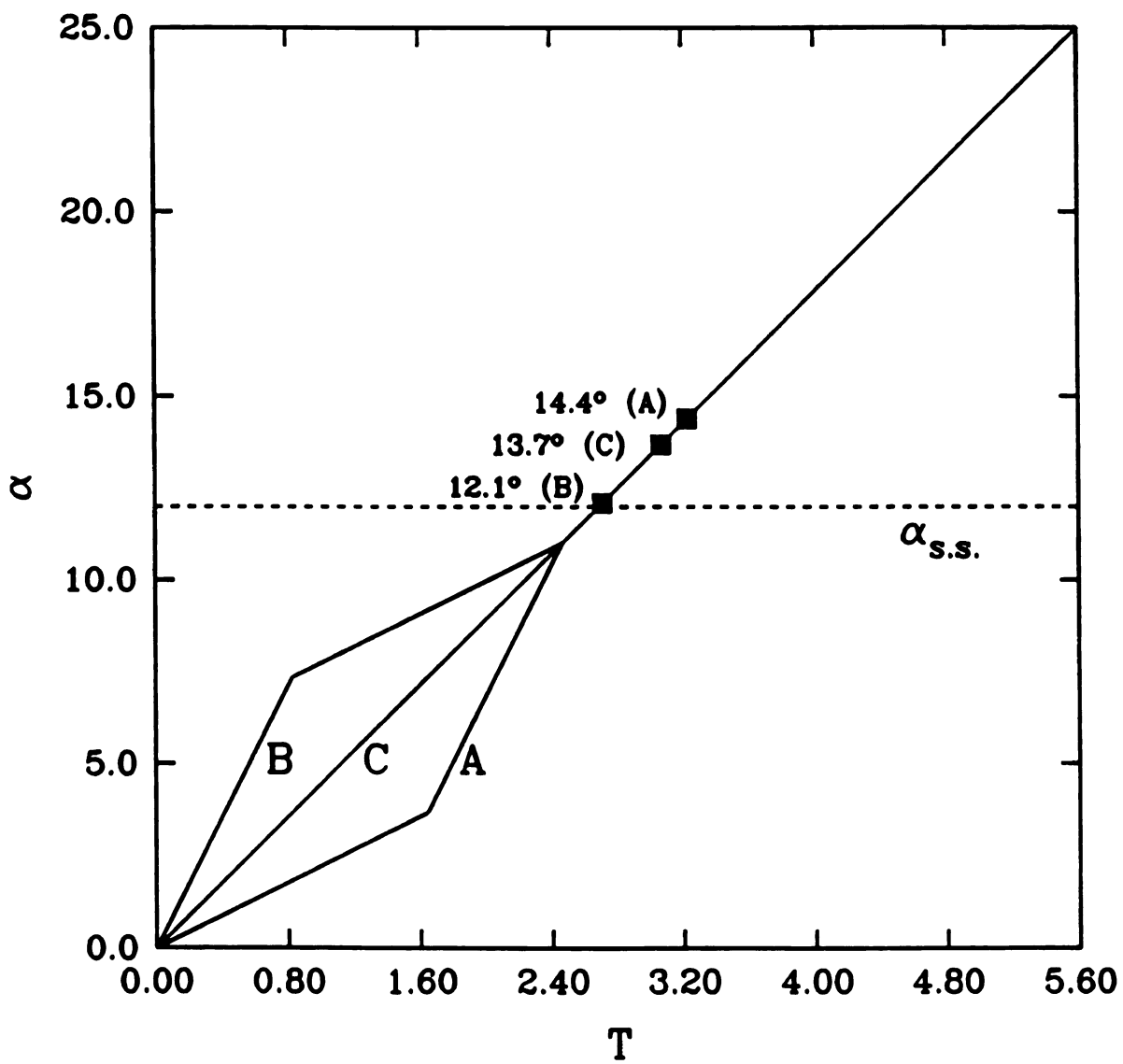
Figure 4.8. Separation angles for $\alpha_m = 11°$, $\Omega^* = 0.05$.
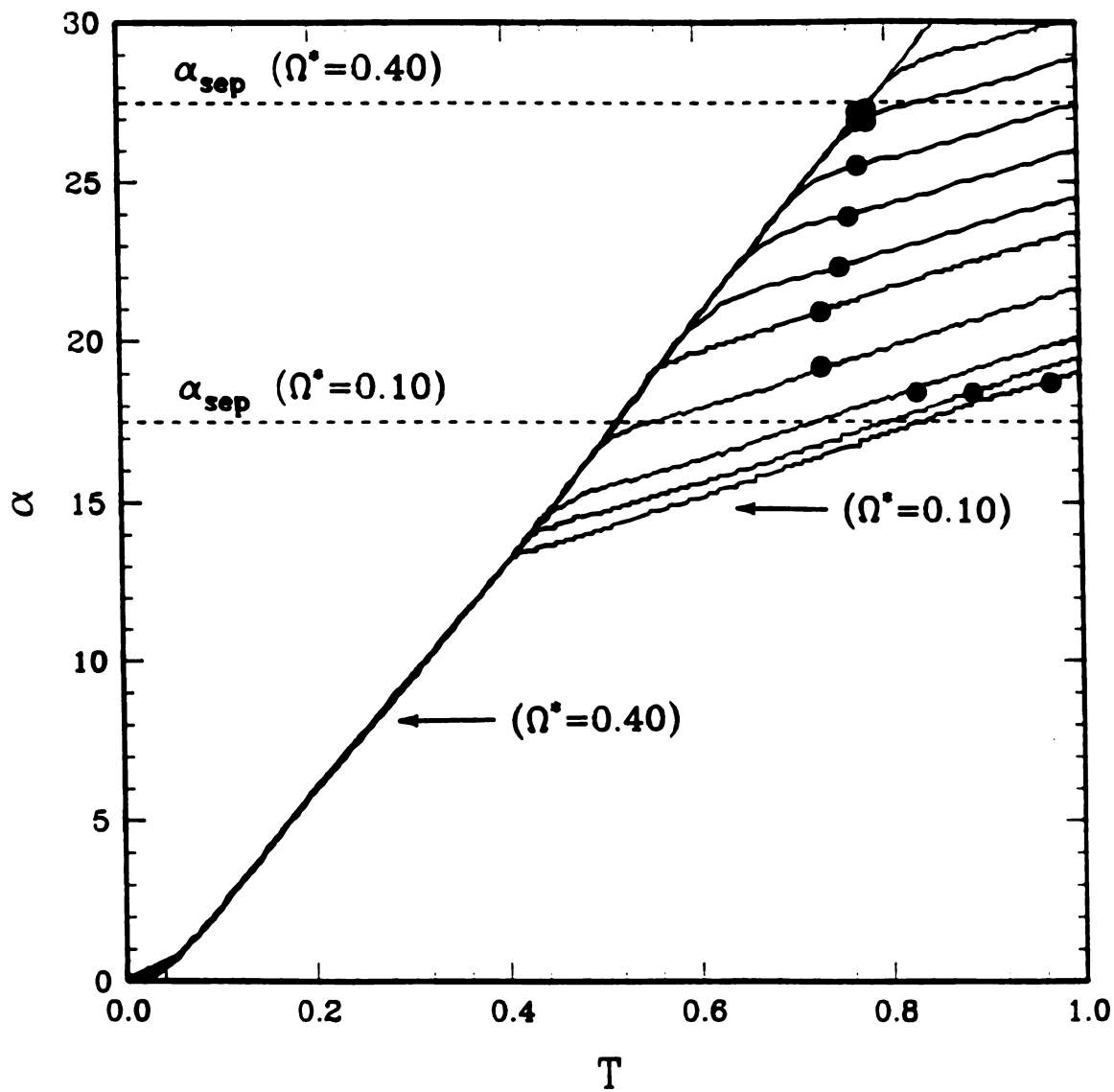
Figure 4.9. Separation angles for high α_m values, $\Omega^* = 0.20$, case B.
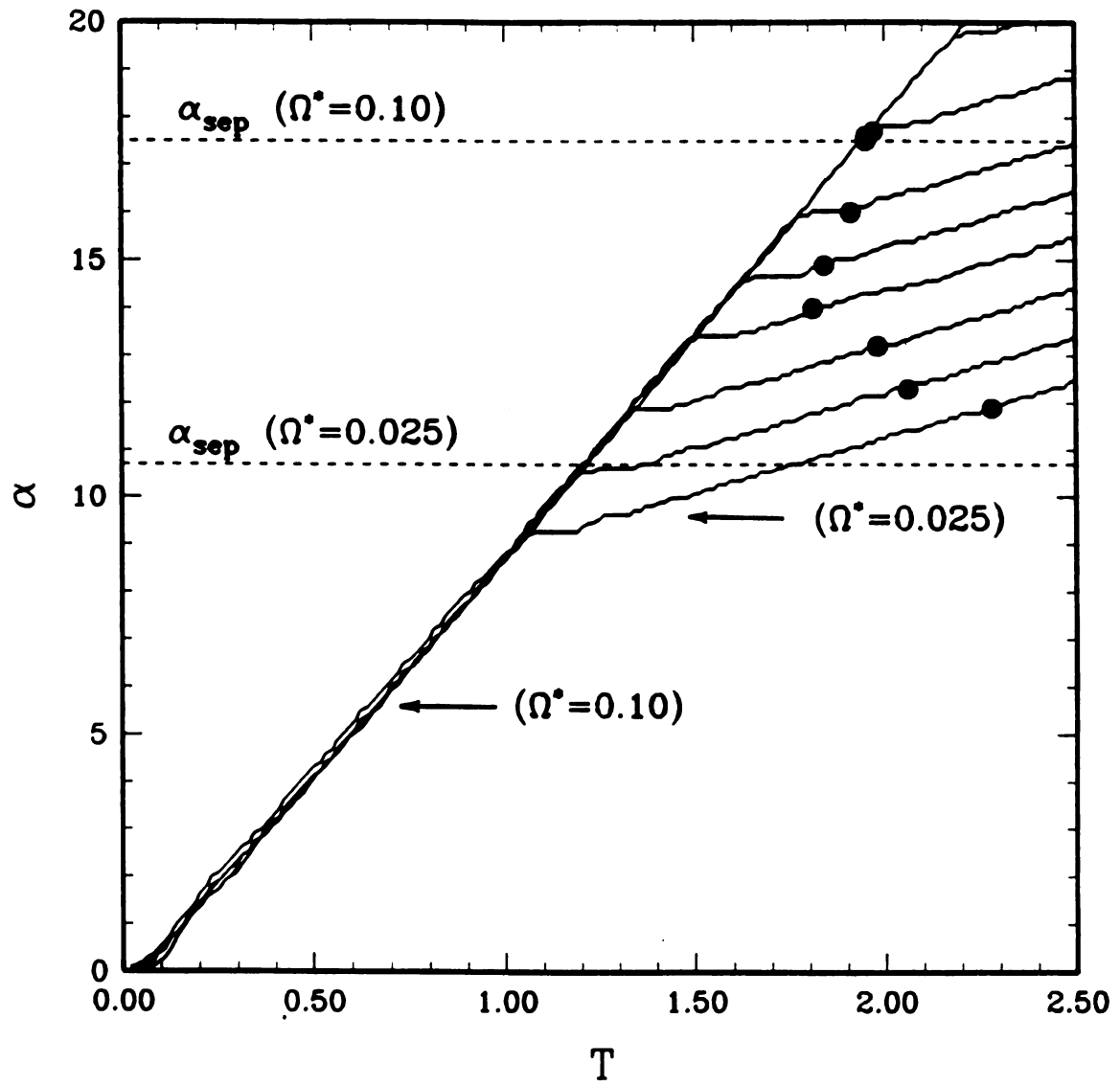
Figure 4.10. Separation angles for high α_m values, $\Omega^* = 0.05$, case B.
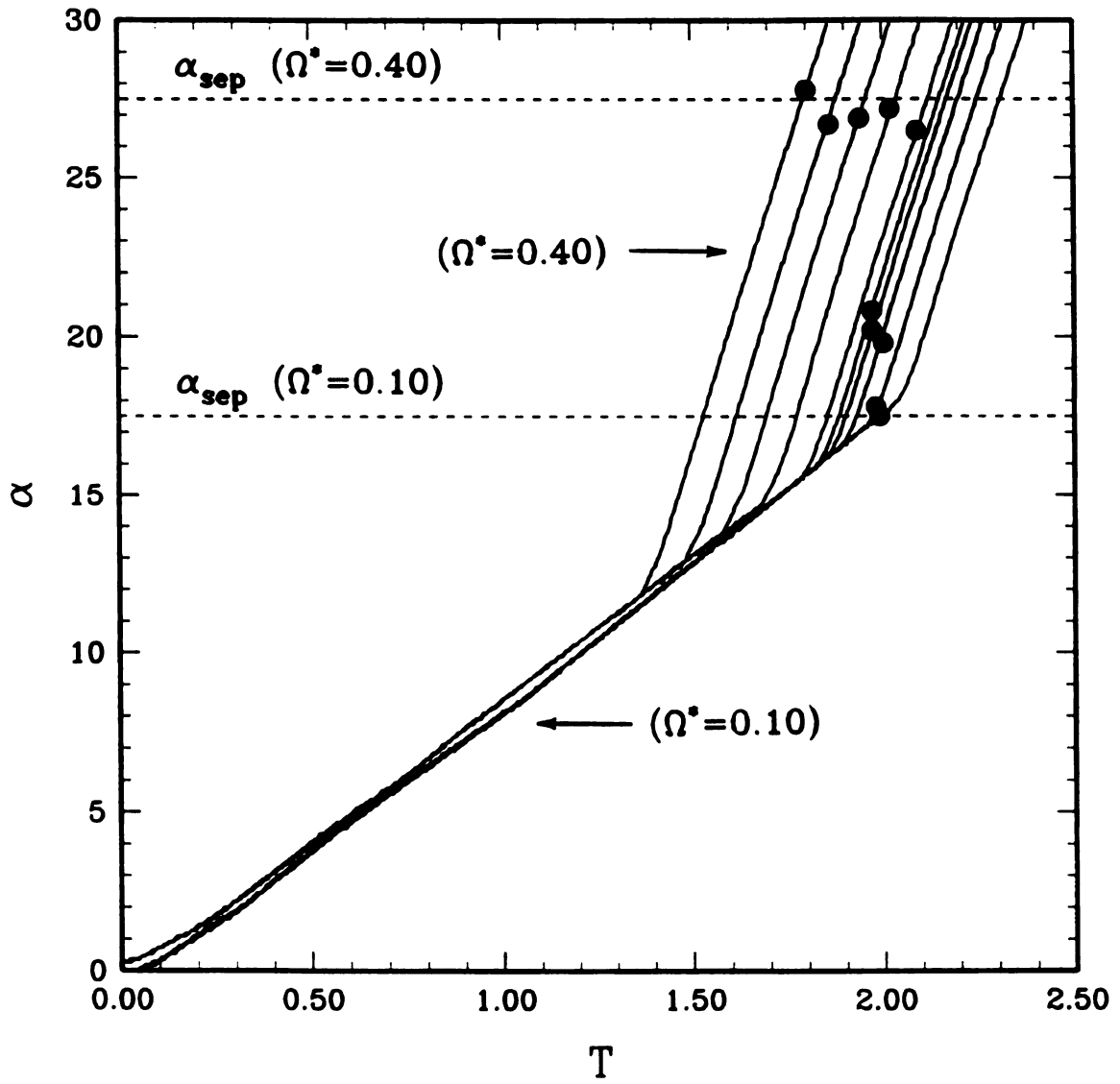
Figure 4.11. Separation angles for high α_m values, $\Omega^* = 0.20$, case A.

$\alpha = 00.0°$

$\alpha = 14.0°$

$\alpha = 21.6°$

$\alpha = 24.0°$

$\alpha = 25.4°$

$\alpha = 26.5°$

$\alpha = 27.7°$
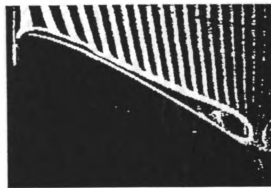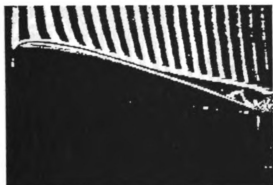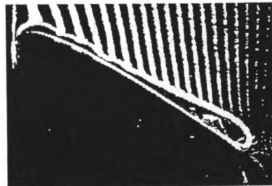
$\alpha = 30.2°$
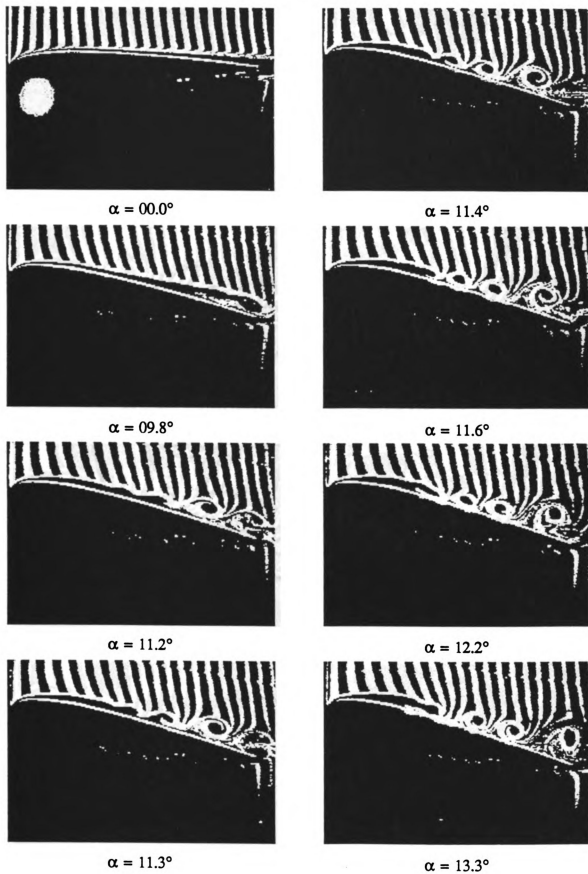
Figure 4.12. Evolution of flow field for $\alpha_t = 15.3°$, $\alpha_m = 46°$, $\Omega^* = 0.20$, case A.

α = 32.6°

α = 42.6°

α = 35.2°

α = 45.2°

α = 37.8°

α = 50.0°

α = 40.2°
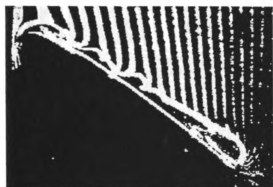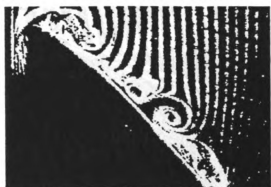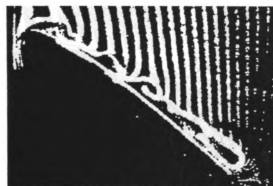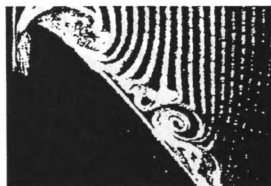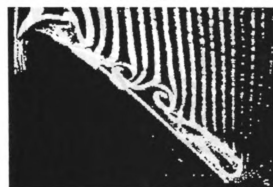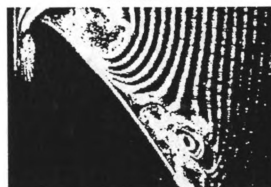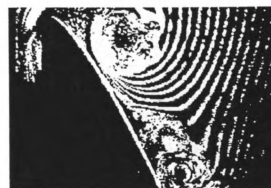
α = 59.0°

Figure 4.12 Continued.

$\alpha = 00.0°$

$\alpha = 19.3°$
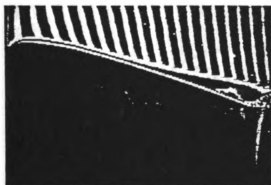
$\alpha = 13.7°$

$\alpha = 22.0°$
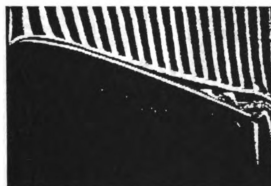
$\alpha = 16.2°$
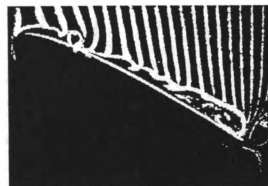
$\alpha = 24.5°$

$\alpha = 17.8°$

$\alpha = 25.6°$

Figure 4.13. Evolution of flow field for $\alpha_t = 19.3°$, $\alpha_m = 58°$, $\Omega^* = 0.20$, case A.
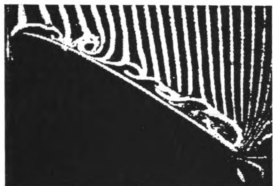
$\alpha = 26.8°$
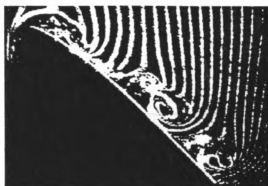
$\alpha = 38.3°$
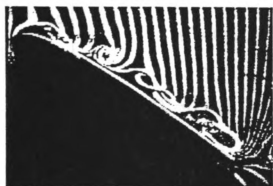
$\alpha = 29.3°$
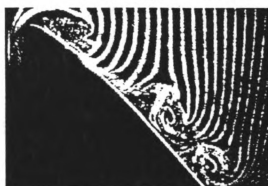
$\alpha = 41.9°$
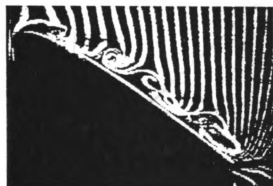
$\alpha = 30.5°$
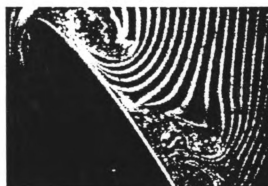
$\alpha = 50.7°$
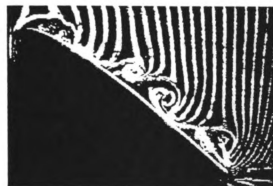
$\alpha = 34.5°$
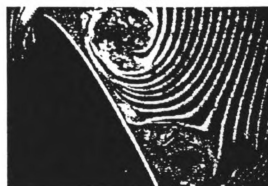
$\alpha = 57.2°$

Figure 4.13 Continued.
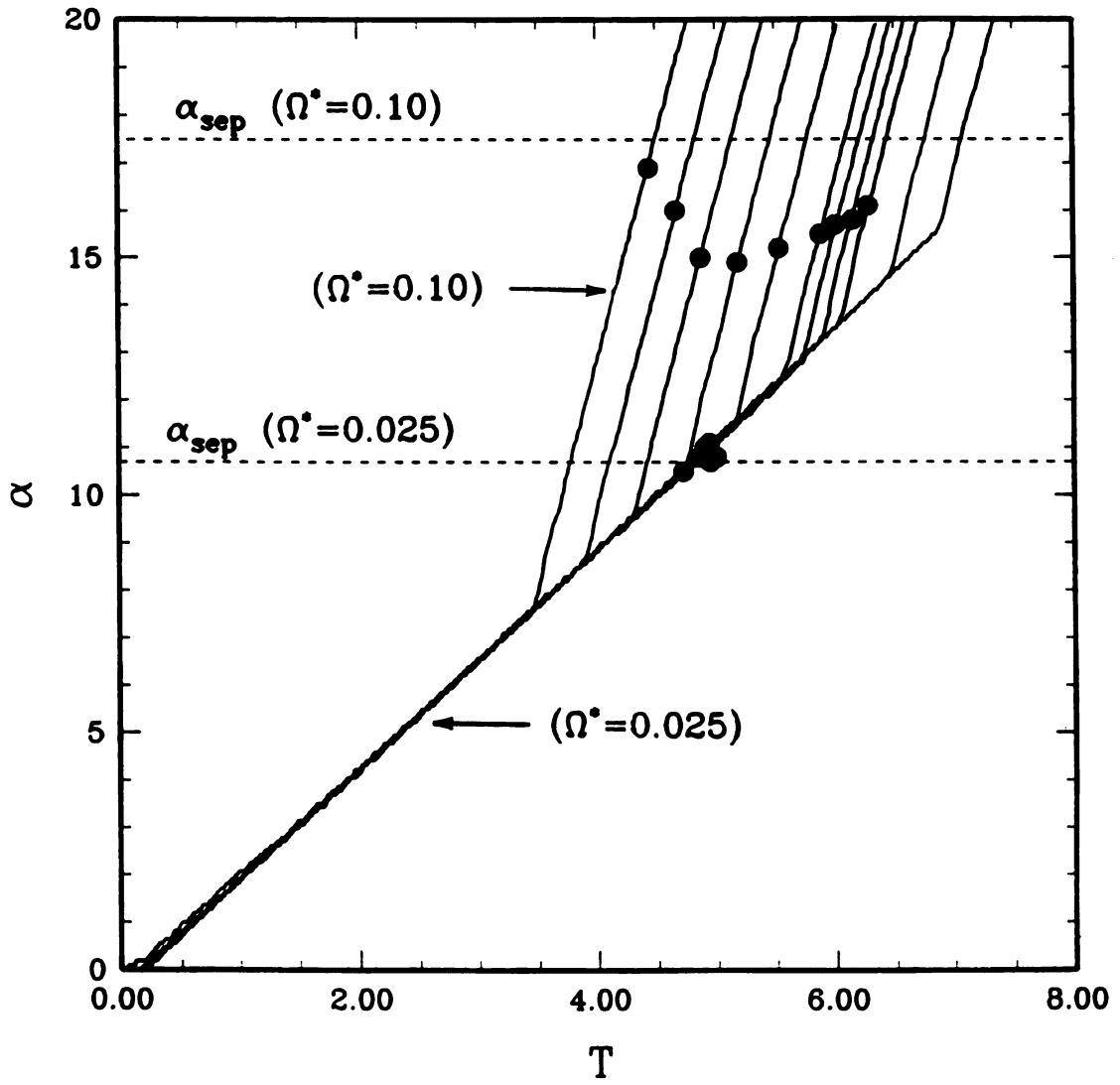
Figure 4.14. Separation angles for high α_m values, $\Omega^* = 0.05$, case A.

$\alpha = 00.0°$ $\alpha = 15.0°$

$\alpha = 10.8°$ $\alpha = 15.6°$

$\alpha = 13.7°$ $\alpha = 16.2°$

$\alpha = 14.3°$ $\alpha = 16.8°$
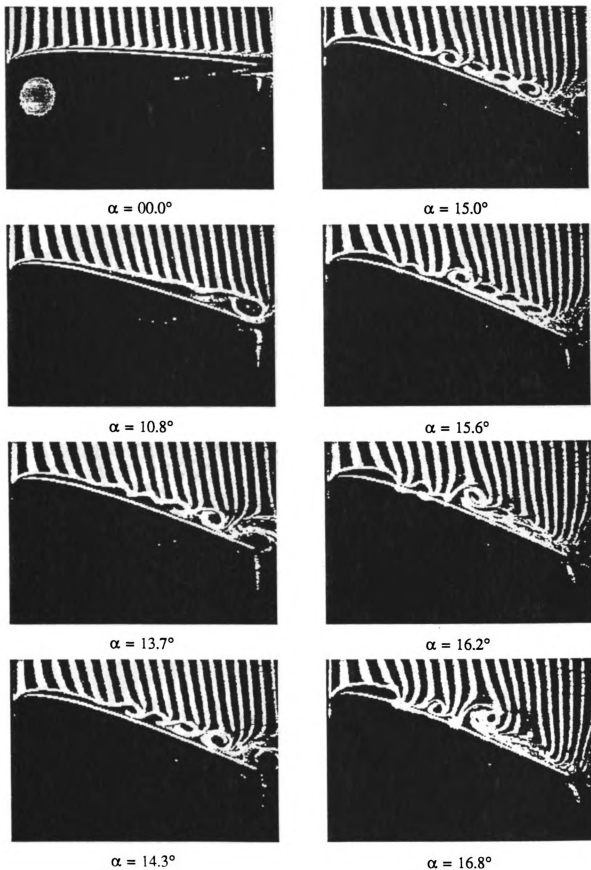
Figure 4.15. Evolution of flow field for $\alpha_i = 9.7°$, $\alpha_m = 29°$, $\Omega^* = 0.05$, case A.
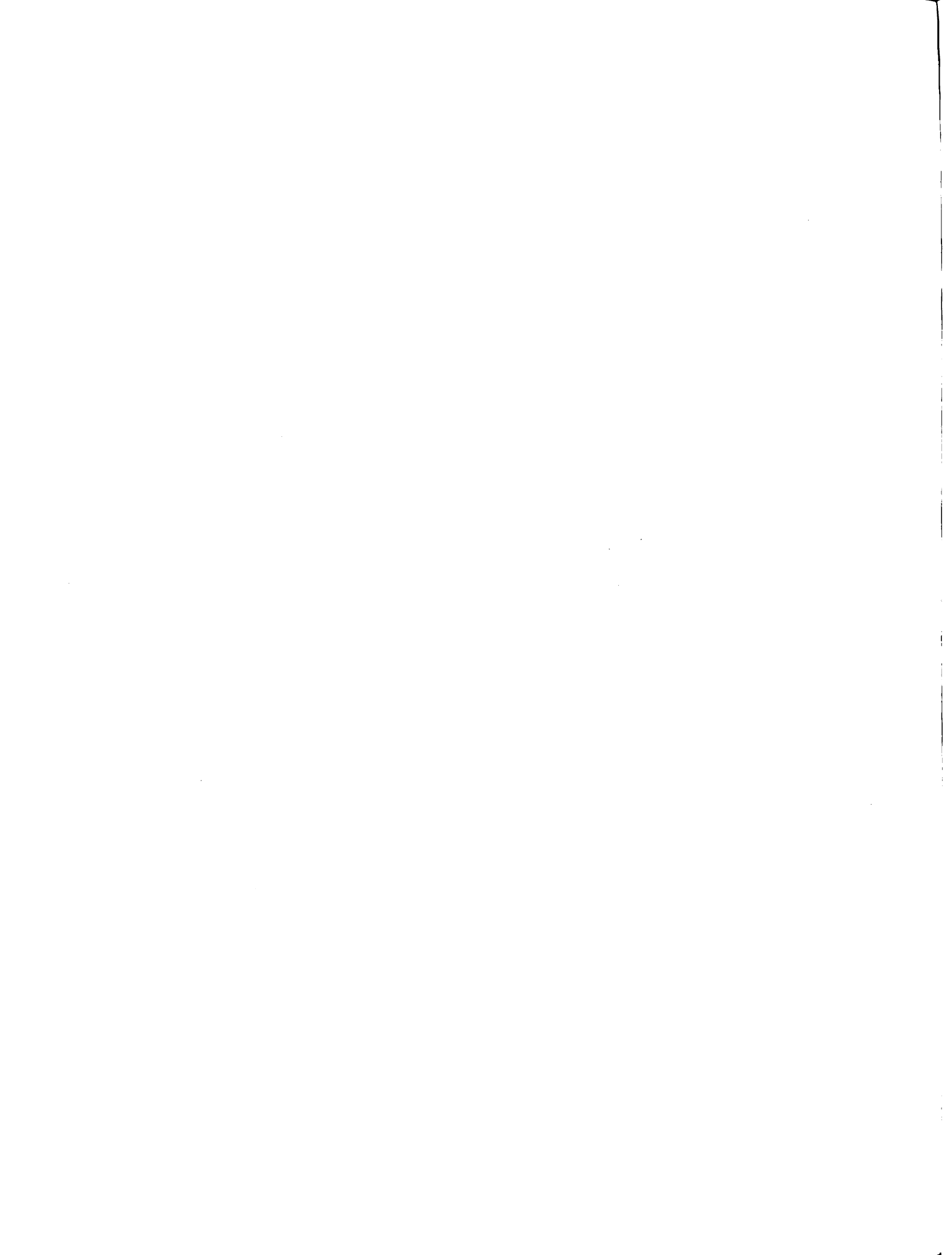
$\alpha = 17.5°$

$\alpha = 20.9°$

$\alpha = 18.1°$
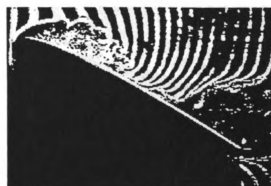
$\alpha = 23.8°$

$\alpha = 18.7°$

$\alpha = 26.3°$

$\alpha = 19.4°$

$\alpha = 30.8°$

Figure 4.15 Continued.

$\alpha = 00.0°$ $\alpha = 11.3°$

$\alpha = 10.0°$ $\alpha = 11.4°$

$\alpha = 10.7°$ $\alpha = 11.5°$

$\alpha = 11.1°$ $\alpha = 11.7°$
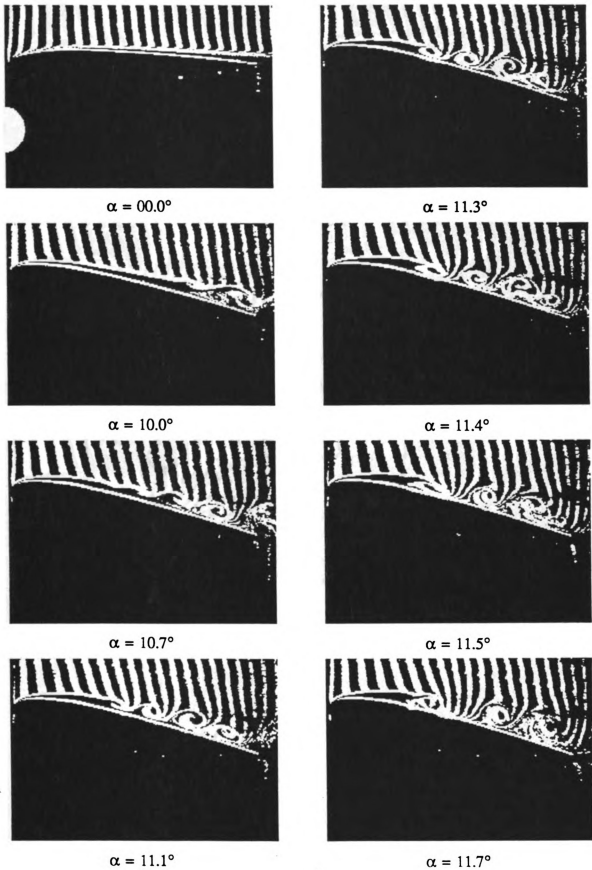
Figure 4.16. Evolution of flow field for $\alpha_t = 13.7°$, $\alpha_m = 41°$, $\Omega^* = 0.05$, case A.

$\alpha = 11.9°$
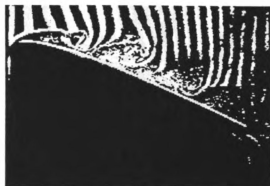
$\alpha = 18.0°$
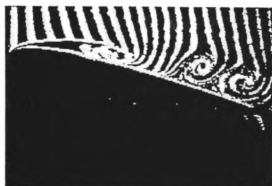
$\alpha = 12.1°$
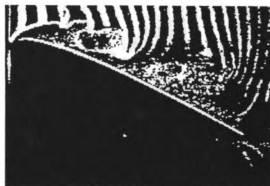
$\alpha = 21.0°$
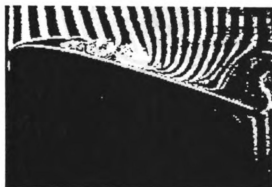
$\alpha = 12.8°$

$\alpha = 24.1°$
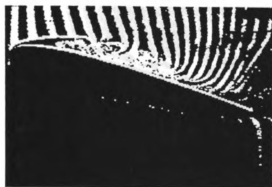
$\alpha = 13.2°$

$\alpha = 27.2°$

Figure 4.16 Continued.

$\alpha = 00.0°$ $\alpha = 11.4°$

$\alpha = 09.8°$ $\alpha = 11.6°$

$\alpha = 11.2°$ $\alpha = 12.2°$

$\alpha = 11.3°$ $\alpha = 13.3°$

Figure 4.17. Evolution of flow field for $\alpha_r = 11.7°$, $\alpha_m = 35°$, $\Omega^* = 0.05$, case A.
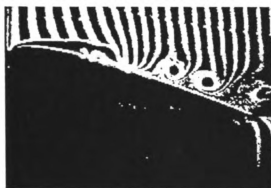
$\alpha = 14.2°$
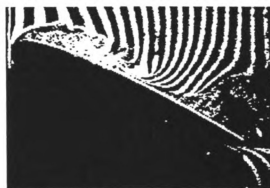
$\alpha = 22.6°$
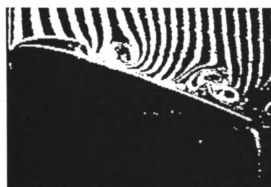
$\alpha = 16.2°$
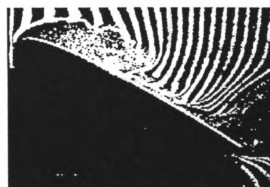
$\alpha = 25.0°$
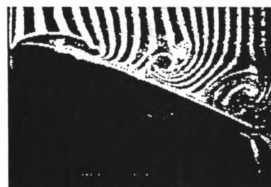
$\alpha = 18.0°$
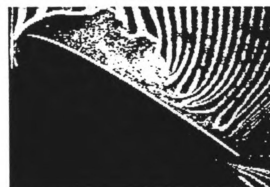
$\alpha = 28.2°$
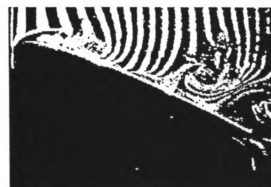
$\alpha = 19.9°$
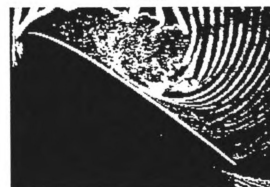
$\alpha = 31.2°$

Figure 4.17 Continued.
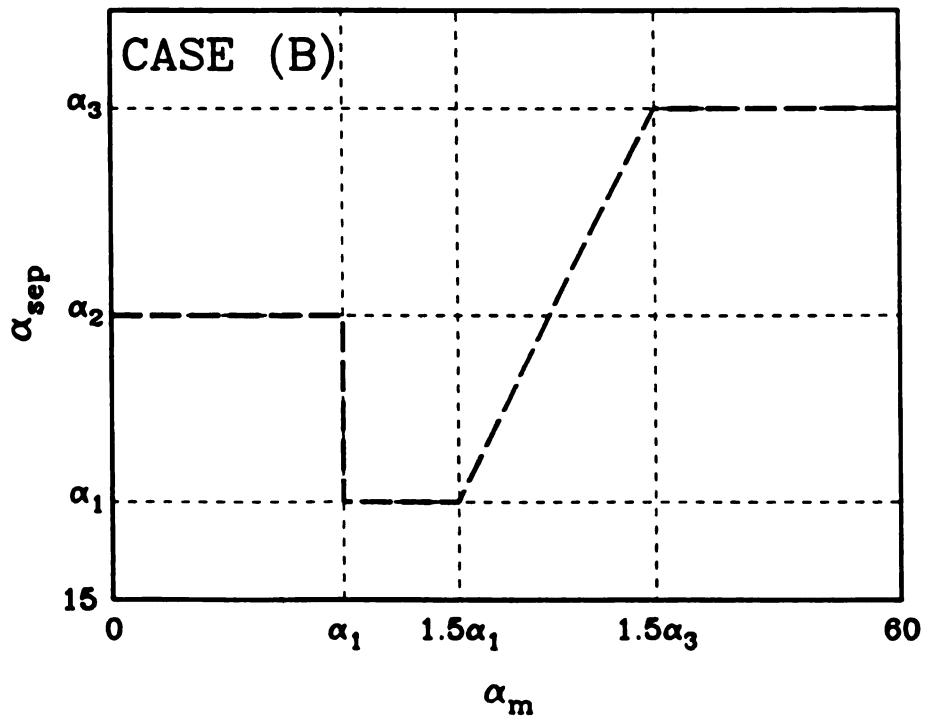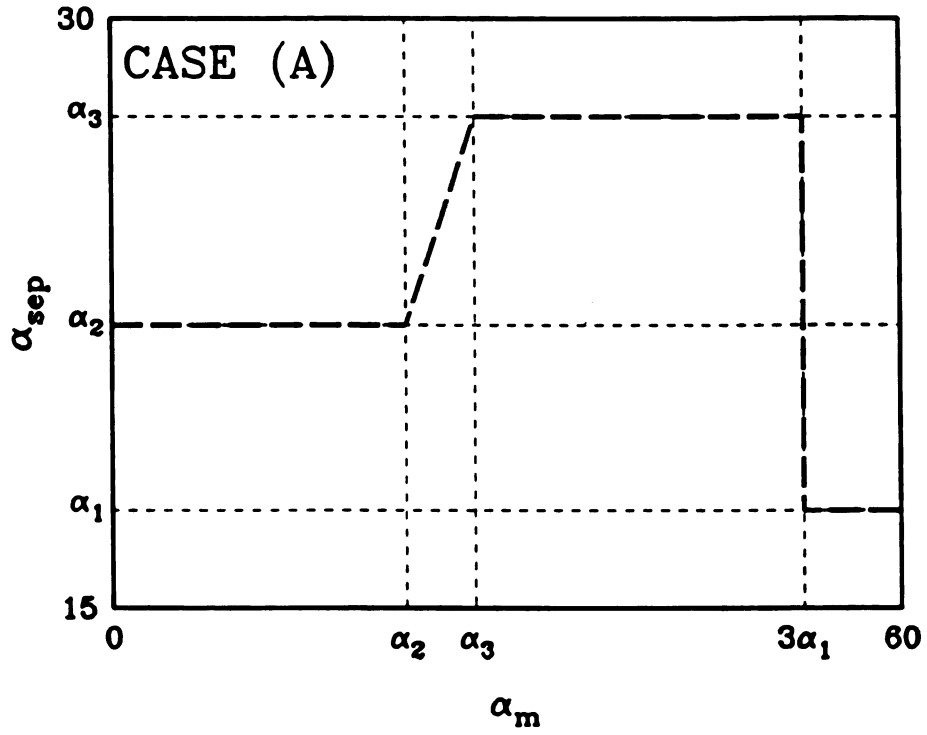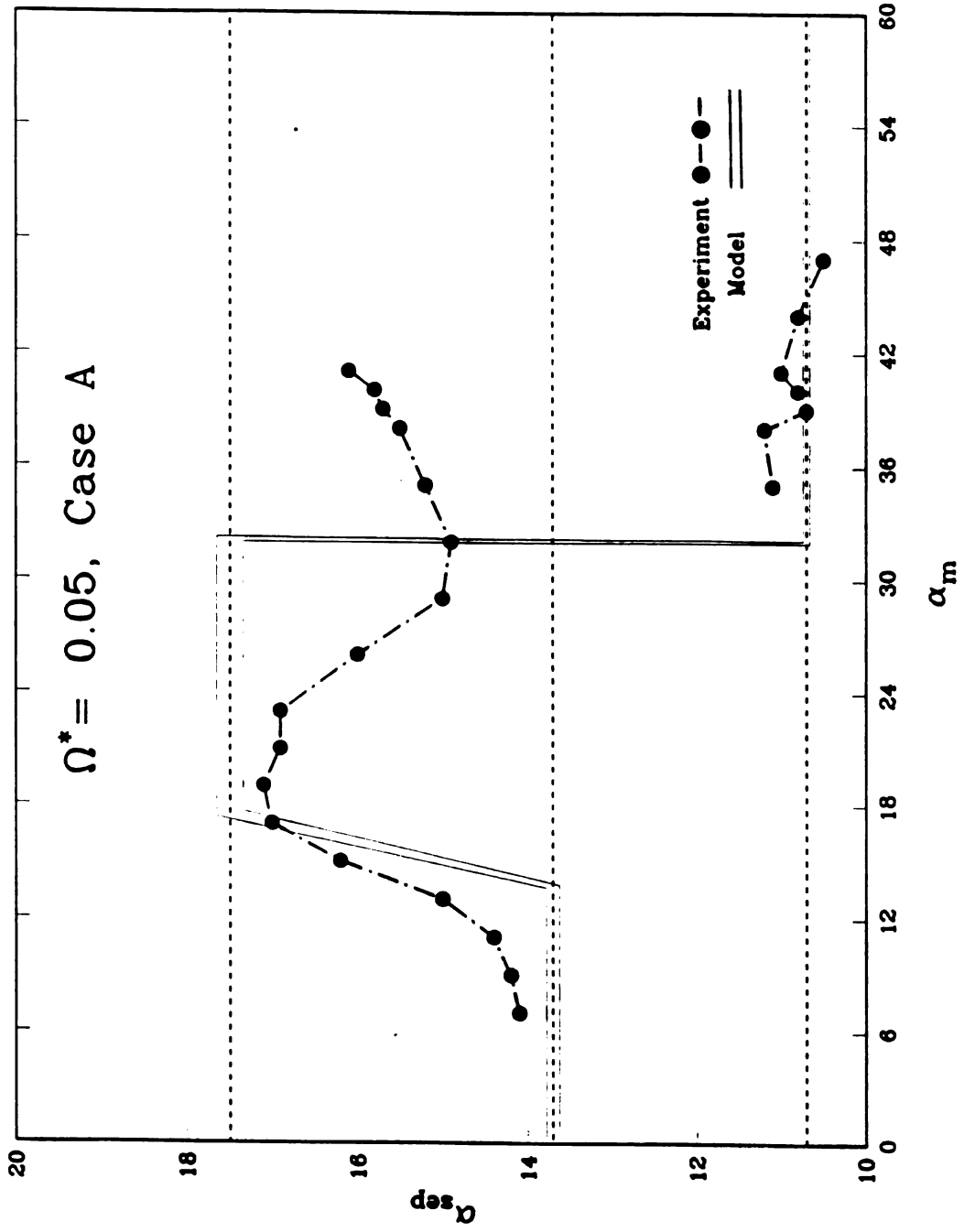
Figure 4.18. Graphical representation of separation model.

Figure 4.19. α_{sep} vs α_m for $\Omega^* = 0.05$, case A.
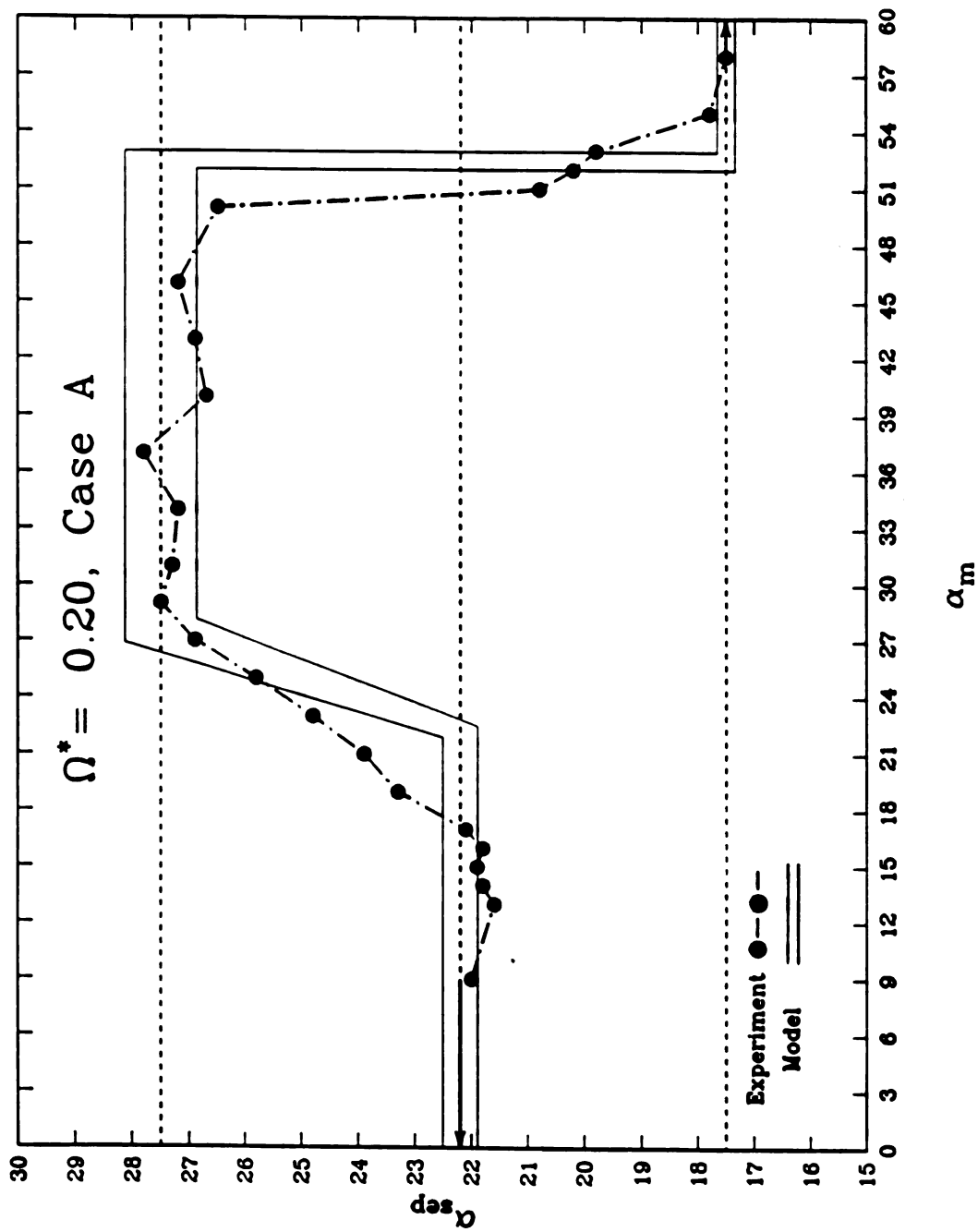
Figure 4.20. α_{sep} vs α_m for $\Omega^* = 0.20$, case A.
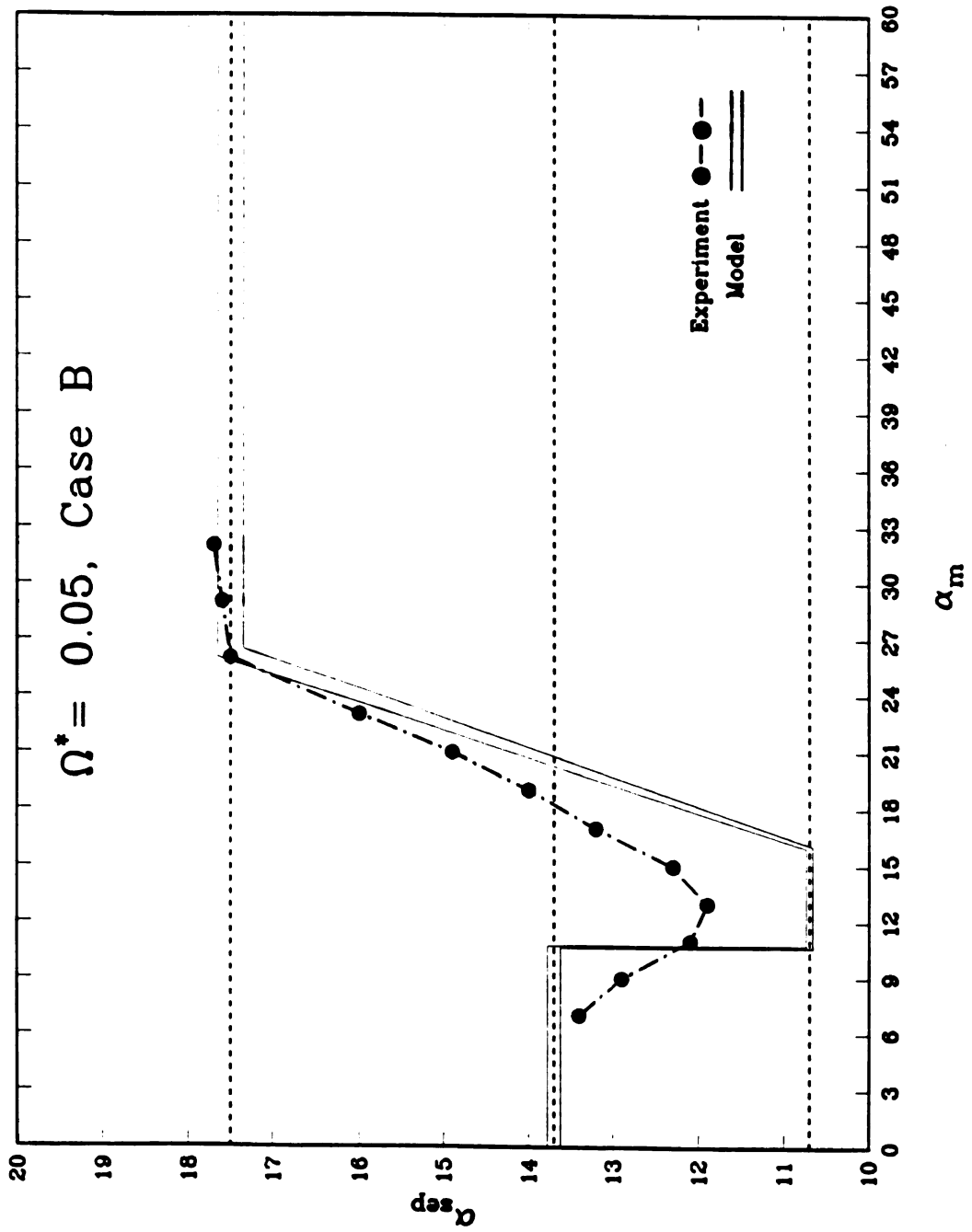
Figure 4.21. α_{sep} vs α_m for $\Omega^* = 0.05$, case B.

Figure 4.22. α_{sep} vs α_m for $\Omega^* = 0.20$, case B.